

Evidence for Neutrino Oscillations from Muon Decay at Rest

C. Athanassopoulos¹², L. B. Auerbach¹², R. L. Burman⁷,
 I. Cohen⁶, D. O. Caldwell³, B. D. Dieterle¹⁰, J. B. Donahue⁷, A. M. Eisner⁴,
 A. Fazely¹¹, F. J. Federspiel⁷, G. T. Garvey⁷, M. Gray³, R. M. Gunasingha⁸,
 R. Imlay⁸, K. Johnston⁹, H. J. Kim⁸, W. C. Louis⁷, R. Majkic¹², J. Margulies¹²,
 K. McIlhany¹, W. Metcalf⁸, G. B. Mills⁷, R. A. Reeder¹⁰, V. Sandberg⁷, D. Smith⁵,
 I. Stancu¹, W. Strossman¹, R. Tayloe⁷, G. J. VanDalen¹, W. Vernon^{2,4}, N. Wadia⁸,
 J. Waltz⁵, Y-X. Wang⁴, D. H. White⁷, D. Works¹², Y. Xiao¹², S. Yellin³

LSND Collaboration

¹*University of California, Riverside, CA 92521*

²*University of California, San Diego, CA 92093*

³*University of California, Santa Barbara, CA 93106*

⁴*University of California Intercampus Institute for Research at Particle Accelerators, Stanford,
 CA 94309*

⁵*Embry Riddle Aeronautical University, Prescott, AZ 86301*

⁶*Linfield College, McMinnville, OR 97128*

⁷*Los Alamos National Laboratory, Los Alamos, NM 87545*

⁸*Louisiana State University, Baton Rouge, LA 70803*

⁹*Louisiana Tech University, Ruston, LA 71272*

¹⁰*University of New Mexico, Albuquerque, NM 87131*

¹¹*Southern University, Baton Rouge, LA 70813*

¹²*Temple University, Philadelphia, PA 19122*

(March 30, 2022)

Abstract

A search for $\bar{\nu}_\mu \rightarrow \bar{\nu}_e$ oscillations has been conducted at the Los Alamos

Meson Physics Facility using $\bar{\nu}_\mu$ from μ^+ decay at rest. The $\bar{\nu}_e$ are detected via the reaction $\bar{\nu}_e p \rightarrow e^+ n$, correlated with the 2.2 MeV γ from $np \rightarrow d\gamma$. The use of tight cuts to identify e^+ events with correlated γ rays yields 22 events with e^+ energy between 36 and 60 MeV and only 4.6 ± 0.6 background events. The probability that this excess is due entirely to a statistical fluctuation is 4.1×10^{-8} . A χ^2 fit to the entire e^+ sample results in a total excess of $51.8^{+18.7}_{-16.9} \pm 8.0$ events with e^+ energy between 20 and 60 MeV. If attributed to $\bar{\nu}_\mu \rightarrow \bar{\nu}_e$ oscillations, this corresponds to an oscillation probability (averaged over the experimental energy and spatial acceptance) of $(0.31^{+0.11}_{-0.10} \pm 0.05)\%$.

14.60.Pq, 13.15.+g

1. INTRODUCTION

1.1 Motivation

This paper describes the evidence for neutrino oscillations from the Liquid Scintillator Neutrino Detector (LSND) apparatus described in reference [1]. The result of a search for $\bar{\nu}_\mu \rightarrow \bar{\nu}_e$ oscillations has been reported [2] for data taken in 1993 and 1994 in this experiment, where an excess of events consistent with neutrino oscillations was observed. The purpose of the present paper is to provide details of that analysis which can not be covered in a Letter publication. In addition, data taken in 1995 have been included. Also, further work has shown ways in which the analysis can be made more efficient so that the data sample can be increased, with the result that the beam excess is now sufficiently large that it cannot be due to a statistical fluctuation of the beam-off background. The excess must be due to neutrino oscillations or to an unknown neutrino source or interaction with a very similar signature.

The existence of neutrino oscillations would imply nonconservation of lepton family number and different neutrino mass eigenstates. In the standard model the neutrinos are massless. Observation of neutrino oscillations would require an extension of the standard model and could help in leading to a more encompassing theory. In addition, since there are about 10^2cm^{-3} neutrinos of each family left over from the initial expansion of the universe, neutrino mass of even a few eV would have profound effects on the development of structure in the universe.

There are hints of neutrino mass from observations of both solar and atmospheric neutrinos. Solar models predict more neutrinos from the sun than are detected in four experiments of three quite different types [3–6]. Solving this problem solely by adjusting solar models requires disregarding at least two of the three types of experiment. Neutrino oscillations provide a quantitative explanation of this deficit of electron neutrinos (ν_e), requiring that the difference in the square of the masses (Δm^2) of the neutrinos involved be very small,

$\lesssim 10^{-5}\text{eV}^2$ from the implied energy dependence of the deficit. In the atmospheric neutrino case, three experiments find the ratio of muon to electron neutrinos (ν_μ/ν_e) produced by secondary cosmic ray interactions to be about 60% of that expected [7–10], and this can be explained by $\nu_\mu \rightarrow \nu_e$ or $\nu_\mu \rightarrow \nu_\tau$ oscillations with large mixing. One of these experiments [8] infers a Δm^2 of $\sim 10^{-2} \text{ eV}^2$. However, the (ν_μ/ν_e) ratio observed by the three experiments can be explained by larger values of Δm^2 .

This experiment deals with a range of Δm^2 values that is much larger than that applied to the solar neutrino case. It is perhaps possible [11] to explain both the atmospheric neutrino effect and this LSND result by the same Δm^2 . Although this paper reports strong evidence for neutrino oscillations, more experimental data will be needed to firmly establish the existence of neutrino oscillations and to clarify any relationship among these several indications of oscillations.

1.2 Experimental Method

LSND was designed to detect neutrinos originating in a proton target and beam stop at the Los Alamos Meson Physics Facility (LAMPF), and to search specifically for both $\bar{\nu}_\mu \rightarrow \bar{\nu}_e$ and $\nu_\mu \rightarrow \nu_e$ transitions with high sensitivity. This paper focuses on the first of these two complementary searches. The neutrino source and detector are described in detail in [1]. First results on the $\bar{\nu}_e$ search have been reported in [2], using data collected in 1993 and 1994.

For the experimental strategy to be successful, the beam stop is required to be a copious source of $\bar{\nu}_\mu$, while producing relatively few $\bar{\nu}_e$ by conventional means in the energy range of interest. The detector must be able to recognize interactions of $\bar{\nu}_e$ with precision and separate them from other neutrino types, including a large expected flux of ν_e . The observation of $\bar{\nu}_e$ in excess of the number expected from conventional sources is interpreted as evidence for neutrino oscillations. However, although in this paper we will concentrate on the oscillation hypothesis, it must be noted that any exotic process that creates $\bar{\nu}_e$ either at production, in

flight, or in detection can produce a positive signal in this search. Lepton number violation in muon decay, $\mu^+ \rightarrow e^+ + \bar{\nu}_e + \nu_x$, is a good example and would require an extension of the standard model.

The high flux of protons on the water target produced pions copiously [1]. Most of the positive pions came to rest and decayed through the sequence

$$\begin{aligned}\pi^+ &\rightarrow \mu^+ + \nu_\mu \quad , \\ \mu^+ &\rightarrow e^+ + \nu_e + \bar{\nu}_\mu \quad ,\end{aligned}$$

supplying $\bar{\nu}_\mu$ with a maximum energy of 52.8 MeV. The energy dependence of the $\bar{\nu}_\mu$ flux from decay at rest (DAR) is very well known, and the absolute value is known to 7% [1,12]. The open space around the target is short compared to the pion decay length, so only a small fraction of the π^+ (3.4%) decay in flight (DIF) through the first reaction. A much smaller fraction (approximately 0.001%) of the muons DIF, due to the difference in lifetimes and the fact that a π^+ must first DIF.

The symmetrical chain starting with π^- might lead to an intolerable number of $\bar{\nu}_e$, but three factors result in a large suppression of this background. First, for the LAMPF proton beam and beam stop configuration, positive pion production exceeds that of negative pions by a factor of about eight. Second, negative pions which come to rest in the beam stop are captured through strong interactions before they can decay, so only the 5% which DIF can contribute to a $\bar{\nu}_e$ background. (Note that 5% of π^- and 3.4% of π^+ produced in the beam stop decay in flight.) Third, virtually all of the negative muons arising from such pion DIF come to rest in the beam stop before decaying. Most are captured from atomic orbit, a process which leads to a ν_μ but no $\bar{\nu}_e$, leaving only 12% of them to decay into $\bar{\nu}_e$. Hence one can estimate the relative yield, compared to the positive channel, to be $\sim (1/8) * 0.05 * 0.12 \approx 7.5 \times 10^{-4}$. Thus, it is expected that $\bar{\nu}_e$ are present only at this level in the isotropic flux of neutrinos from the source. A detailed Monte Carlo simulation [12] gives a value of 7.8×10^{-4} for the ratio of $\bar{\nu}_e$ from μ^- DAR to $\bar{\nu}_\mu$ from μ^+ DAR.

It is, however, necessary to deal with the DAR ν_e produced one-for-one with the desired

$\bar{\nu}_\mu$. Although it is not possible to distinguish an e^- from an e^+ , the key to rejecting these ν_e as a background to the $\bar{\nu}_e$ search is the presence of free protons (hydrogen) in the detector. LSND detects $\bar{\nu}_e$ via

$$\bar{\nu}_e + p \rightarrow e^+ + n \quad ,$$

a process with a well-known cross section [13], followed by the neutron-capture reaction

$$n + p \rightarrow d + \gamma(2.2 \text{ MeV}) \quad .$$

Thus the detection signature consists of an “electron” signal, followed by a 2.2 MeV photon correlated with the electron signal in both position and time. Detection of ν_e in LSND is dominated by charged current reactions on ^{12}C . But an electron from $\nu_e^{12}\text{C} \rightarrow e^- \text{ }^{12}\text{N}$ with a DAR ν_e has energy $E_e < 36 \text{ MeV}$ because of the mass difference of ^{12}C and ^{12}N . Moreover, the production of a correlated photon via $\nu_e^{12}\text{C} \rightarrow e^- n \text{ }^{11}\text{N}$ can likewise occur only for $E_e < 20 \text{ MeV}$ because of the threshold for free neutron production. Hence, the ν_e background is greatly suppressed by neutron detection for $E_e > 20 \text{ MeV}$. In addition, the requirement of a minimum e^\pm energy of 36 MeV eliminates most of the ν_e background due to an *accidental* coincidence with an uncorrelated γ signal.

The detector is a tank filled with 167 metric tons of dilute liquid scintillator, located about 30 m from the neutrino source, and surrounded on all sides except the bottom by a liquid scintillator veto shield. The dilute mixture allows the detection in photomultiplier tubes (PMTs) of both Čerenkov light and isotropic scintillation light, so that reconstruction software provides robust particle identification (PID) for e^\pm along with the event vertex and direction. The electronics and data acquisition systems are designed to detect related events separated in time. This is necessary both for neutrino induced reactions and for cosmic ray backgrounds. The response of the detector in the energy range for the $\bar{\nu}_\mu \rightarrow \bar{\nu}_e$ search is calibrated using a large sample of Michel e^\pm from the decays of stopped cosmic ray muons. The response to 2.2 MeV photons is understood by studying the capture of cosmic ray neutrons.

Despite $\sim 2 \text{ kg/cm}^2$ of “overburden” shielding above the detector, there remains a very

large background to the oscillation search due to cosmic rays, which needs to be suppressed by about nine orders of magnitude to reach a sensitivity limited by the neutrino source itself. The cosmic ray muon rate through the tank is ~ 4 kHz, of which $\sim 10\%$ stop and decay in the scintillator, whereas even if every $\bar{\nu}_\mu$ oscillated to $\bar{\nu}_e$, the total rate of $\bar{\nu}_e p$ interactions in the entire tank would be < 0.01 Hz. There are five lines of attack in removing this background. First, an in-time veto rejects muons, but decay e^\pm remain, along with neutrons and a small fraction of unvetoesd muons due to veto shield inefficiency. Second, these e^\pm are greatly reduced by imposing a veto on any event that occurs soon after a specific number of PMT hits in the detector or veto shield. A trigger threshold at 7 muon lifetimes is increased in analysis to as much as 18 muon lifetimes. Third, cosmic ray-induced neutrons are strongly suppressed by use of e^\pm PID criteria, based upon timing, vertex, and direction information from the detector. Fourth, the requirement of a correlated capture γ discriminates against cosmic ray particles other than neutrons. Fifth, the level of remaining cosmic ray background is very well measured because about 14 times as much data are collected when the beam is off as on. The result of these procedures is to reduce cosmic ray particles to a small background for the DAR oscillation search.

1.3 Outline of This Paper

We present a brief description of the detector system and data collection in chapter two. Chapter three describes the methodology of identifying 2.2 MeV γ s associated with neutron capture on free protons. Chapter four describes event selection and acceptance. Chapter five contains an assessment of neutrino backgrounds. Distributions of data are shown in chapter six, and fits to the data are discussed in chapter seven. An interpretation of the data in terms of neutrino oscillations is given in chapter eight, together with a comparison with other neutrino oscillation experiments.

2. DETECTOR AND DATA COLLECTION

2.1 Overview

Reference [1] contains a detailed description of the neutrino source and detector and a discussion of detector performance. Here the detector is described briefly in section 2.2 and the veto shield in section 2.3.

2.2 Detector and Data Collection

This experiment is carried out at LAMPF using 800 MeV protons from the linear accelerator. Pions were produced from 14772 Coulombs of proton beam at the primary beam stop over three years of operation between 1993 and 1995. There were 1787 Coulombs in 1993, 5904 Coulombs in 1994, and 7081 Coulombs in 1995. The fraction of the total DAR neutrino flux produced in each of the three years was 12% in 1993, 42% in 1994, and 46% in 1995 and varied slightly from the Coulomb fractions due to small variations in the beam stop geometry. The duty ratio is defined to be the ratio of data collected with beam on to that with beam off. It averaged 0.070 for the entire data sample, and was 0.076, 0.080, and 0.060 for the years 1993, 1994, and 1995, respectively. The primary beam stop consists of a 30 cm water target surrounded by steel shielding and followed by a copper beam dump. The DAR neutrino flux varies approximately as r^{-2} from the average neutrino production point, where r is the distance traveled by the neutrino. The detector is located 30 m from this main production target, while two thinner subsidiary targets are located approximately 75 m and 100 m farther upstream.

The detector is a roughly cylindrical tank containing 167 tons of liquid scintillator and viewed by 1220 uniformly spaced 8" Hamamatsu PMTs. The digitized time and pulse height of each of these PMTs (and each of the 292 veto shield PMTs) are recorded when the deposited energy in the tank exceeds a threshold of about 4 MeV (electron equivalent energy) with less than 4 veto PMT hits. Activity in the detector or veto shield during

the 51.2 μs preceding a primary trigger is also recorded, provided there are > 17 detector PMT hits or > 5 veto PMT hits. Data after the primary are recorded for 1 ms with a threshold of about 0.7 MeV. The detector operates without reference to the beam spill, but the state of the beam is recorded with the event. Approximately 93% of the data is taken between beam spills. This allows an accurate measurement and subtraction of cosmic ray background surviving the event selection criteria. The detector scintillator consists of mineral oil (CH_2) in which is dissolved a small concentration (0.031 g/l) of b-PBD [14]. This mixture allows the separation of Čerenkov light and scintillation light and produces about 33 photoelectrons per MeV of electron energy deposited in the oil. The combination of the two sources of light provides direction information and makes PID possible for relativistic particles. Identification of neutrons is accomplished through the detection of the 2.2 MeV γ from neutron capture on free protons. Note that the oil consists almost entirely of carbon and hydrogen. The fractional mass of oxygen and nitrogen in the oil from the b-PBD (0.031 g/l of $C_{24}H_{22}N_2O$) and the vitamin E added as a preservative (0.010 g/l of $C_{19}H_{28}O$) is about 2×10^{-6} and 3×10^{-6} , respectively. Also, nitrogen is bubbled through the oil continually to remove oxygen that can decrease the oil's attenuation length. However, the fractional mass due to this nitrogen is $\ll 10^{-6}$.

2.3 Veto Shield

The veto shield encloses the detector on all sides except the bottom. Additional counters were placed below the veto shield after the 1993 run to reduce cosmic ray background entering through the bottom support structure. The main veto shield [15] consists of a 15-cm layer of liquid scintillator in an external tank and 15 cm of lead shot in an internal tank. This combination of active and passive shielding tags cosmic ray muons that stop in the lead shot. A veto inefficiency $< 10^{-5}$ is achieved with this detector for incident charged particles. The veto inefficiency is larger for incident cosmic-ray neutrons.

3. CORRELATED PHOTONS FROM NEUTRON CAPTURE

3.1 Overview

The performance of the detector in the detection of 2.2 MeV γ s from neutron capture on free protons is discussed in this chapter. Neutrons produced in the reaction $\bar{\nu}_e p \rightarrow e^+ n$ are identified by detection of the subsequent 2.2 MeV γ from the reaction $n + p \rightarrow d + \gamma$. These recoil neutrons are produced with kinetic energy in the 0 to 5.2 MeV energy range and typically travel about 10 cm before capture. The expected mean capture time of 186 μ s is essentially independent of the initial neutron energy because the time taken for the neutron to degrade to less than 1 MeV is small compared to 186 μ s. The detector performance is measured empirically from a large sample of cosmic ray neutron events which appear in the main detector and are discussed in section 3.2. The energy and position reconstruction of 2.2 MeV γ s is discussed in section 3.3. Properties of 2.2 MeV γ candidates and accidental γ background are discussed in section 3.4. A Monte Carlo simulation for correlated low-energy neutrons is discussed in section 3.5. The likelihood parameter that is used to separate correlated and accidental γ s is described in section 3.6.

3.2 Cosmic Ray Neutron Sample

A cosmic ray neutron sample is obtained with the following selection criteria: deposited electron equivalent energy between 36 and 60 MeV, PID consistent with a neutron (satisfying $\chi_{tot} > 0.8$ and $\chi_r < 0.75$, to reduce events with multiple neutrons, where χ_{tot} and χ_r are described in section 4.2), less than 4 veto hits within the 0.5 μ s event window, beam off, and at least one triggered γ event within 1 ms of the primary event. Charged particles below Čerenkov threshold produce less light per energy deposited than do $\beta \sim 1$ electrons. Also, neutrons deposit much of their energy by scattering from protons and nuclei. The energy scale used in this paper is based on the light-to-energy ratio for electrons. Fig. 1 shows the time difference between neutrons that satisfy the above criteria and a subsequent γ with 21

to 50 hit PMTs. The distribution is fit to a sum of an exponential for correlated γ s and a flat background for accidental γ s (solid curve). The fitted time constant of $188 \pm 3 \mu\text{s}$ agrees well with the $186 \mu\text{s}$ capture time for neutrons in mineral oil. The γ s in the last $250 \mu\text{s}$ of the 1 ms window are almost entirely accidental γ s and are used to define the characteristics of the “accidental γ ” sample. Similarly, a “correlated γ ” sample is defined to contain a γ in the first $250 \mu\text{s}$ of the 1 ms window after subtraction of the accidental γ contribution (see section 3.4).

3.3 Gamma Reconstruction Algorithm

Activities with 21 to 50 hit PMTs, with average charge per PMT hit greater than 0.8 photoelectrons, and which occur within 1 ms of the primary event are defined to be γ candidates and are fit for position with a special reconstruction algorithm. The algorithm defines the γ position to be the average of the position of all hit PMTs weighted by the pulse height of each PMT. This algorithm, although simple, results in a position error which is comparable to (or better than) some more elaborate methods (see section 3.4).

3.4 Properties of Photon Candidates

3.4.1 Correlated and Accidental Photons

In Fig. 2 is shown the observed distributions of photons from the “correlated γ ” (solid curve) and “accidental γ ” (dashed curve) samples. The distributions are: (a) the time of the γ after the primary; (b) the number of photon PMT hits; (c) the distance of the reconstructed γ from the primary.

These three “correlated γ ” distributions are found to be approximately independent of the primary event location in the fiducial volume. As expected from the uniformity of the oil, there is no correlation between the neutron capture time and the other two variables. Furthermore, the number of photon PMT hits is observed to be independent of distance

from the primary, except for a small correlation for distances beyond 2 m. Events with fewer PMT hits have a slightly broader distance distribution, which is expected because the position correlation of the γ and primary vertex is dominated by reconstruction errors. However, the observed distance distribution from the cosmic ray neutron sample is broader than expected for neutrons from the reaction $\bar{\nu}_e + p \rightarrow e^+ + n$ because the primary arises from an initial neutron interaction of higher energy and thus travels slightly farther before reaching thermal energies. Monte Carlo studies (see section 3.5) indicate that the mean measured distance distribution is up to 20 cm larger on average than for the low-energy neutrons of interest.

The dependence of the three “accidental γ ” distributions on primary event locations was also investigated. For this study the reconstructed γ position was required to be within 2.5 m of the primary vertex, a criterion imposed in the γ identification procedure described later. The three distributions are uniform over the fiducial volume except near the bottom, upstream corner of the detector (see section 3.4.2), where there is a higher rate of accidental γ s. For primary events in this region, both the number of photon PMT hits and the distance distribution have lower average values than elsewhere in the detector.

3.4.2 Spatial Distributions of Accidental Photons

The reconstructed position for accidental γ s in the X - Z and Y - Z projections is shown in Fig. 3. The coordinate system is defined such that Y is pointing up in the vertical direction and Z is pointing downstream along the cylindrical axis of the detector. These distributions are non-uniform and show a concentration near the upstream, bottom portion of the detector. This concentration may be due to steel shielding underneath the detector with a high level of radioactivity or to a cable penetration through the veto system in that region. This non-uniformity is taken into account in the fit analyses of chapter 7. The average accidental γ rate over the entire detector is 1.07 ± 0.01 kHz in 1993, 1.19 ± 0.01 kHz in 1994, and 1.14 ± 0.01 kHz in 1995.

3.5 Monte Carlo Simulation of Photons From Neutron Capture

Cosmic ray neutrons selected are of higher energy than those from the neutrino oscillation reaction $\bar{\nu}_e p \rightarrow e^+ n$. Thus, the distance of the reconstructed photon from the primary is on average shorter for the neutrino oscillation reaction than it is for cosmic ray neutrons. In order to compute the expected distance distribution between the reconstructed e^+ and the 2.2 MeV γ , three Monte Carlo distance distributions were used. (1) Positrons of the expected energy distribution were generated and passed through the Monte Carlo detector simulation [1,16] and reconstruction to find the distribution of distances between the e^+ point of origin and reconstructed position. (2) A separate Monte Carlo program designed to track low energy neutrons was used to find the distribution in distance between neutron production and capture. This program simulated elastic scattering from the carbon and hydrogen atoms according to tabulated neutron cross sections. Neutrons were tracked even after they have thermalized, at which point it becomes important that neutron absorption with resulting γ production on hydrogen and carbon was also included. (3) The detector simulation is used to simulate scintillation light produced by the 2.2 MeV γ . Two extra single photoelectron hits were randomly added to the hit PMTs to simulate PMT noise, which is based on the average PMT noise rate of about 3 kHz. The photon reconstruction algorithm described in section 3.3 was used to compute the γ position, from which the distance between the generated and reconstructed photon is obtained.

The expected distribution in distance between the reconstructed e^+ and the 2.2 MeV γ is the convolution of these three distributions and is shown as the solid histogram in Fig. 4. This distribution is dominated by reconstruction errors in the γ position. The travel distance of low energy neutrons, e^+ reconstruction position error, and PMT noise contribute little to the overall distance distribution. Hence, the distribution is narrower, as expected, but not vastly different from that obtained in section 3.4 from cosmic ray neutrons, shown as the dashed histogram in Fig. 4. We use both distributions for the fits described in chapter 7 and obtain similar results.

3.6 Photon Identification Parameter (R)

The three “correlated γ ” distributions in Fig. 2 are used to determine the likelihood, \mathcal{L}_c , that the γ is correlated with the primary event. Similarly, the three “accidental γ ” distributions in Fig. 2 are used to determine the likelihood, \mathcal{L}_a , that the γ is accidental and uncorrelated with the primary event. Each likelihood, therefore, is the product of the three probability densities, $\mathcal{L} = P(hits) \times P(\Delta r) \times P(\Delta t)$. A likelihood ratio, R , for the event is then defined as the ratio of these likelihoods, $R \equiv \mathcal{L}_c/\mathcal{L}_a$. Because of the small correlations described in section 3.4.1 and the adjustment to the Δr distribution discussed in section 3.5, these \mathcal{L} s are only approximate likelihoods. Moreover, R does not allow for the variation of accidental rates with the position of the primary particle. Nonetheless, R is a very powerful tool for separating correlated from uncorrelated γ s, and the Δr and rate effects are fully allowed for in the fitting procedures to be described later in this paper.

Fig. 5 shows the measured R distribution for events with the γ correlated (solid) and uncorrelated (dashed) with the primary event. As expected, the uncorrelated events are concentrated at low values of R . For events with multiple γ s, the γ with the maximum R is used. R is set to 0 for events without a γ that reconstructs within 2.5 m of the primary, has 21 to 50 PMT hits, and occurs within 1 ms of the primary event. The definition of R is always based on the spectra of Fig. 2, using the Δr distribution measured from cosmic ray neutrons. However, if Δr for correlated photons is actually distributed as given by the Monte Carlo calculation of Section 3.5, then the distribution of R for correlated photons will be given by the dotted curve in Fig. 5 instead of the solid histogram. Both versions are tried for the fits to be described in Section 7.1. It should also be noted that while the accidental photon spectrum shown in Fig. 5 is averaged over primary event locations in the fiducial volume, those fits actually use a spectrum which takes the local accidental rate into account.

The efficiency for producing and detecting a 2.2 MeV correlated γ within 2.5 m, with 21 to 50 PMT hits, and within 1 ms was determined to be $63 \pm 4\%$ (using the solid curve

of Fig. 5. This efficiency is the product of the probability that the γ trigger is not vetoed by a veto shield signal within the previous $15.2 \mu s$ ($82 \pm 1\%$), the data acquisition livetime ($94 \pm 3\%$, lower for γ s than for primary events), the requirement that the γ occurs between $8 \mu s$ and $1000 \mu s$ after the primary event ($95 \pm 1\%$), the requirement that the γ has between 21 and 50 hit PMTs ($90 \pm 4\%$), and the requirement that the γ reconstructs within 2.5 m of the primary event ($96 \pm 2\%$). From the cosmic-ray Michel electron data, the average probability of finding an accidental uncorrelated γ within the same cuts is $28 \pm 2\%$. The R distributions shown in Fig. 5 are then used to determine the efficiencies for finding a correlated or uncorrelated γ satisfying a particular R criterion. For example, the efficiency that an accidental γ satisfies $R > 30$ (1.5) is 0.6% (9.0%), while the efficiency for a correlated γ is 23% (58%). The accidental rate depends on the position of the primary event within the fiducial volume, as seen in Fig. 3. However, Fig. 6 shows that the R distributions are almost identical for $R > 0$ in each of the four quadrants of the Y - Z plane for correlated γ s (solid) and accidental γ s (dashed).

4. EVENT SELECTION AND EFFICIENCY

4.1 Overview

The signature for the principal oscillation search is two-fold – a positron and a correlated 2.2 MeV γ . The analysis is performed for two ranges of positron energy. In order to establish the presence of an excess, the positron is required to be in the energy range $36 < E_e < 60$ MeV, where the known neutrino backgrounds are small. A looser energy requirement, $20 < E_e < 60$ MeV, provides a larger range of L/E_ν and is used to determine the oscillation probability and the Δm^2 vs $\sin^2 2\theta$ allowed range. Isolation of an oscillation signal in this experiment thus consists of PID of the positron from the reaction $\bar{\nu}_e p \rightarrow e^+ n$ (without distinguishing between positrons and electrons) and positive identification of the associated neutron by the presence of a correlated 2.2 MeV γ from the reaction $np \rightarrow d\gamma$. Backgrounds

then fall into three categories. Two of them are beam-related, the first involving events which include a primary particle identified as an e^\pm plus a correlated neutron-capture signal, and the second involving events with an accidental γ signal instead of a correlated neutron. The largest category of backgrounds is from beam-unrelated cosmic rays. While the latter are eventually subtracted statistically using beam-off data, the strategy for positron selection is to reduce these backgrounds to a low level before making the subtraction. These positron selection criteria are described in this chapter. The tools for selecting associated neutrons have been presented in chapter 3 and are applied to event selection in chapters 6 and 7.

4.2 Positron Selection

The positron selection criteria and efficiencies are summarized in Table I for two different selections. Selection I is identical to what has been used previously [2], while selection VI makes use of additional criteria which reduce the beam-off background and increase the acceptance. Selections II - V are variations of selections I and VI and are discussed at the end of the chapter.

To establish an event excess, positrons are required to have an energy in the $36 < E_e < 60$ MeV range. The narrow energy range is chosen, as shown in Fig. 7, because it is above the $\nu_e \text{ }^{12}\text{C} \rightarrow e^- \text{ }^{12}\text{N}$ endpoint and in the range expected for oscillation events.

The primary particle is required to have a PID consistent with a positron. Particles with velocities well above Čerenkov threshold are separated from particles below Čerenkov threshold by making use of the four χ parameters defined in reference [1]. Briefly, χ_r and χ_a are the quantities minimized for the determination of the event position and direction, χ_t is the fraction of PMT hits that occur more than 12 ns after the fitted event time, and χ_{tot} is proportional to the product of χ_r , χ_a , and χ_t . Fig. 8 shows the four χ parameters for samples of Michel electrons (solid) and cosmic-ray neutrons (dashed) with electron energies in the $36 < E_e < 60$ MeV range. For a neutron, E_e is the equivalent electron energy corresponding to the observed total charge. The Michel electrons are identified by their correlation with

a parent muon, while the neutrons are identified by their correlation with a 2.2 MeV γ from np capture. By requiring that the χ parameters satisfy $0.3 < \chi_{tot} < 0.66$, $\chi_r < 0.61$, $\chi_a < 0.20$, and $\chi_t < 0.26$ ($0.3 < \chi_{tot} < 0.65$, $\chi_r < 0.60$, $\chi_a < 0.19$, and $\chi_t < 0.25$ for selection I), optimal separation is obtained between electrons and particles below Čerenkov threshold. (For example, neutrons are reduced by a factor of $\sim 10^3$.) The lower limit on χ_{tot} is imposed to eliminate any laser calibration events that are not correctly identified. The overall PID efficiencies for positrons in the $36 < E_e < 60$ MeV energy range are 0.77 ± 0.02 and 0.84 ± 0.02 for selections I and VI, respectively. The PID efficiencies increase with energy, as shown in Fig. 9. The PID efficiency in the $20 < E_e < 36$ MeV energy range is 0.62 ± 0.02 for selection VI. There is some variation of PID efficiency with position in the detector, and the efficiencies above are averaged over the detector fiducial volume.

In order to eliminate Michel electrons from muon decay, the time to the previous triggered event, Δt_p , is required to be greater than $40 \mu s$ for selection I and greater than $20 \mu s$ for selection VI. For selection VI, all activities between $20 \mu s$ and $34 \mu s$ before the event trigger time are required to be uncorrelated with the positron by having fewer than 50 PMT hits and a reconstructed position more than 2m from the positron position. Fig. 10 shows the Δt_p distribution of beam-off events that satisfy the other positron selection criteria for (a) events with no Δt_p requirement and (b) events after imposing the above criteria for no correlated activities within $34 \mu s$. Note the reduction in the beam-off events shown in the figure between 20 and $34 \mu s$. The locations of the $20 \mu s$ and $34 \mu s$ requirements are shown on the figure. Note that the $20 \mu s$ requirement, corresponding to $10 \mu^-$ lifetimes and $9 \mu^+$ lifetimes in oil, allows a negligible amount of background from $\nu_\mu C \rightarrow \mu^- X$ scattering. The remaining small cosmic ray background after these cuts is eliminated by beam on-off subtraction. The selection I and VI efficiencies are 0.50 ± 0.02 and 0.68 ± 0.02 , respectively.

It is required that the number of veto shield hits associated with the events is less than 2 for selection I (0.84 ± 0.02 efficiency) and less than 4 (the hardware trigger requirement) for selection VI (0.98 ± 0.01 efficiency) to reduce cosmic ray backgrounds.

The reconstructed positron location is required to be a distance D of at least 35 cm from

the surface tangent to the faces of the PMTs. This cut provides assurance that the positron is in a region of the tank in which the energy and PID responses vary smoothly and are well understood; charge response, energy resolution and PID efficiencies all degrade near and behind the PMTs. (For the 1993 data a 40 cm requirement is used due to the absence of additional veto counters placed below the veto shield.) Fig. 11 shows that, for Michel electrons generated behind the PMT surface by the Monte Carlo simulation, no more than $\approx 1\%$ are reconstructed with $D > 35$ cm and with more than 150 PMT hits. This results in a negligible background of $\nu_\mu C$ scattering events in which the muon is missed because it is behind the PMT surface. The 35 cm cut also avoids the region of the tank with the highest cosmic ray background, thus reducing the statistical error from having to subtract that background.

The time to any subsequent triggered event is required to be $> 8 \mu s$ to remove events that are muons that decay. (A high energy muon above Čerenkov threshold has a small probability for satisfying the PID criteria.) By requiring no subsequent event within four μ^- lifetimes, this background is almost completely eliminated.

To further suppress cosmic ray neutrons, the number of associated γ s with $R > 1.5$ (see chapter 3) is required to be less than 3 for selection I (0.99 ± 0.01 efficiency) and less than 2 for selection VI (0.94 ± 0.01 efficiency). Cosmic ray neutrons that enter the detector often produce one or more additional neutrons, while recoil neutrons from the $\bar{\nu}_e p \rightarrow e^+ n$ reaction are too low in energy to knock out additional neutrons. Fig. 12 shows the number of associated γ s with $R > 1.5$ for beam-off background events of $R > 30$ in the $36 < E_e < 60$ MeV energy range with at least one γ (dashed), compared to the expectation (based on the measured rate of accidental γ s in the tank) for oscillation events (solid). About 94% of the expected oscillation events and only 60% of the beam-off background events with $R > 30$ have less than 2 associated γ s.

For events that pass the electron selection criteria above, beam-off data are different from the expected neutrino interaction signal in two respects. The first of these is the distribution of $\vec{r} \cdot \hat{dr}$, where \vec{r} is the location of the reconstructed event with respect to the center of the

tank, and $\hat{d}r$ is the unit direction of the event in the same coordinate system. This scalar product gives large negative values for events near the edge of the fiducial volume that head toward the center of the tank. In the dashed line of Fig. 13, the $\vec{r} \cdot \hat{d}r$ distribution for the beam-off sample is shown. As expected for events originating outside the fiducial volume, the distribution is peaked at large negative values. For neutrino events on the other hand, the distribution is much more symmetric about the origin. This is illustrated by the solid line of Fig. 13, which shows the $\vec{r} \cdot \hat{d}r$ distribution for a sample of $\nu_e C$ scattering events. (Note that $\vec{r} \cdot \hat{d}r$ does not depend on energy.)

The number of hits in the veto system is also observed to be different from that expected from signal. The number of veto hits in the beam-off sample is displayed in the dashed line of Fig. 14, while the number expected (from accidental coincidences) in the signal is shown in the solid line. (This last distribution is measured by looking at the number of veto hits in coincidence with random firing of the laser flasks [1].)

Using the distributions of these two variables, the likelihoods \mathcal{L}_{off} and \mathcal{L}_{on} are calculated that a given event is due to beam-off background or to beam-on signal, respectively. The ratio of these likelihoods ($S = \mathcal{L}_{on}/\mathcal{L}_{off}$) is plotted for the $\nu_e C$ and beam-off samples in Fig. 15. (Note that the bias caused by using the beam-off data sample for both the S determination and to correct for cosmic-ray background in the beam-on sample has been shown by Monte Carlo simulations to be negligible.) A cut at $S > 0.5$ is 87% efficient for neutrino-induced events, while eliminating 33% of the beam-off background. This cut is used only for selection VI and completes the positron selection criteria.

4.3 Efficiencies of Positron Selection Criteria

The efficiencies for selection VI are summarized below. The efficiency of the PID selection criteria for positrons is measured using the Michel electron sample. The resulting PID selection efficiency is about $84 \pm 2\%$. The requirement that the time to the previous triggered event is greater than $20 \mu s$ and the time to any correlated activity is greater than $34 \mu s$ has

an efficiency of $68 \pm 2\%$. The veto shield hit requirement has an efficiency of $98 \pm 1\%$, as determined from laser calibration events. Because all event yield calculations are based upon the number of target atoms inside the 35 cm fiducial volume cut, an efficiency correction of $85 \pm 5\%$ is applied to allow for the tendency of the position reconstruction algorithm to push events toward the PMT surfaces [1]. Additional efficiencies result from the requirement of no triggered event within $8 \mu\text{s}$ in the future after the primary event to eliminate muon decays ($99 \pm 1\%$), the requirement of < 2 associated γ s with $R > 1.5$ ($94 \pm 1\%$), the $S > 0.5$ requirement ($87 \pm 2\%$), and the data acquisition system livetime ($97 \pm 1\%$). The overall positron selection efficiency is $37 \pm 3\%$, and is higher than the $26 \pm 2\%$ efficiency (see Table I) obtained with selection I. Selection V is defined to be the same as selection VI but without the $S > 0.5$ requirement, while selection IV is defined to be the same as selection V but without the < 2 associated γ requirement. Selection II is the same as selection I but with the looser PID criteria, and selection III is the same as selection II but with the looser veto hits less than 4 requirement. Selections II - V have positron selection efficiencies of $28 \pm 2\%$, $33 \pm 3\%$, $45 \pm 3\%$, and $43 \pm 3\%$, respectively.

5. BEAM-RELATED BACKGROUNDS

5.1 Beam-Related Backgrounds with a Correlated γ

Beam-related backgrounds with neutrons are estimated individually in the $36 < E_e < 60$ MeV energy range before the correlated γ requirement is imposed. Table II lists the backgrounds in the above energy range for $R \geq 0$ (the full positron sample) and $R > 30$, while Table III lists the backgrounds for the $20 < E_e < 60$ MeV energy range. Selection criterion VI, defined in chapter 4, is used, and backgrounds for other selection criteria can be obtained by multiplying by the relative efficiencies. The DAR and DIF neutrino fluxes have been estimated by a detailed beam Monte Carlo simulation [12]. Uncertainties in the efficiency, cross section, and DIF ν flux lead to systematic errors of between 20 and 50% for

the backgrounds discussed below.

5.1.1 Neutrons Entering the Detector

Despite the amount of shielding between the beam dump and the detector, one must consider the possibility, nonetheless, that neutrons from the target could find their way into the tank. A limit on the beam neutron background relative to the cosmic neutron background is set by looking for a beam-on minus beam-off excess of neutron events in the 40 – 180 MeV electron equivalent energy range. This comparison is made by examining neutron candidates which pass neutron, rather than e^+ , PID criteria. For events with $\chi_{tot} > 0.75$ and an associated 2.2 MeV γ within 1.5 m and 0.5 ms, 89700 beam-off events and 6915 beam-on events are observed in a partial data set with a duty ratio of 0.075, implying an excess of 187.5 ± 86.1 events. This excess of events is consistent with the ~ 200 events expected from $\nu C \rightarrow \nu n X$ scattering. However, even if the entire excess is interpreted as beam neutrons entering the tank, fewer than $187.5/6915 = 3\%$ of the beam-on events are actually beam-related. Applying this same ratio for neutrons *passing* the e^+ PID criteria, the beam-related neutron background in the e^+ sample is less than 0.03 times the number of beam-unrelated neutrons. Based upon the R distribution of the beam-off data sample, less than 15% of beam-unrelated events in the selected e^+ sample are due to neutrons. Hence the beam-related neutron background is less than 0.005 times the total beam-unrelated background, and is negligible.

5.1.2 $\bar{\nu}_e$ from Standard Processes

The largest beam-related background with a correlated neutron is due to $\bar{\nu}_e$ produced in the beam stop by conventional processes. Such events are detected in the same way as oscillation candidates, via $\bar{\nu}_e p \rightarrow e^+ n$. Their most important source is the DAR of μ^- in the beam stop. As outlined in section 1.2, the $\bar{\nu}_e$ flux from μ^- decay is suppressed by more than three orders of magnitude compared to the $\bar{\nu}_\mu$ flux from μ^+ decay. Another possible source

of $\bar{\nu}_e$, the direct decay of $\pi^- \rightarrow e^- \bar{\nu}_e$, is negligible, as a consequence of its low branching ratio (1.2×10^{-4}), the 1/8 ratio of π^- to π^+ in the target, and the capture of π^- in the material of the beam dump.

The product of neutrino flux ($6.1 \times 10^{-13} \bar{\nu}_e/cm^2/p$), number of protons on target (9.2×10^{22} , corresponding to 14772 C), average cross section over the entire energy range ($0.72 \times 10^{-40} \text{ cm}^2$) [13], the number of free protons in the fiducial volume (7.4×10^{30}), the fraction of events with $E > 36 \text{ MeV}$ (0.45), and the average positron reconstruction efficiency after cuts (0.36), gives a total background in the full positron sample of 4.8 ± 1.0 events. Note that the positron efficiency is energy dependent. The systematic uncertainty is largely due to that in the $\bar{\nu}_e$ flux [1], but also includes contributions for the efficiency (section 4.3).

The energy-dependence of this background is determined by folding the $\bar{\nu}_e$ spectrum from μ^- DAR (softer than the $\bar{\nu}_\mu$ DAR spectrum and hence of potential oscillation events) with the detection cross section. It is shown in Fig. 16.

A related background is due to $\bar{\nu}_e \text{ } ^{12}\text{C} \rightarrow e^+ \text{ } ^{11}\text{B}n$ scattering. The cross section to the ^{12}B ground state is calculated to be $6.3 \times 10^{-42} \text{ cm}^2$ [17] and the cross section to the $^{11}\text{B}n$ final state must be at least a factor of two smaller, especially because the first four excited states of ^{12}B are stable against neutron emission. Therefore, we estimate that this background is $< 2\%$ of the $\bar{\nu}_e p \rightarrow e^+ n$ background and is negligible. Furthermore, the maximum positron energy from this background is 36.1 MeV, so that almost all of the positron energy spectrum is $< 36 \text{ MeV}$.

5.1.3 Misidentification of $\bar{\nu}_\mu$ Events

The second most important source of beam-related background events with correlated neutrons is the misidentification of $\bar{\nu}_\mu$ charged-current interactions in the tank as $\bar{\nu}_e$ events. Because of the energy needed to produce a μ^+ , such a $\bar{\nu}_\mu$ must arise from a π^- that decays in flight. In the tank it interacts by either $\bar{\nu}_\mu p \rightarrow \mu^+ n$ or (less often) $\bar{\nu}_\mu \text{C} \rightarrow \mu^+ n X$, followed by $\mu^+ \rightarrow e^+ \nu_e \bar{\nu}_\mu$. There are four possible reasons for the misidentification.

First, the muon can be missed because the deposited energy is below the 18 phototube threshold for activity triggers. This is either because the muon is too low in energy or is produced behind the phototube surfaces. The detector Monte Carlo simulation is used to show that this threshold corresponds to a μ^- kinetic energy T_μ of 3 to 4 MeV. Since the associated neutron also produces a little light in the tank, the background will be quoted for the case of muons below 3 MeV. Their yield is computed by folding the DIF $\bar{\nu}_\mu$ flux with the charged-current cross sections. The background rate from $\bar{\nu}_\mu p \rightarrow \mu^+ n$ is written as the product of the number of protons on target (9.2×10^{22}), the total $\bar{\nu}_\mu$ flux ($8.7 \times 10^{-12} \bar{\nu}_\mu/\text{cm}^2/p$), the average flux-weighted cross section ($0.70 \times 10^{-40} \text{cm}^2$, including the $\bar{\nu}_\mu$ energy range below threshold) [13], the fraction of μ^+ having $T_\mu < 3 \text{ MeV}$ (0.0215), the number of free protons in the fiducial volume (7.4×10^{30}), the positron efficiency (0.37), and the fraction of events with $36 < E < 60 \text{ MeV}$ (0.58), for a background of 1.9 events. (Note that the positron efficiency varies with energy.) Similar estimates for the backgrounds from $\bar{\nu}_\mu C \rightarrow \mu^+ nX$ and $\nu_\mu C \rightarrow \mu^- nX$ [20] add 0.1 and 0.4 events, respectively, for a total of 2.4 ± 1.2 events. It is estimated [20] that about 80% of the $\bar{\nu}_\mu C \rightarrow \mu^+ X$ and 6% of the $\nu_\mu C \rightarrow \mu^- X$ scattering events will have a recoil neutron. The 50% systematic error includes the uncertainty in the threshold, as well as smaller contributions from the $\bar{\nu}_\mu$ flux and efficiency.

Second, a μ^+ above the hit threshold can be missed if a prompt decay to e^+ caused the muon and electron to be collected in a single event which is then identified as an e^\pm . This effect is considerably suppressed by the χ cuts and the requirement that the reconstructed time be consistent with the triggered event time. The detector Monte Carlo simulation shows that this misidentification only occurs for μ^+ decays within 100 ns, decreases with T_μ , and is almost zero above 10 MeV. Using the Monte Carlo misidentification probabilities, a calculation similar to that above implies a background of 0.20 ± 0.10 events.

Third, the μ^+ can be lost because it is produced behind the PMT surface and the electron radiates a hard γ that reconstructs within the fiducial volume. A background of 0.1 ± 0.1 events is estimated from the Monte Carlo simulation.

Fourth, a muon can be missed by trigger inefficiency. In 1995, we acquired for many online positron triggers complete digitization information for all veto and detector phototubes over the 6 μ s interval prior to the positron. Analysis of these data, discussed in section 7.3.2, shows the trigger inefficiency for low-energy muons to be negligible.

The total background due to misidentified muons is thus 2.7 ± 1.3 events. It has a detected energy spectrum which is very close to that for positrons from μ^+ decay.

5.1.4 Other Backgrounds Considered

Additional backgrounds are from $\bar{\nu}_e$ produced by $\mu^- \rightarrow e^- \nu_\mu \bar{\nu}_e$ and $\pi^- \rightarrow e^- \bar{\nu}_e$ DIF. These $\bar{\nu}_e$ can interact on either C or a free proton to yield the oscillation signature of a positron and a recoil neutron. For $36 < E_e < 60$ MeV, 0.1 ± 0.1 events are estimated. The reactions $\nu_e {}^{12}C \rightarrow e^- n X$ and $\nu_e {}^{13}C \rightarrow e^- n X$ are negligible (< 0.1 events) for $E_e < 36$ MeV and cannot occur for $E_e > 36$ MeV. Other backgrounds, for example $\nu_\mu C \rightarrow \nu_\mu n \gamma X$ with $E_\gamma > 20$ MeV and $\nu_e C \rightarrow e^- p X$ followed by ${}^{13}C(p, n) {}^{13}N$, are also negligible.

5.2 Beam-Related Backgrounds Without a Correlated γ

There are eight beam-related backgrounds without neutrons that are considered (see Tables II and III). Although their total is determined empirically by a fit involving the photon parameter R (see section 7.1), they are also estimated individually in the $36 < E_e < 60$ MeV energy range before the associated γ requirement is imposed. These estimates are outlined below, using positron selection criterion VI as defined in chapter 4.

5.2.1 DIF Backgrounds Without a Correlated γ

The first background is due to π DIF in the beam stop, followed by $\nu_\mu C \rightarrow \mu^- X$ and $\mu^- \rightarrow e^- \nu \bar{\nu}$ in the detector. This background occurs if the muon is missed because it is below the 18 PMT threshold, either because the muon is produced at too low an energy (.005

probability) or behind the PMT surface (.001 probability) or the muon decays promptly so that the muon and electron are considered one particle that pass the PID (.001 probability). The estimated number of events is the sum of the above contributions (.007 probability) multiplied by the ν_μ flux ($6.5 \times 10^{-11} \nu_\mu/\text{cm}^2/\text{p}$), the number of protons on target (9.2×10^{22}), the flux-average cross section ($2.3 \times 10^{-40} \text{ cm}^2$) [18], the electron efficiency (0.39), the fraction of events with $36 < E_e < 60 \text{ MeV}$ (0.58), and the number of ^{12}C atoms in the fiducial volume (3.7×10^{30}), which results in a total of 8.1 ± 4.0 events.

Another background from π DIF is $\nu_\mu e \rightarrow \nu_\mu e$ elastic scattering. The product of neutrino flux, number of protons on target given above, the flux-averaged cross section ($1.4 \times 10^{-43} \text{ cm}^2$), the electron reconstruction efficiency (0.38), the fraction of events with $36 < E_e < 60 \text{ MeV}$ (0.16), and the number of electrons in the fiducial volume (3.0×10^{31}) gives 1.5 ± 0.3 events.

Other backgrounds are due to $\mu^+ \rightarrow e^+ \bar{\nu}_\mu \nu_e$ and $\pi^+ \rightarrow e^+ \nu_e$ DIF followed by $\nu_e C \rightarrow e^- X$ scattering (0.6 ± 0.1 events), and $\pi^+ \rightarrow \mu^+ \nu_\mu$ DIF followed by $\nu C \rightarrow \nu C \pi^0$ coherent scattering [19] (0.2 ± 0.1 events).

5.2.2 DAR Backgrounds Without a Correlated γ

The next background we consider is $\nu_e e \rightarrow \nu_e e$ and $\bar{\nu}_\mu e \rightarrow \bar{\nu}_\mu e$ elastic scattering from μ^+ DAR in the beam stop. Note that ν_μ from π^+ DAR are too low in energy to produce electrons above 36 MeV. The number of events from this source is estimated as the product of the neutrino flux ($7.8 \times 10^{-10} \nu/\text{cm}^2/\text{p}$), the number of protons on target (9.2×10^{22}), the average cross section sum for $\nu_e e$ and $\bar{\nu}_\mu e$ scattering ($3.5 \times 10^{-43} \text{ cm}^2$), the electron reconstruction efficiency (0.38), the fraction of events with $E > 36 \text{ MeV}$ (0.042), and the number of electrons in the fiducial volume (3.0×10^{31}), which results in 12.0 ± 1.2 events.

Another background from μ^+ DAR in the beam stop is $\nu_e C$ scattering. For $\nu_e ^{12}\text{C} \rightarrow e^- X$ scattering (including the transition to the ^{12}N ground state) an average cross section of $1.5 \times 10^{-41} \text{ cm}^2$ [20] is used. For an electron reconstruction efficiency of 0.36, the fraction of

events with $E > 36$ MeV of 0.014 (as determined by the Monte Carlo simulation and which dominates the systematic error), and the number of ^{12}C atoms in the fiducial volume of 3.7×10^{30} , a total of 20.1 ± 4.0 events is obtained. As shown in Fig. 16, this is the dominant background for $E_e < 36$ MeV. For $\nu_e \text{ } ^{13}\text{C} \rightarrow e^- X$ scattering, an average cross section [21] of $5.3 \times 10^{-41} \text{ cm}^2$ is used, an electron reconstruction efficiency of 0.37 , the fraction of events with $E > 36$ MeV of 0.39 , and the number of ^{13}C nuclei in the fiducial volume of 4.1×10^{28} (1.1% of the carbon nuclei are ^{13}C) to obtain a total of 22.5 ± 4.5 events. Note that the highest energy electron that can be produced with a recoil neutron from ^{13}C is 30 MeV.

Finally, there is a background from $\pi^+ \rightarrow e^+ \nu_e$ DAR in the beam stop followed by $\nu_e C \rightarrow e^- X$ scattering. An average cross section of $2.9 \times 10^{-40} \text{ cm}^2$ [20] is used with an electron reconstruction efficiency of 0.39 , a branching ratio of 1.2×10^{-4} , and a number of ^{12}C atoms in the fiducial volume of 3.7×10^{30} to obtain a total of 3.6 ± 0.7 events.

5.3 Total Beam-Related Background and Maximal Oscillation Signal

Summing all of the above backgrounds, a total beam-related background of 76.2 ± 9.7 events is obtained in the $36 < E_e < 60$ MeV energy range with no γ requirement ($R \geq 0$). Using efficiencies for correlated and accidental γ s with $R > 30$ (0.23 and 0.006 , respectively), the total beam-related background for $R > 30$ is 2.1 ± 0.4 events in the $36 < E_e < 60$ MeV energy range. The total beam-related background is shown as a function of energy in Fig. 16 for (a) $R \geq 0$ and (b) $R > 30$.

Table II also gives the number of events expected for $100\% \bar{\nu}_\mu \rightarrow \bar{\nu}_e$ transmutation, where the total due to $\bar{\nu}_e p \rightarrow e^+ n$ is 12500 ± 1250 events for $R \geq 0$, including a systematic error of 10% . This number is the product of neutrino flux ($7.8 \times 10^{-10} \nu/\text{cm}^2/\text{p}$), number of protons on target (9.2×10^{22}), the average cross section [13] over the entire energy range ($0.95 \times 10^{-40} \text{ cm}^2$), the average positron reconstruction efficiency (0.37), the fraction of events with $E > 36$ MeV (0.67), and the number of free protons in the fiducial volume (7.4×10^{30}). The number implied for $R > 30$ is then 2875 ± 345 events, where a 12% systematic error is used (see

section 7.1). Table III gives the expected number of events for the $20 < E_e < 60$ MeV energy range.

6. DATA SIGNAL

6.1 Event Excess

Table IV lists the number of signal, beam-off background and neutrino-background events for the various selections described in chapter 4. Excess/Efficiency is the excess number of events divided by the total efficiency. Also shown in the table are the probabilities that the event excesses are entirely due to statistical fluctuations. With selection criterion VI and no correlated γ requirement, 139.5 ± 17.7 beam-excess events are observed in the $36 < E_e < 60$ MeV energy range, which is more than the 76.2 ± 9.7 events expected from conventional processes and which results in a total excess of 63.3 ± 20.1 events. To determine whether a γ is a 2.2-MeV γ correlated with an electron or from an accidental coincidence, the approximate likelihood ratio, R , is employed, as described in chapter 3. As listed in Table IV, 22 events beam-on and $36 \times 0.07 = 2.5$ events beam-off, corresponding to a beam on-off excess of 19.5 ± 4.7 events, are observed for $R > 30$, a region in which backgrounds with an accidental γ are greatly suppressed. When each of the electron selection criteria is relaxed, the background increases slightly, but the beam-on minus beam-off event excess does not change significantly. The total estimated neutrino background for $R > 30$ is 2.1 ± 0.4 events, which results in a net excess, beam-on minus total background, of 17.4 ± 4.7 events in the $36 < E_e < 60$ MeV energy range. The probability that this excess is due entirely to a statistical fluctuation of a 4.6 ± 0.6 event expected total background is 4.1×10^{-8} . The corresponding excess for the cuts used in reference [2] (selection I) is 8.7 ± 3.6 events. Table IV lists the results for this and all other selections described in chapter 4. The Excess/Efficiency numbers are all statistically consistent.

6.2 Alternative Geometric Criteria

Two alternative geometric criteria discussed in reference [2] were also studied to minimize cosmic-ray background, although it is reliably measured from beam-off data. The first criterion, defined as selection VIa, removes 6% of the acceptance by requiring $Y > -120$ cm for events with $Z < 0$ cm. The second criterion, defined as selection VIb, removes 55% of the acceptance by requiring $Y > -50$ cm, $Z > -250$ cm, and $D > 50$ cm. The relative acceptances were determined with the sample of $\nu_e C \rightarrow e^- X$ scattering events. As shown in Table IV, the resulting Excess/Efficiency numbers are consistent with the other selections.

6.3 Distributions of Data

Table V lists the 26 beam-on events from selection IV with $R > 30$ and energy in the range $36 < E_e < 60$ MeV. For each event the energy, position, and distance from the PMT surfaces are given. Also given are the selections that each event satisfies. Fig. 17 shows the beam-on minus beam-off energy distributions over an extended energy range, for both $R \geq 0$ (the full positron sample) and $R > 30$ samples that satisfy selection VI. The dashed histograms show the total estimated beam-related backgrounds. In order to illustrate compatibility of the energy distribution with one example of an oscillation hypothesis, a contribution from high- Δm^2 ($\Delta m^2 \rightarrow \infty$) oscillations has been added to the backgrounds, resulting in the solid histograms in the two plots. The shape of this contribution is of course sensitive to Δm^2 . Fig. 18 shows the X, Y, Z spatial distributions for the $R \geq 0$ and $R > 30$ samples, while Figs. 19 and 20 are two-dimensional plots showing the distribution of events in the Y - X and Y - Z planes for (a,b) the beam-on events and (c,d) the beam-off events.

Figures 21 to 27 show a variety of other beam-on minus beam-off distributions for the $R > 30$ selection VI sample, all restricted to $36 < E_e < 60$ MeV. For the $\cos\theta_b$ distribution shown in Fig. 21, where θ_b is the angle between the neutrino direction and the reconstructed positron direction, the solid histogram also illustrates expectations from a high- Δm^2 oscil-

lation hypothesis. The observed average value of $\cos\theta_b$ is 0.20 ± 0.13 , in agreement with the expected value of 0.16 for $\bar{\nu}_e p$ interactions. Electrons from muon decay and $\nu_e C$ scattering have expected values of 0 and < 0 , respectively. For the remaining plots, the expected distributions are those for any neutrino-induced reactions. These distributions are obtained from samples of $\nu_e C \rightarrow e^- X$ scattering events in the $20 < E_e < 36$ MeV energy range and electrons from muon decay with the same selection as for the oscillation sample. Fig. 22 displays the distance from the PMT surfaces, D . The χ , Δt_p , and veto shield multiplicity distributions are shown in Fig. 23, Fig. 24 and Fig. 25, where the χ variables are the particle ID parameters discussed in chapter 4, Δt_p is the time to the previous event, and the veto shield multiplicity is the number of hit veto PMTs in time with the event. Finally, the $\vec{r} \cdot \hat{d}\vec{r}$ and the S distributions, discussed in chapter 4, are shown in Fig. 26 and Fig. 27.

6.4 Tests of Spatial, Energy, and Time Distributions

6.4.1 Spatial Distribution of Beam-Related Data

Cosmic-ray background is larger in the outer regions of the detector and where the veto has gaps – beneath the detector (large negative Y), and around the periphery of the upstream end at large negative Z. Because the beam-on data includes cosmic-ray background, it is expected to show concentrations in the same regions of the detector. In fact, any effect from strong or electromagnetic interactions coming from outside the detector should be concentrated near the detector boundary.

The source of neutrinos is concentrated in the region of the beam stop described in reference [1]. The distance from the beam stop to the center of the detector is 29.8 m, and the angular distribution of the neutrinos is isotropic. The neutrino flux from targets A1 and A2, which are 105 m and 130 m away, respectively, imposes a small variation on the flux distribution calculated using the A6 location. Neutrino event distributions in the detector are expected to reflect the varying solid angle of the detector with small effects

from the finite extent of the source. This is simulated in detail, although the deviation from uniformity is small, and these fluxes are used in estimating rates.

It is important to test whether the spatial distributions of beam excess events are compatible with neutrino oscillations. To this end, a Kolmogorov statistic is computed for each distribution being tested for consistency. For a given variable V , an observed cumulative probability distribution, F_{on} , is computed for beam-on data. If N_{on} is the number of beam-on events, then $N_{on}F_{on}(w)$ is the number of beam-on events with V less than w . F_{on} is a step function. If the distribution in V is consistent with beam-off background plus a contribution from neutrino interactions, then F_{on} should be approximately equal to an expected cumulative probability distribution, F , that is a combination of these two contributions. The Kolmogorov statistic, K , is the maximum distance between F_{on} and F . The probability distribution of K is computed for the case of the beam-on excess coming from neutrino interactions.

One contribution to $N_{on}F(w)$ is the expected number of events from the cosmic background. If there are N_{off} beam-off events, and r is the ratio between beam-on and beam-off time, then the expected total number from cosmic background is rN_{off} . If the step function, F_{off} , is defined the same as F_{on} , except for beam-off events instead of beam-on ones, then the expected contribution to $N_{on}F(w)$ from cosmic background is equal to $rN_{off}F_{off}(w)$. The remaining contribution to $N_{on}F(w)$ is from the $N_{on} - rN_{off}$ excess of presumably neutrino events, which should be distributed according to a smooth cumulative probability distribution, F_ν . For each variable, V , we take $F_\nu(w)$ to be the expected fraction of neutrino interactions in our acceptance with V below w . It is computed with a Monte Carlo program that includes the position dependent neutrino flux and position dependent positron detection efficiency, and of course includes the requirement that positrons be reconstructed at least 35 cm from the photomultiplier tube faces. Then $(N_{on} - rN_{off})F_\nu(w)$ is the expected contribution to $N_{on}F(w)$ from the beam-on excess if that excess is from neutrino

interactions. Thus

$$F(w) = \frac{rN_{off}}{N_{on}}F_{off}(w) + \left(1 - \frac{rN_{off}}{N_{on}}\right)F_{\nu}(w).$$

The Kolmogorov statistic, K , is easily determined, given the functions, F_{on} and F . Each computation of K involves comparing a cumulative distribution of data (F_{on}) with a function that is a linear combination of a distribution of other data (F_{off}) and a smooth theoretical function (F_{ν}). The probability distribution of K is not given in standard tables for such a case. We therefore perform a Monte Carlo computation of the probability of K accidentally being at least as large as is measured.

One complication is that the Z distribution for neutrino oscillation events depends on the value of Δm^2 . In the limit of large Δm^2 , however, the distribution has the same L^{-2} dependence as for other neutrino interactions, where L is the distance from the neutrino production point to the neutrino interaction location. The consistency checks are calculated for this case. If K is measured to be especially high, i.e., if there is an especially low probability of K accidentally being higher, then the observed distribution is inconsistent with the assumption that the beam-on excess comes from neutrino interactions in the detector tank. The consistency checks on the spatial distribution of the data amount to finding such probabilities for each of several distributions, including those shown in Figs. 18 and 22. A high probability near one means that the distribution is very similar to the expected distribution, while a probability near zero means that the distribution is not very similar. Results are presented in Table VI with various cuts for identification of the γ from $np \rightarrow d\gamma$.

If the gap in the veto beneath the detector is responsible for the beam-on excess, the Y distribution would be expected to show an especially low probability. If the holes in the veto at its upstream end are responsible for the excess, the Z distribution or the distribution in distance from the bottom upstream corner with low Y, Z would show a low probability. If the events are anomalously concentrated towards the outer part of the detector, then there would be a low probability for the variable that measured the distance from the PMT faces. These probabilities are computed for various cuts on R , the photon discrimination

parameter. The probabilities for $R \geq 0$ are observed to be smaller than the probabilities for $R > 1.5$ or $R > 30$. This is due to the high statistics of the $R \geq 0$ sample, which makes this sample very sensitive to uncertainties in the expected position distribution. For example, the Z distribution and low YZ distribution probabilities for $R \geq 0$ increase from 0.047 to 0.331 and from 0.016 to 0.074, respectively, when one assumes that the events are uniformly distributed in the detector instead of having a L^{-2} position dependence. Although this assumption is unrealistic for the large expected beam-associated neutrino background with $R \geq 0$ (see Table IV), a contribution from neutrino oscillations at low Δm^2 would have a uniform position dependence.

6.4.2 Kolmogorov Test on the Energy Distribution

The energy distribution of events with $R > 30$ has been subjected to the same Kolmogorov test as in the previous section on the geometric distribution of events. Events near and above 60 MeV provide incentive for this test. The cumulative distribution for neutrinos, $F_\nu(E)$, is taken to be the expected energy distribution for neutrino oscillations in the limit of high Δm^2 . The contribution shown in Fig. 17 from known neutrino interactions is ignored, as well as possible contributions from DIF oscillation events. The probability that the energy distribution for $R > 30$ is consistent with this hypothetical distribution is 35% for $36 < E_e < 60$ MeV and 37% for $36 < E_e < 80$ MeV. There is no evidence of an excess of events above 60 MeV. For the $60 < E_e < 80$ MeV interval there are 4 events beam on and 62 events beam off, corresponding to an excess of -0.3 ± 2.1 events. The solid curve in Fig. 17b shows that there is no incompatibility between the oscillation hypothesis and the data excess, given present statistical errors.

6.4.3 Time Distribution of Beam-Related Data

Another consistency check on our data and analysis methods is whether the evidence for neutrino oscillations is reasonably uniform from one year of data collection to the next. Small

problems with the apparatus, corrected as the experiment progressed, can make spurious signals appear only in data collected before hardware repairs. Unconscious prejudices can lead experimenters to tune cuts until a selection is found that accidentally gives a spurious signal. Such a selection would not show a signal for data collected after the cuts have been tuned.

In order to test for time variation of our data, we bin beam-on and beam-off data for $R > 30$ by the year in which it is collected. Most changes in apparatus and procedures are made in the periods between the running periods of different years. We consider two selections for the data: Selection I, which is the same as was used before beginning the 1995 runs and on which a previous publication [2] is based; and Selection VI, which includes the the most recent analysis improvements. The excesses (beam-on minus duty ratio times beam-off) should be roughly proportional to the $\bar{\nu}_\mu$ fractions of integrated beam intensity during each time period. The consistency checks test how probable are the observed deviations from rough proportionality.

Table VII shows the results of two types of consistency checks. “Prob 1” is the probability of beam-on data accidentally being distributed in an equally likely or less likely way than is observed, given the beam-off numbers of events in each year and the duty ratios. “Prob 2” is the probability of the 1995 beam-on number accidentally being as low as is observed given the beam-off numbers in each year, the total beam-on number of events, and the duty ratios. No probability is so low as to demonstrate a serious inconsistency.

7. FITS TO THE DATA

7.1 Fits to Determine the Oscillation Probability

For the observed excess, the overall oscillation probability is found by fitting the R distribution to determine the fraction of events with a correlated γ . The overall oscillation probability is the number of excess correlated events divided by the total number of events

expected for 100% $\bar{\nu}_\mu \rightarrow \bar{\nu}_e$ transmutation. Note that for any experiment the oscillation probability is dependent on the experiment's geometry and energy range in addition to $\sin^2 2\theta$ and Δm^2 . The one-parameter χ^2 fit to the R distribution takes into account the position dependence of the γ rates by using the actual beam-on and beam-off events that satisfy the oscillation criteria. The accidental γ spatial distributions are determined from laser calibration events. Fig. 28 shows the R distribution, beam-on minus beam-off excess, for events that satisfy selection VI (see chapter 4) and that have energies in the range $20 < E_e < 60$ MeV. There are 1763 beam-on events and 11981 beam-off events in this energy range, corresponding to a beam on-off excess of 924.3 events.

The R distribution is fit to the two different R shapes discussed in chapter 3 and illustrated in Fig. 5. The fit using the R shape from cosmic ray neutrons has a $\chi^2 = 6.9/9$ D.O.F. and determines that $68.5^{+19.4}_{-17.6}$ events have a γ that is correlated with the primary, while the fit using the Monte Carlo R shape has a $\chi^2 = 5.4/9$ D.O.F. and determines that $60.1^{+17.6}_{-15.7}$ events have a γ that is correlated with the primary. Averaging these numbers and subtracting the neutrino background with a correlated γ (12.5 ± 2.9 events) results in a net excess of $51.8^{+18.7}_{-16.9}$ events. (If the number of events with a correlated γ is set to the background estimate of 12.5 events, the χ^2 increases by 15.0 and 14.1, respectively, compared to the above two fits.) This corresponds to an oscillation probability of $(0.31^{+0.11}_{-0.10} \pm 0.05)\%$, where the first error is statistical and the second error is the systematic error arising from uncertainties in the neutrino flux (7%), e^+ efficiency (7%), and γ efficiency (7%). The latter two uncertainties are lower than in our previous publication [2] due to improved understanding of the detector performance. Note that the statistical error is non-Gaussian and corresponds to an increase of the χ^2 by one over the minimum χ^2 fit. The systematic error is for both the background estimate and the expected number of oscillation events. Also, $860.8^{+18.5}_{-16.7}$ events do not have a correlated γ , which agrees with the estimated neutrino background of 795.0 ± 133.9 events from Table VIII. The solid curve in Fig. 28 is the best fit to the data, while the dashed curve is the component of the fit with an uncorrelated γ . Table VIII summarizes the results of the χ^2 fit. Also shown in Table VIII is the result of a likelihood fit

that uses for each positron event the local accidental R distribution rather than a weighted average, and the number of signal and background events in the $20 < E_e < 60$ MeV energy range with $R > 30$.

7.2 Favored Regions of Δm^2 vs. $\sin^2 2\theta$

Assuming that the observed event excess is due to neutrino oscillations, a likelihood fit is performed to determine favored regions in the Δm^2 vs. $\sin^2 2\theta$ plane, where Δm^2 is the difference of the squares of the approximate mass eigenstates and θ is the mixing angle. A general formalism for neutrino oscillations would involve all three generations and the possibility of CP violation. In fact, any pair of neutrinos ($\bar{\nu}_e$, $\bar{\nu}_\mu$, $\bar{\nu}_\tau$, or more properly ν_1 , ν_2 , or ν_3) with a Δm^2 in the region of experimental sensitivity could lead to a signal in a $\bar{\nu}_\mu \rightarrow \bar{\nu}_e$ oscillation search. However, here the formalism is simplified by assuming that only two generation mixing is important. Then the oscillation probability can be written

$$P = \sin^2(2\theta) \sin^2 \left(1.27 \Delta m^2 L / E_\nu \right) \quad ,$$

where L is the distance from neutrino production to detection in meters and E_ν is the neutrino energy in MeV. The discussion is limited to this restricted formalism solely as a basis for experimental parameterization, and no judgement is made as to the simplicity of the actual situation.

Four measured quantities are used to separate oscillation candidates from background and determine the parameters of the oscillation. These are E_e (the measured energy of the positron), R (the gamma likelihood ratio), $\cos \theta_b$ (the cosine of the angle between the e and ν directions), and L (the measured distance from the $\bar{\nu}_\mu$ source). The 1763 beam-on events passing selection VI are binned in four dimensions according to these measured quantities. Using the background estimates from chapter 5, the distributions of beam-related background events in these variables are calculated. To calculate the beam-unrelated background, the measured beam-off data set is smoothed and scaled by the duty ratio.

A likelihood function, \mathcal{L} , is constructed:

$$\mathcal{L}(n_1, n_2, \dots | \Delta m^2, \sin^2 2\theta) = \prod_{i=1}^N \frac{1}{n_i!} \nu_i^{n_i} e^{-\nu_i},$$

where N is the total number of bins, n_i is the number of beam-on events in bin i , and ν_i is the expected number in bin i . The expected number in bin i may be written

$$\nu_i = \nu_{i,\text{BUB}} + \nu_{i,\text{BRB}} + \nu_{i,\text{osc}}(\Delta m^2, \sin^2 2\theta),$$

where $\nu_{i,\text{BUB}}$ is the calculated number of events in bin i due to beam-unrelated background, $\nu_{i,\text{BRB}}$ is that due to beam-related background, and $\nu_{i,\text{osc}}(\Delta m^2, \sin^2 2\theta)$ is the expected number of events for a particular pair of $\Delta m^2, \sin^2 2\theta$ values. This likelihood function reaches its maxima at $15 \text{ and } 19 \text{ eV}^2, \sin^2 2\theta = 0.006$. The individual distributions of E_e , R , $\cos \theta_b$, and L for the data are compared with projections of the expected four-dimensional distribution (including oscillations at $19 \text{ eV}^2, \sin^2 2\theta = 0.006$) in Fig. 29. Note that most of the data in Fig. 29 is from beam-unrelated or neutrino-induced background.

The log of this likelihood function is calculated for a range of $\Delta m^2, \sin^2 2\theta$ values. Regions within 2.3 and 4.5 log-likelihood units of vertical distance from the peak are identified. These regions are called “90%” and “99%” likelihood regions. (They do not define confidence limits, but do show the regions favored by the experiment.) These favored regions are calculated several times while varying inputs to reflect systematic uncertainties. The systematic effects varied included: the method used for smoothing the beam-off data, the method used for calculation of the correlated R distribution, and the normalization of the backgrounds (both beam-related and beam-unrelated are shifted by $\pm 1\sigma$). Also, the product of neutrino flux and detection efficiency was allowed to change by $\pm 10\%$. Regions which are favored in any of these systematic investigations are shown in Fig. 30, where the darkly-shaded and lightly-shaded regions correspond to 90% and 99% likelihood regions, respectively. This figure shows discrimination against some values of Δm^2 which would be allowed in an analysis that simply took the size of the oscillation signal into account. This discrimination may be understood from the energy plot of Fig. 17b. The presence of relatively high-energy

oscillation candidates tends to exclude Δm^2 near integral multiples of $4.3eV^2$. (These values of Δm^2 give $\sin^2(1.27\Delta m^2 L/E_\nu)$ near 0 for the highest energy $\bar{\nu}_\mu$.)

Some of the favored region is excluded by the ongoing KARMEN experiment [22] at ISIS, E776 at BNL [23], and the Bugey reactor experiment [24] (see section 8.2). However, there remains a region at small values of Δm^2 and $\sin^2 2\theta$ where our oscillation parameters are not in conflict with any other experiment.

It is difficult to place additional constraints on Δm^2 with the few events collected to date. Fig. 31 shows the L/E_ν distribution of the high- R data (from the top 3 R bins of Fig. 29) compared with expectations for several pairs of $\Delta m^2, \sin^2 2\theta$. (E_ν is calculated from the measured values E_e and $\cos \theta_b$.) This plot gives an indication of the statistical precision needed to distinguish between high and low values of Δm^2 . It also shows the expected L/E_ν distribution for the disfavored $4.3eV^2$.

7.3 Neutrino Backgrounds with a Correlated γ

In this section we discuss in more detail the two major neutrino backgrounds with a correlated γ : (1) μ^- DAR in the beam stop followed by the reaction $\bar{\nu}_e p \rightarrow e^+ n$ in the detector; and (2) π^- DIF in the beam stop followed by the reaction $\bar{\nu}_\mu p \rightarrow \mu^+ n$ in the detector. As described in section 5.1, these backgrounds are each estimated to be about an order of magnitude smaller than the observed excess. Additional arguments, however, can be made to demonstrate that these backgrounds are not likely to explain the signal.

7.3.1 μ^- DAR Background

Because the $\bar{\nu}_e$ spectrum from μ^- decay is softer than the $\bar{\nu}_\mu$ spectrum from μ^+ decay, one can, in principle, distinguish between $\bar{\nu}_\mu \rightarrow \bar{\nu}_e$ oscillations and μ^- DAR background by fitting the energy distribution. This is accomplished by allowing the μ^- background to float and determining how good a fit (see section 7.2) can be obtained without neutrino oscillations. The best such fit has a μ^- DAR background contribution that is 8 times larger

than the estimated background of 8.6 ± 1.7 events (see Table VIII). However, even with such an increase, this best fit has the log of the likelihood function 2.2 units less than the best oscillation fit. Therefore, our observed excess is less compatible with the shape of the μ^- DAR background.

7.3.2 π^- DIF Background

As mentioned in chapter 2, the nominal trigger threshold for past activity in LSND is 18 hit PMTs. This allows a background to arise from π^- DIF in the beam stop followed by $\bar{\nu}_\mu p \rightarrow \mu^+ n$ scattering, where the μ^+ is below the 18 PMT threshold. (Background contributions also arise from $\bar{\nu}_\mu C \rightarrow \mu^+ nX$ and $\nu_\mu C \rightarrow \mu^- nX$ scattering.) We are confident of our calculation of this background in chapter 5. However, to ensure that such events do not explain our observed signal, the trigger was modified for the 1995 running so that all hit PMTs within $0 - 3$ and $3 - 6$ μ s of selected events are recorded as two extra events. Fig. 32 shows the total number of hit PMTs in the detector tank for those extra events that occur $0 - 3\mu$ s and $3 - 6\mu$ s prior to oscillation candidate events. The candidates are in the $25 < E_e < 60$ MeV energy range with (a) $R \geq 0$ and (b) $R > 30$. The data points are the beam on events, while the solid curve is what is expected from random PMT hits as determined from the sample of laser calibration events. There is good agreement between the data and the laser events and little evidence of candidates from π^- DIF background, which the Monte Carlo simulation estimates would hit an additional 10 PMTs on average. This also confirms that the trigger operated correctly.

The sample of $\nu_\mu C \rightarrow \mu^- X$ scattering events also has been studied to check that the observed hit PMT distribution from the recoil μ and X agrees with our Monte Carlo simulation. This sample is cleanly obtained by requiring a coincidence between the μ and the decay electron and by performing a beam-on minus-off subtraction. Fig. 33 shows the observed hit PMT distribution for all $\nu_\mu C$ scattering events (including $\nu_\mu C \rightarrow \mu^- X$, $\bar{\nu}_\mu C \rightarrow \mu^+ X$, and $\bar{\nu}_\mu p \rightarrow \mu^+ n$) for events with (a) $R \geq 0$ and (b) $R > 30$. The solid histogram in each case

is the prediction from the Monte Carlo simulation, normalized to the data. The agreement is excellent and serves as a check of our background estimate from chapter 5.

8. INTERPRETATION OF RESULTS

8.1 Possible Explanations

This paper reports an excess of events that is consistent with the reaction $\bar{\nu}_e p \rightarrow e^+ n$ and is an order of magnitude larger than what is expected from conventional physics processes. This excess is, therefore, evidence for $\bar{\nu}_\mu \rightarrow \bar{\nu}_e$ oscillations within the allowed range of Fig. 30. Note that for three neutrino flavors there must be three-generation mixing, so that the oscillation probability is in general a sum of three terms, where each term has an oscillation wavelength determined by one of the three different Δm^2 values. However, there are other exotic physics explanations of the observed excess. One example is the lepton-number-violating decay $\mu^+ \rightarrow e^+ \bar{\nu}_e \nu_\mu$, which can explain these observations with a branching ratio of $(0.31^{+0.11}_{-0.10} \pm 0.05)\%$. The published upper limit on this “wrong-sign” muon decay mode is 1.2% [25]; however, a preliminary report from the KARMEN experiment [26] gives a much stricter limit, $\mu^+ \rightarrow e^+ \bar{\nu}_e \nu_\mu / \mu^+ \rightarrow e^+ \nu_e \bar{\nu}_\mu < 0.25\%$ at 90% C.L. If an excess similar to that reported in the present paper is observed also in the π^+ DIF $\nu_\mu \rightarrow \nu_e$ search from LSND or from some other experiment, then the oscillation hypothesis will be favored and the allowed region in Fig. 30 will be constrained.

8.2 Review of Other Experiments

In this section the evidence restricting neutrino oscillation parameters is briefly reviewed. Three experiments using the BNL wide-band beam have searched for $\nu_\mu \rightarrow \nu_e$ oscillations. They are an experiment primarily designed to measure neutrino electron scattering, E734 [27], a follow up on a previous indication of neutrino oscillations at the CERN PS, E816 [28], and a specifically designed long baseline oscillation experiment, E776 [23].

The BNL neutrino beam is a horn focused beam composed mainly of ν_μ and $\bar{\nu}_\mu$ from pion and kaon DIF. The principal ν_e background for all of the experiments comes from the pion-muon decay sequence and from charged and neutral kaon decay. Integrated over the entire spectrum, this ν_e flux is about 1% of the ν_μ flux with a minimum ν_e flux of about 0.6% near a neutrino energy of 1 GeV. Each experiment also has a photon background from π^0 production, where one γ is confused as an electron and where the second γ is not seen. The first two experiments separate photons by observing the primary vertex and using the spatial separation of the photon from this primary vertex to distinguish electrons and photons. The third experiment relies on a Monte Carlo method to calculate the background from π^0 production. In each case, the systematic errors dominate the limits reported by E734 and E776, as shown in Figs. 30 and 34a.

The difference in limits in Fig. 34a is almost completely accounted for by the different distances from the target (E734 is at 120 m and E776 at 1000 m from the neutrino source) because the beam is common to both measurements. The E816 experiment observed an excess of electron events 1.6 ± 0.9 times that expected. The average E816 neutrino energy was about 1.2 GeV, although individual electron event energies were not reported. The CCFR experiment [30] provides the most stringent limit on $\nu_\mu \rightarrow \nu_e$ oscillations near $\Delta m^2 \sim 350 \text{eV}^2$, but their limits are not as restrictive as E776 for values of $\Delta m^2 < 300 \text{eV}^2$.

The KARMEN experiment [22] has searched for $\nu_\mu \rightarrow \nu_e$ oscillations using neutrinos from pion DAR. These neutrinos are monoenergetic, and the signature for oscillations is an electron energy peak at about 12 MeV. This method has very different backgrounds and systematics compared to the previous three experiments but, unfortunately, does not yet have statistical precision sufficient to affect the exclusion region of Fig. 34b. The KARMEN experiment also has searched for $\bar{\nu}_\mu \rightarrow \bar{\nu}_e$ oscillations and has produced the exclusion plot shown in Figs. 30 and 34b. KARMEN is located 18m from the neutrino source, compared with 30 m for LSND. The experiments have sensitivities, therefore, that peak at different values of Δm^2 . Experiments E225 and E645 at LAMPF also searched for $\bar{\nu}_\mu \rightarrow \bar{\nu}_e$ oscillations and set less restrictive limits [29], [25].

The most recent experiments searching for $\bar{\nu}_e$ disappearance are Gosgen [31], Bugey [24], and Krasnoyarsk [32]. Power reactors are prolific sources of $\bar{\nu}_e$, and the detection method is similar in the three cases. The Bugey measurement has the highest reported sensitivity. The detectors observe both the positron from the primary neutrino interaction and the capture energy (4.8 MeV) from neutron absorption on ${}^6\text{Li}$. This capture time is about 50 μs and, after saturation effects in the scintillator are included, the capture energy yields 0.5 MeV electron equivalent energy. The positron energy is 1.8 MeV below the neutrino energy and allows an event-by-event measure of neutrino energy. Detectors are placed at 15m, 40m, and 95 m from the nearest reactor. Two methods are used to search for oscillations. The first uses the ratio of events seen in the three detectors and the second uses an absolute prediction of flux from the reactor as a further constraint. The resulting limit is shown in Figs. 30 and 34c.

Searches for ν_μ disappearance have been conducted at both CERN and Fermilab by the CDHS [33] and CCFR [30] experiments. In each case two detectors are placed at different distances from the neutrino source, which is a DIF ν_μ beam without focusing. The limits obtained by these experiments are shown in Fig. 34d. Also shown in this figure are limits derived from the E531 Fermilab experiment [34] which searches for the appearance of tau decay from charged current interactions in a high energy neutrino beam. Experiments which probe ν_e disappearance and ν_μ disappearance have given limits which are not sensitive enough to constrain the results here, except at the lowest Δm^2 .

9. CONCLUSIONS

The LSND experiment observed 22 electron events in the $36 < E_e < 60$ MeV energy range that were correlated in time and space with a low-energy γ , and the total estimated background from conventional processes is 4.6 ± 0.6 events. The probability that this excess is due to a statistical fluctuation is 4.1×10^{-8} . The observed excess is consistent with $\bar{\nu}_\mu \rightarrow \bar{\nu}_e$ oscillations, and a fit to the entire electron sample with electron energy in the range

$20 < E_e < 60$ MeV results in an oscillation probability of $(0.31_{-0.10}^{+0.11} \pm 0.05)\%$. The allowed regions of $\sin^2 2\theta$ vs. Δm^2 are shown in Fig. 30.

Acknowledgements The authors gratefully acknowledge the support of Peter Barnes, Cyrus Hoffman, and John McClelland. It is particularly pleasing that a number of undergraduate students from participating institutions were able to contribute to the experiment. We acknowledge many interesting and helpful discussions with Dharam Ahluwalia, Terry Goldman, Peter Herczeg, Petr Vogel, and Geoffrey West. This work was conducted under the auspices of the US Department of Energy, supported in part by funds provided by the University of California for the conduct of discretionary research by Los Alamos National Laboratory. This work is also supported by the National Science Foundation. We are particularly grateful for the extra effort that was made by these organizations to provide funds for running the accelerator at the end of the data taking period in 1995.

TABLES

TABLE I. The positron selection criteria and corresponding efficiencies for selections I and VI.

The variables are defined in the text.

Selection I	Efficiency	Selection VI	Efficiency
PID	0.77 ± 0.02	PID	0.84 ± 0.02
< 2 Veto Hits	0.84 ± 0.02	< 4 Veto Hits	0.98 ± 0.01
$\Delta t_p > 40\mu s$	0.50 ± 0.02	$\Delta t_p > 20\mu s, 34\mu s$	0.68 ± 0.02
DAQ Deadtime	0.97 ± 0.01	DAQ Deadtime	0.97 ± 0.01
35 cm Fiducial Volume	0.85 ± 0.05	35 cm Fiducial Volume	0.85 ± 0.05
No event within $8\mu s$	0.99 ± 0.01	No event within $8\mu s$	0.99 ± 0.01
< 3 Associated γ s	0.99 ± 0.01	< 2 Associated γ s	0.94 ± 0.01
–	1.00	$S > 0.5$	0.87 ± 0.02
Total	0.26 ± 0.02	Total	0.37 ± 0.03

TABLE II. A list of all backgrounds with the expected number of background events in the $36 < E_e < 60$ MeV energy range that satisfy selection VI for $R \geq 0$ (the full positron sample) and $R > 30$. The neutrinos are from either π and μ decay at rest (DAR) or decay in flight (DIF). Also shown are the number of events expected for 100% $\bar{\nu}_\mu \rightarrow \bar{\nu}_e$ transmutation.

Background	Neutrino Source	Events with $R \geq 0$	Events with $R > 30$
Beam Off		160.5 ± 3.4	2.52 ± 0.42
Beam-Related Neutrons		< 0.7	< 0.1
$\bar{\nu}_e p \rightarrow e^+ n$	$\mu^- \rightarrow e^- \bar{\nu}_\mu \bar{\nu}_e$ DAR	4.8 ± 1.0	1.10 ± 0.22
$\bar{\nu}_\mu p \rightarrow \mu^+ n$	$\pi^- \rightarrow \mu^- \bar{\nu}_\mu$ DIF	2.7 ± 1.3	0.62 ± 0.31
$\bar{\nu}_e p \rightarrow e^+ n$	$\pi \rightarrow e \nu$ and $\mu \rightarrow e \nu \bar{\nu}$ DIF	0.1 ± 0.1	0
Total with Neutrons		7.6 ± 1.8	1.72 ± 0.41
$\nu_\mu C \rightarrow \mu^- X$	$\pi^+ \rightarrow \mu^+ \nu_\mu$ DIF	8.1 ± 4.0	0.05 ± 0.02
$\nu_e {}^{12}C \rightarrow e^- {}^{12}N$	$\mu^+ \rightarrow e^+ \bar{\nu}_\mu \nu_e$ DAR	20.1 ± 4.0	0.12 ± 0.02
$\nu_e {}^{13}C \rightarrow e^- {}^{13}N$	$\mu^+ \rightarrow e^+ \bar{\nu}_\mu \nu_e$ DAR	22.5 ± 4.5	0.14 ± 0.03
$\nu e \rightarrow \nu e$	$\mu^+ \rightarrow e^+ \bar{\nu}_\mu \nu_e$ DAR	12.0 ± 1.2	0.07 ± 0.01
$\nu e \rightarrow \nu e$	$\pi \rightarrow \mu \nu_\mu$ DIF	1.5 ± 0.3	0.01 ± 0.01
$\nu_e C \rightarrow e^- X$	$\pi \rightarrow e \nu_e$ DAR	3.6 ± 0.7	0.02 ± 0.01
$\nu_\mu C \rightarrow \pi X$	$\pi \rightarrow \mu \nu_\mu$ DIF	0.2 ± 0.1	0
$\nu_e C \rightarrow e^- X$	$\pi \rightarrow e \nu$ and $\mu \rightarrow e \nu \bar{\nu}$ DIF	0.6 ± 0.1	0
Total without Neutrons		68.6 ± 9.5	0.41 ± 0.06
Grand Total		236.7 ± 10.2	4.65 ± 0.59
100% Transmutation	$\mu^+ \rightarrow e^+ \bar{\nu}_\mu \nu_e$ DAR	12500 ± 1250	2875 ± 345

TABLE III. A list of all backgrounds with the expected number of background events in the $20 < E_e < 60$ MeV energy range that satisfy selection VI for $R \geq 0$ (the full positron sample) and $R > 30$. The neutrinos are from either π and μ decay at rest (DAR) or decay in flight (DIF). Also shown are the number of events expected for 100% $\bar{\nu}_\mu \rightarrow \bar{\nu}_e$ transmutation.

Background	Neutrino Source	Events with $R \geq 0$	Events with $R > 30$
Beam Off		782.0 ± 7.4	9.2 ± 0.8
Beam-Related Neutrons		< 3.8	< 0.5
$\bar{\nu}_e p \rightarrow e^+ n$	$\mu^- \rightarrow e^- \nu_\mu \bar{\nu}_e$ DAR	8.6 ± 1.7	2.0 ± 0.4
$\bar{\nu}_\mu p \rightarrow \mu^+ n$	$\pi^- \rightarrow \mu^- \bar{\nu}_\mu$ DIF	3.8 ± 1.9	0.9 ± 0.4
$\bar{\nu}_e p \rightarrow e^+ n$	$\pi \rightarrow e \nu$ and $\mu \rightarrow e \nu \bar{\nu}$ DIF	0.1 ± 0.1	0
Total with Neutrons		12.5 ± 2.9	2.9 ± 0.6
$\nu_\mu C \rightarrow \mu^- X$	$\pi^+ \rightarrow \mu^+ \nu_\mu$ DIF	11.3 ± 5.6	0.1 ± 0.1
$\nu_e {}^{12}C \rightarrow e^- {}^{12}N$	$\mu^+ \rightarrow e^+ \bar{\nu}_\mu \nu_e$ DAR	666.7 ± 133.3	4.0 ± 0.8
$\nu_e {}^{13}C \rightarrow e^- {}^{13}N$	$\mu^+ \rightarrow e^+ \bar{\nu}_\mu \nu_e$ DAR	45.6 ± 9.1	0.3 ± 0.1
$\nu e \rightarrow \nu e$	$\pi^+ \rightarrow \mu^+ \nu_\mu, \mu^+ \rightarrow e^+ \bar{\nu}_\mu \nu_e$ DAR	56.7 ± 5.7	0.3 ± 0.1
$\nu e \rightarrow \nu e$	$\pi \rightarrow \mu \nu_\mu$ DIF	8.4 ± 1.7	0.1 ± 0.1
$\nu_e C \rightarrow e^- X$	$\pi \rightarrow e \nu_e$ DAR	5.1 ± 1.0	0
$\nu_\mu C \rightarrow \pi X$	$\pi \rightarrow \mu \nu_\mu$ DIF	0.3 ± 0.1	0
$\nu_e C \rightarrow e^- X$	$\pi \rightarrow e \nu$ and $\mu \rightarrow e \nu \bar{\nu}$ DIF	0.9 ± 0.2	0
Total without Neutrons		795.0 ± 133.9	4.8 ± 0.8
Grand Total		1589.5 ± 134.1	16.9 ± 1.3
100% Transmutation	$\mu^+ \rightarrow e^+ \bar{\nu}_\mu \nu_e$ DAR	16670 ± 1667	3830 ± 460

TABLE IV. The number of signal and background events in the $36 < E_e < 60$ MeV energy range. Excess/Efficiency is the excess number of events divided by the total efficiency. The beam-off background has been scaled to the beam-on time. Also shown in the table is the probability that the observed excess is due entirely to a statistical fluctuation. Results are given for $R \geq 0$ (the full positron sample) and for $R > 30$. The different selection criteria are described in section 4.3. (Note that selections VIa and VIb are restricted-geometry tests described in section 6.2.)

Selection	Signal	Beam Off	ν Bkgd.	Excess	Excess/Efficiency	Fluct. Prob.
I, $R \geq 0$	221	133.6 ± 3.1	53.5 ± 6.8	33.9 ± 16.6	130 ± 64	
I, $R > 30$	13	2.8 ± 0.4	1.5 ± 0.3	8.7 ± 3.6	146 ± 61	1.0×10^{-3}
II, $R \geq 0$	245	156.3 ± 3.3	57.6 ± 7.3	31.1 ± 17.6	111 ± 63	
II, $R > 30$	14	4.1 ± 0.5	1.6 ± 0.3	8.3 ± 3.8	129 ± 58	3.8×10^{-3}
III, $R \geq 0$	285	187.3 ± 3.6	67.9 ± 8.6	29.8 ± 19.3	90 ± 58	
III, $R > 30$	17	5.3 ± 0.6	1.9 ± 0.3	9.8 ± 4.2	129 ± 54	2.1×10^{-3}
IV, $R \geq 0$	407	260.3 ± 4.3	93.2 ± 11.9	53.5 ± 23.8	119 ± 53	
IV, $R > 30$	26	6.5 ± 0.7	2.6 ± 0.5	16.9 ± 5.1	163 ± 51	1.2×10^{-5}
V, $R \geq 0$	401	255.3 ± 4.2	87.6 ± 11.2	58.1 ± 23.3	135 ± 54	
V, $R > 30$	25	4.5 ± 0.6	2.4 ± 0.4	18.1 ± 5.0	183 ± 50	3.8×10^{-7}
VI, $R \geq 0$	300	160.5 ± 3.4	76.2 ± 9.7	63.3 ± 20.1	171 ± 54	
VI, $R > 30$	22	2.5 ± 0.4	2.1 ± 0.4	17.4 ± 4.7	205 ± 54	4.1×10^{-8}
VIa, $R \geq 0$	269	122.0 ± 2.9	71.6 ± 9.1	75.4 ± 19.0	217 ± 55	
VIa, $R > 30$	21	2.0 ± 0.4	2.0 ± 0.4	17.0 ± 4.6	211 ± 57	2.5×10^{-8}
VIb, $R \geq 0$	99	33.5 ± 1.5	34.3 ± 4.4	31.2 ± 11.0	187 ± 66	
VIb, $R > 30$	6	0.8 ± 0.2	0.9 ± 0.2	4.3 ± 2.5	110 ± 63	1.1×10^{-2}

TABLE V. The 26 beam-on events with $R > 30$ and energy in the $36 < E_e < 60$ MeV range that satisfy selection IV. For each event is given the year recorded, energy, spatial position, and distance from the PMT surfaces. Also given are the selections that each event satisfies.

Event	Year	E(MeV)	X(cm)	Y(cm)	Z(cm)	D(cm)	Selections
1	1993	47.6	-66	-84	-77	115	I-VI
2	1993	51.1	56	-96	53	103	I-VI
3	1994	40.1	-36	196	-203	53	I-VI
4	1994	44.2	69	-146	153	53	I-VI
5	1994	39.4	-169	96	-347	39	II-VI
6	1994	36.3	-156	-79	-207	84	I-VI
7	1994	56.8	-221	-24	-309	36	I-V
8	1994	52.9	21	106	71	143	IV-VI
9	1994	37.0	31	156	-105	93	IV-VI
10	1994	42.4	-14	-121	-239	78	IV-VI
11	1994	37.7	-91	119	209	109	I-VI
12	1994	54.3	-91	191	269	47	III-VI
13	1994	55.8	71	-99	-259	100	I-VI
14	1994	43.8	6	211	173	38	I-VI
15	1995	50.5	153	-159	-193	38	IV-V
16	1995	59.9	-132	-164	339	35	III-V
17	1995	49.2	-184	10	58	75	I-VI
18	1995	56.5	128	-150	199	49	I-VI
19	1995	37.4	45	-92	-239	107	IV-VI
20	1995	45.1	-186	105	-126	45	IV-VI
21	1995	46.7	179	-93	-108	57	III-VI
22	1995	40.2	-37	-71	160	128	I-VI
23	1995	47.7	-126	-135	-263	64	IV

24	1995	45.9	-161	87	-337	49	I-VI
25	1995	36.3	46	150	107	100	IV-VI
26	1995	37.6	-73	107	-257	129	IV-VI

TABLE VI. Kolmogorov consistency probability for the distribution of various spatial quantities for events with $36 < E_e < 60$ MeV that satisfy selection VI. The expected Z distribution is sensitive to Δm^2 for oscillation events; we used $\Delta m^2 = 100$ eV². D is the distance from the phototube surfaces and D_{YZ} is the distance from the bottom, upstream end of the detector.

Distribution	Probability For All R	Probability for $R > 1.5$	Probability for $R > 30$.
X	0.074	0.763	0.147
Y	0.129	0.196	0.131
Z	0.047	0.713	0.889
D	0.314	0.739	0.620
D_{YZ}	0.016	0.535	0.891

TABLE VII. Consistency check on the time dependence of numbers of events with $R > 30$ and $36 < E_e < 60$ MeV. “Prob 1” is the probability of a worse inconsistency being observed. “Prob 2” is the probability of the 1995 excess accidentally being as low as observed given the overall excess.

	Selection I		Selection VI		Coulombs	$\bar{\nu}_\mu$	duty
	On	Off	On	Off		fraction	ratio
1993	2	8	2	7	1787	0.12	0.076
1994	7	9	11	15	5904	0.42	0.080
1995	4	23	9	14	7081	0.46	0.060
Prob 1	0.47		0.80				
Prob 2	0.19		0.46				

TABLE VIII. The number of signal and neutrino background events in the $20 < E_e < 60$ MeV energy range with selection VI, together with the oscillation probability if the observed excess is due to neutrino oscillations. Results are given for χ^2 and \mathcal{L} fits to the R distribution for all positrons and for the $R > 30$ sample.

Selection	Signal	Beam Off	ν Bkgd.	Excess	Oscillation Prob.
χ^2 R Fit	$64.3^{+18.5}_{-16.7}$	—	12.5 ± 2.9	$51.8^{+18.7}_{-16.9}$	$(0.31^{+0.11}_{-0.10} \pm 0.05)\%$
\mathcal{L} R Fit	$57.2^{+19.3}_{-18.0}$	—	12.5 ± 2.9	$44.7^{+19.5}_{-18.2}$	$(0.27^{+0.12}_{-0.11} \pm 0.04)\%$
$R > 30$	38	9.2 ± 0.8	7.7 ± 1.0	21.1 ± 6.3	$(0.55 \pm 0.16 \pm 0.07)\%$

FIGURES

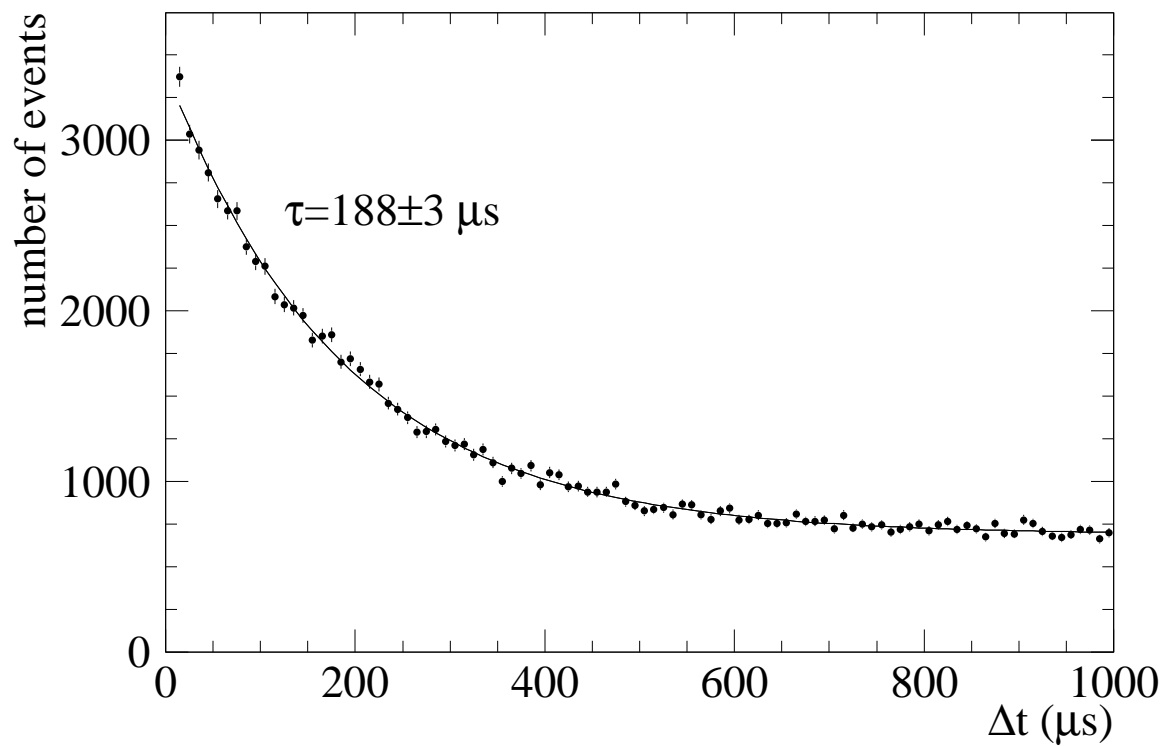


FIG. 1. Time difference between neutrons and subsequent photons for correlated plus accidental γ s. The solid curve is a fit to a sum of an exponential for correlated γ s and a flat background for accidental γ s.

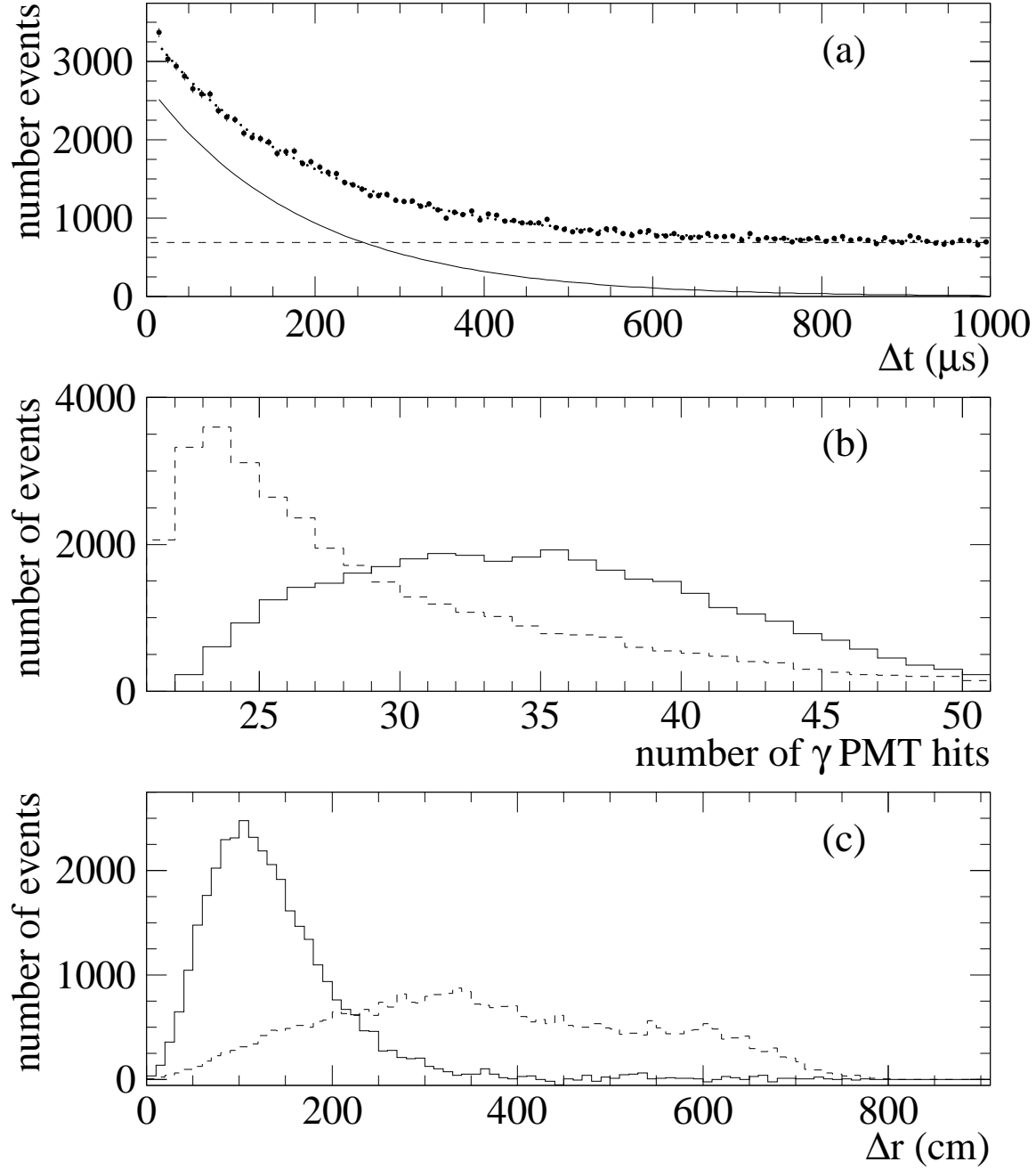


FIG. 2. Distributions obtained from cosmic-ray neutron data for γ s that are correlated (solid) or uncorrelated (dashed) with the primary event: (a) the time between the photon and primary event; (b) the number of photon PMT hits; (c) the distance between the photon and primary event. The raw data points are also shown in (a).

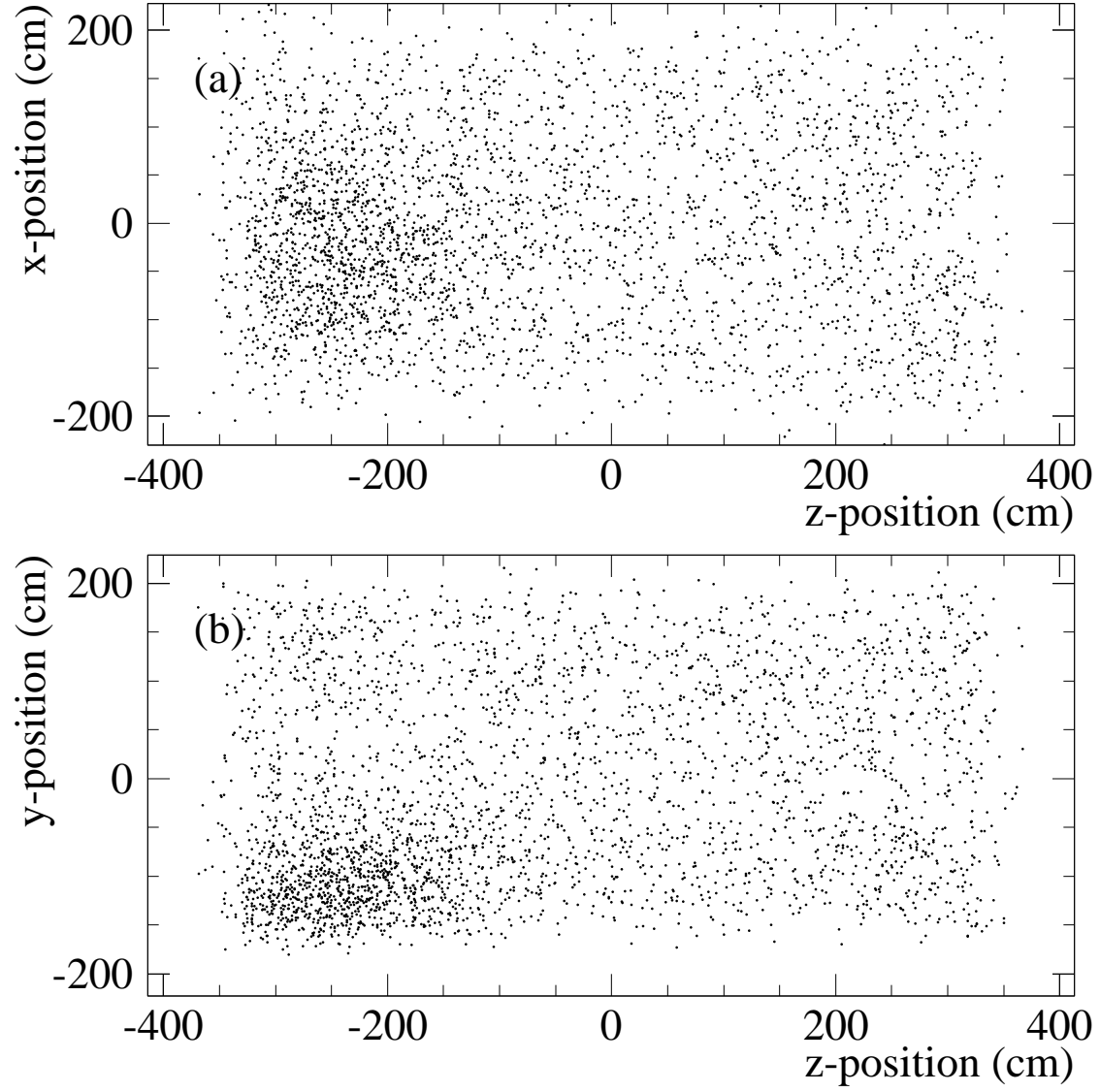


FIG. 3. Distributions of reconstructed position for accidental γ s in the (a) X - Z and (b) Y - Z projections.

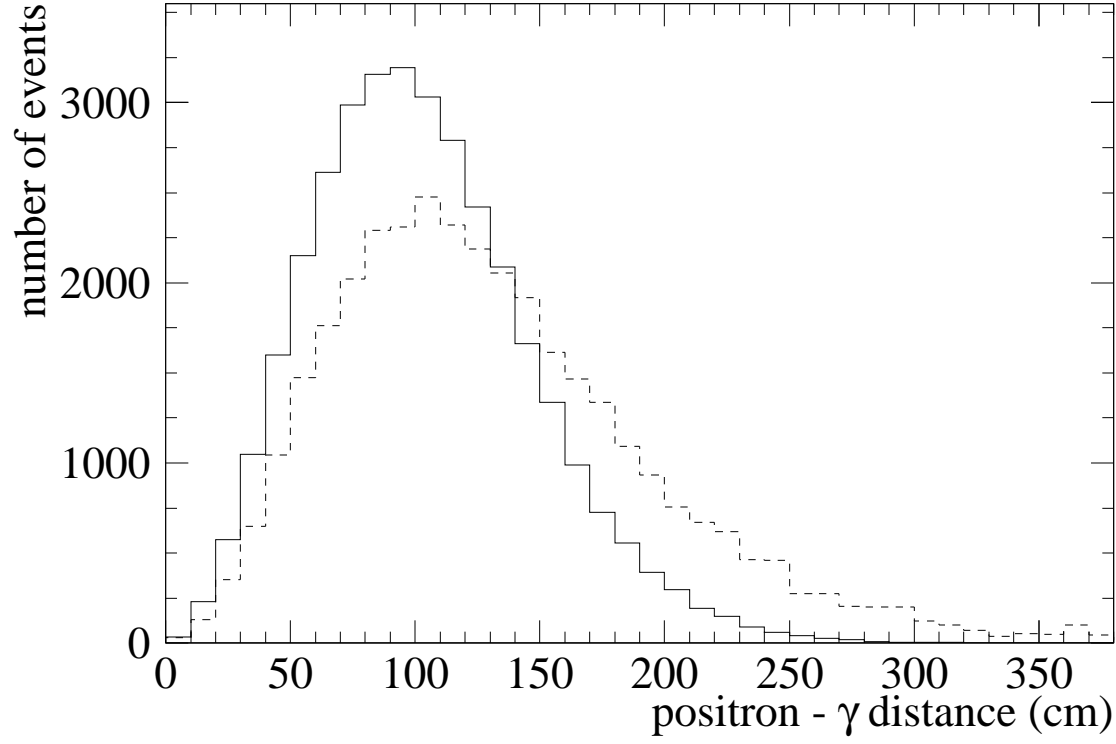


FIG. 4. Distribution of reconstructed distance between e^+ and a correlated γ from the Monte Carlo simulation (solid) and the cosmic ray neutron sample (dashed).

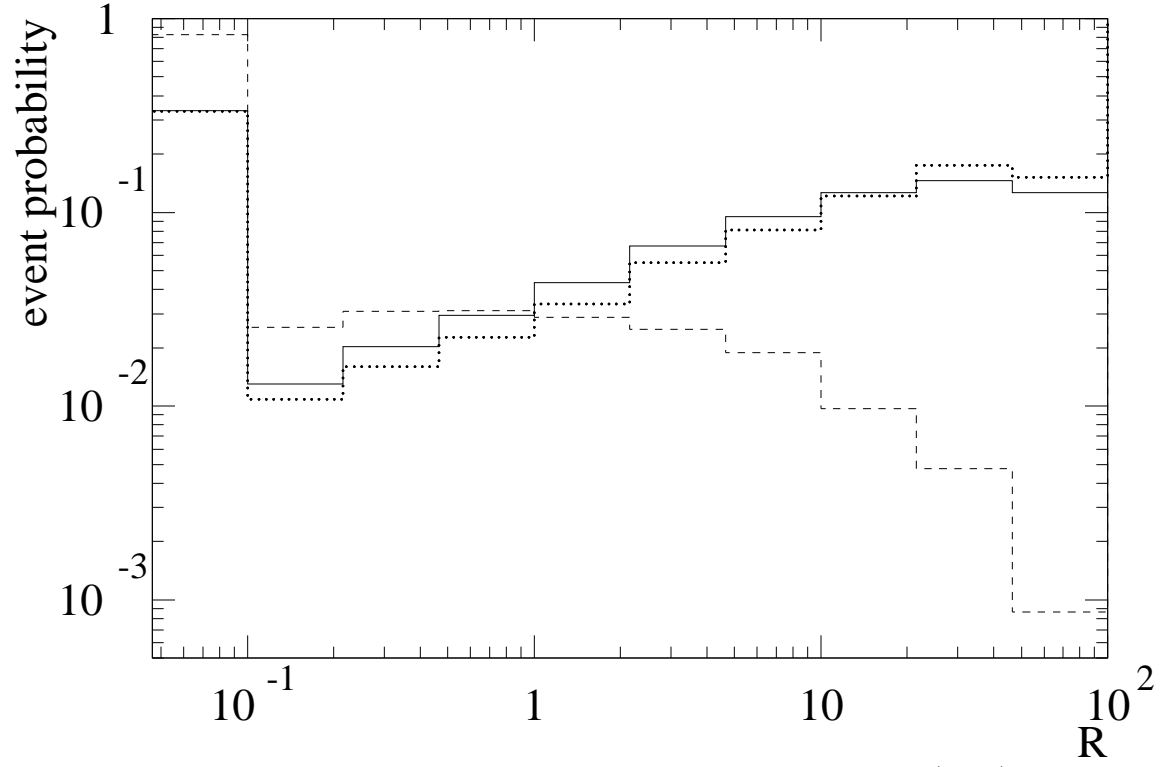


FIG. 5. Measured R distribution for events with the γ correlated (solid) and uncorrelated (dashed) with the primary event. The dotted curve is also for correlated γ s, but with the measured Δr values replaced by values distributed according to the Monte Carlo prediction.

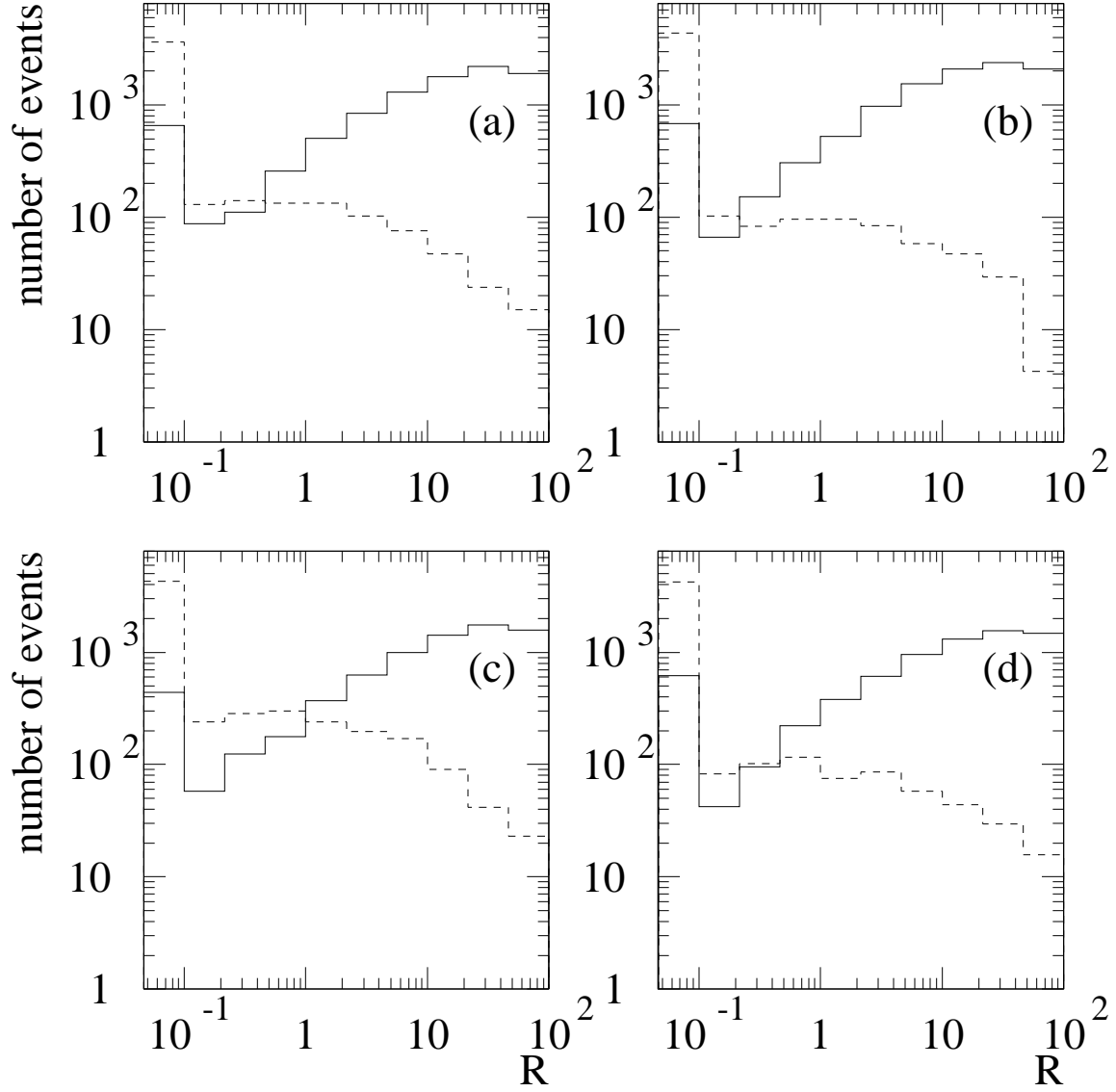


FIG. 6. The R distributions for correlated γ s (solid) and accidental γ s (dashed) for primary events in each of the four quadrants of the Y - Z plane: (a) $Y > 0, Z < 0$; (b) $Y > 0, Z > 0$; (c) $Y < 0, Z < 0$; (d) $Y < 0, Z > 0$.

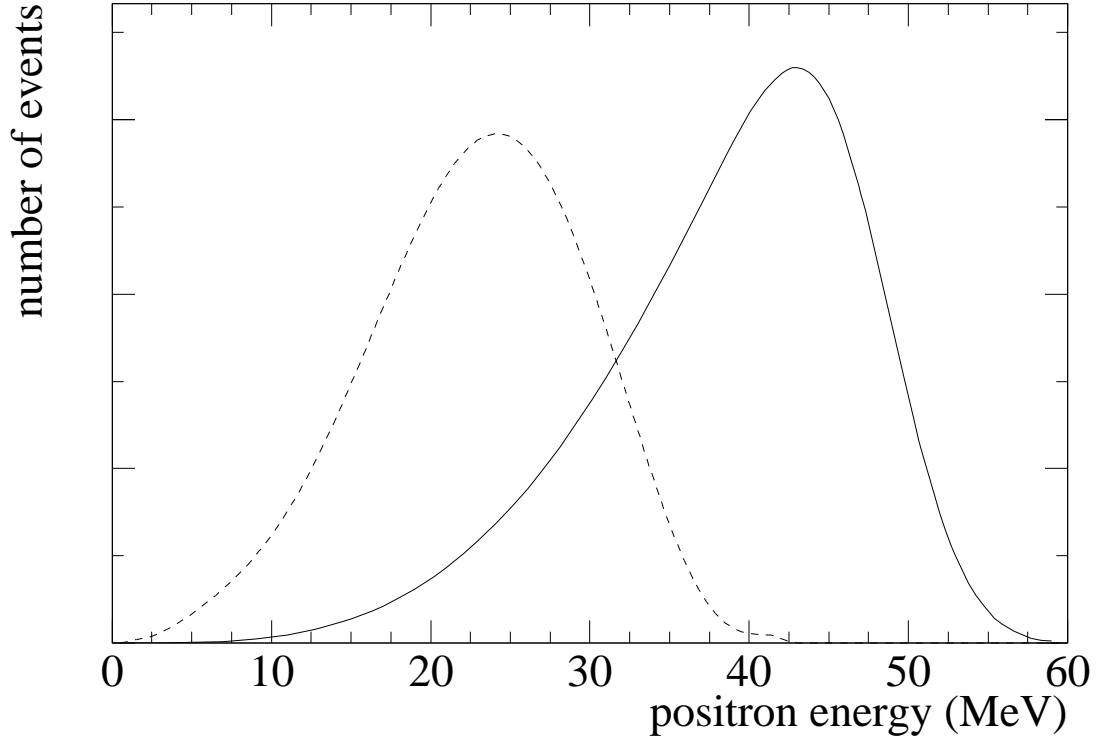


FIG. 7. Energy distribution expected for oscillation events at large Δm^2 ($\Delta m^2 \rightarrow \infty$) (solid) and $\nu_e C$ scattering events (dashed). The distributions include the experimental energy resolution as determined from the sample of electron events from muon decay.

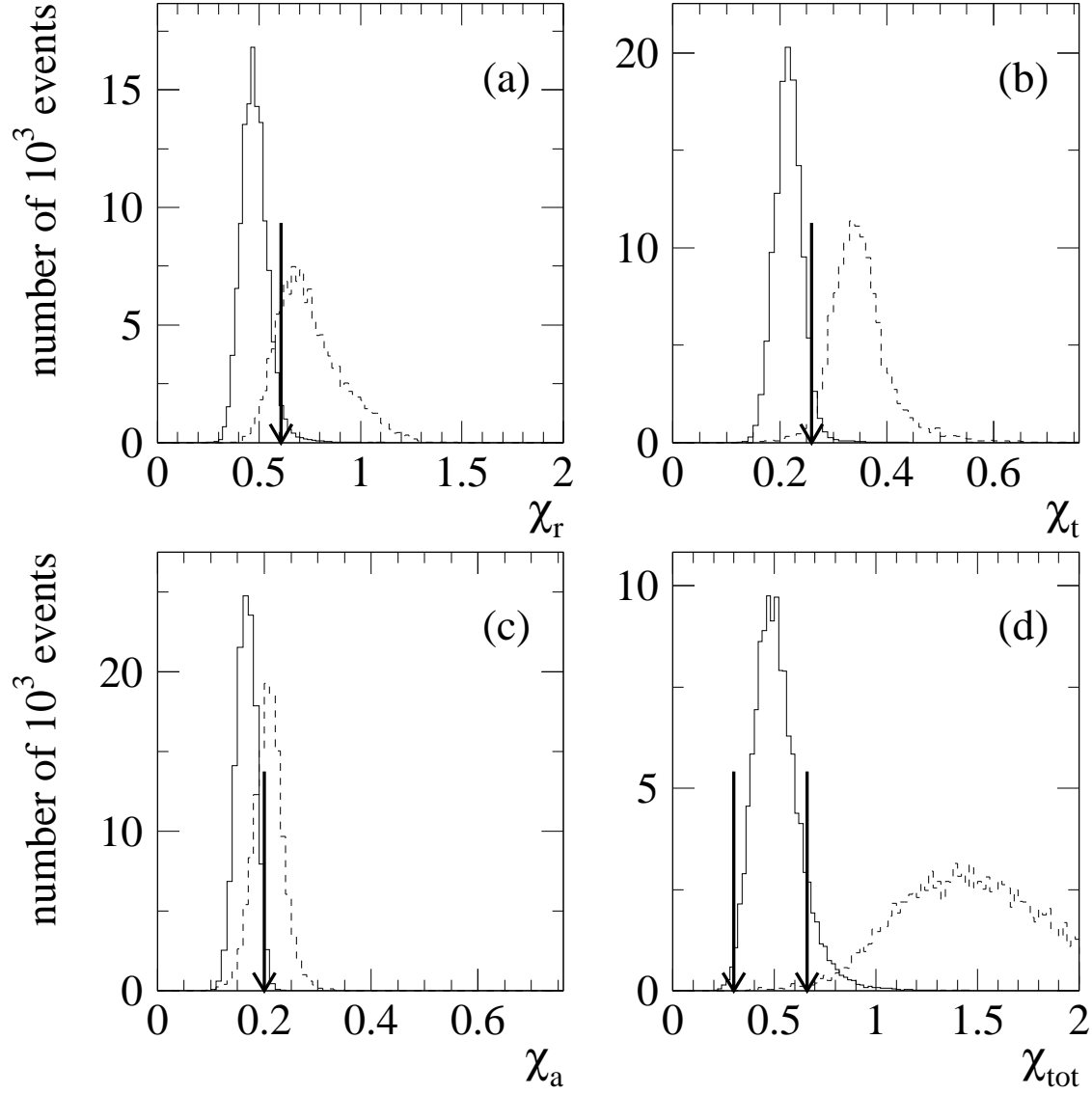


FIG. 8. Distribution of the PID parameters for decay electrons (solid) and neutrons (dashed) with deposited energy between $36 < E_e < 60$ MeV. (a) χ_r ; (b) χ_t ; (c) χ_a ; (d) χ_{tot} . The arrows show the locations of the χ requirements for selection VI.

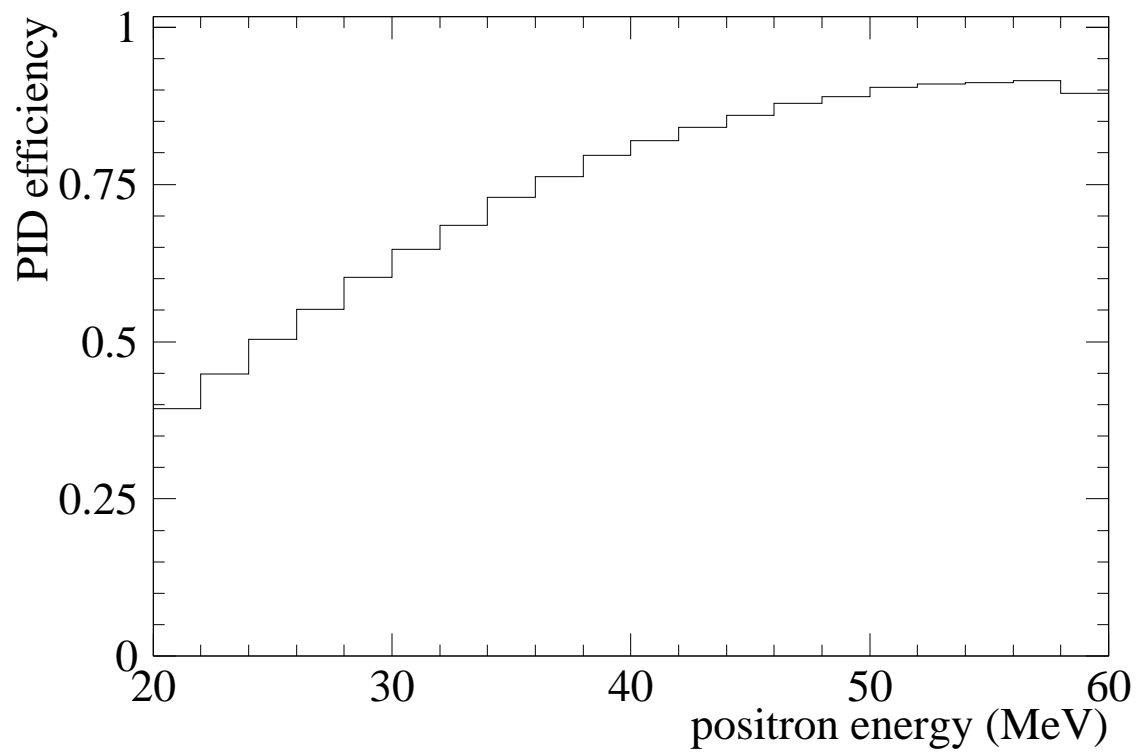


FIG. 9. The PID efficiency for selection VI as a function of electron energy.

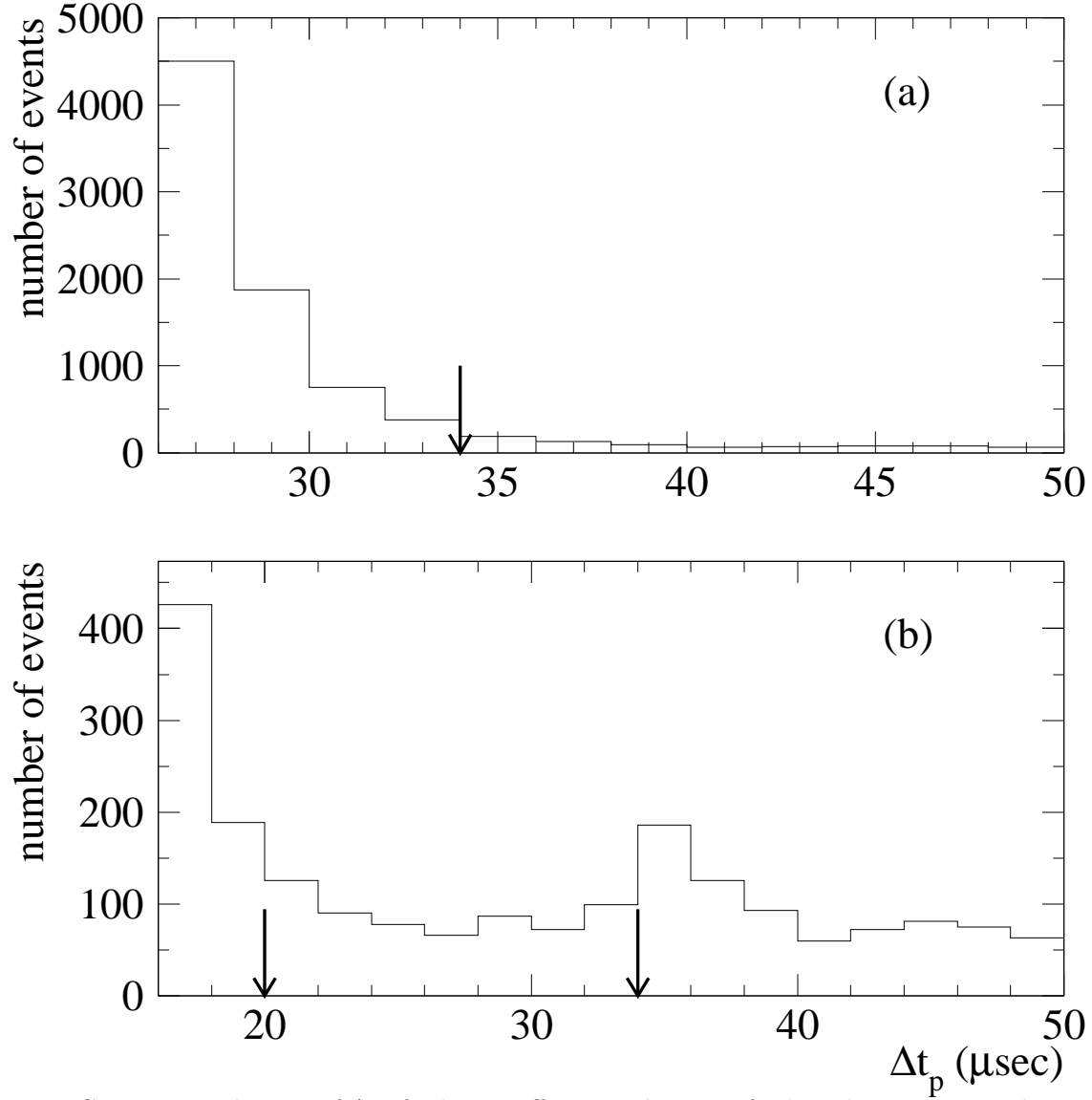


FIG. 10. Distribution of Δt_p for beam-off events that satisfy the other positron selection criteria for (a) events with no Δt_p requirement and (b) events with no correlated activities within $34 \mu\text{s}$. The arrows show the locations of the Δt_p requirements.

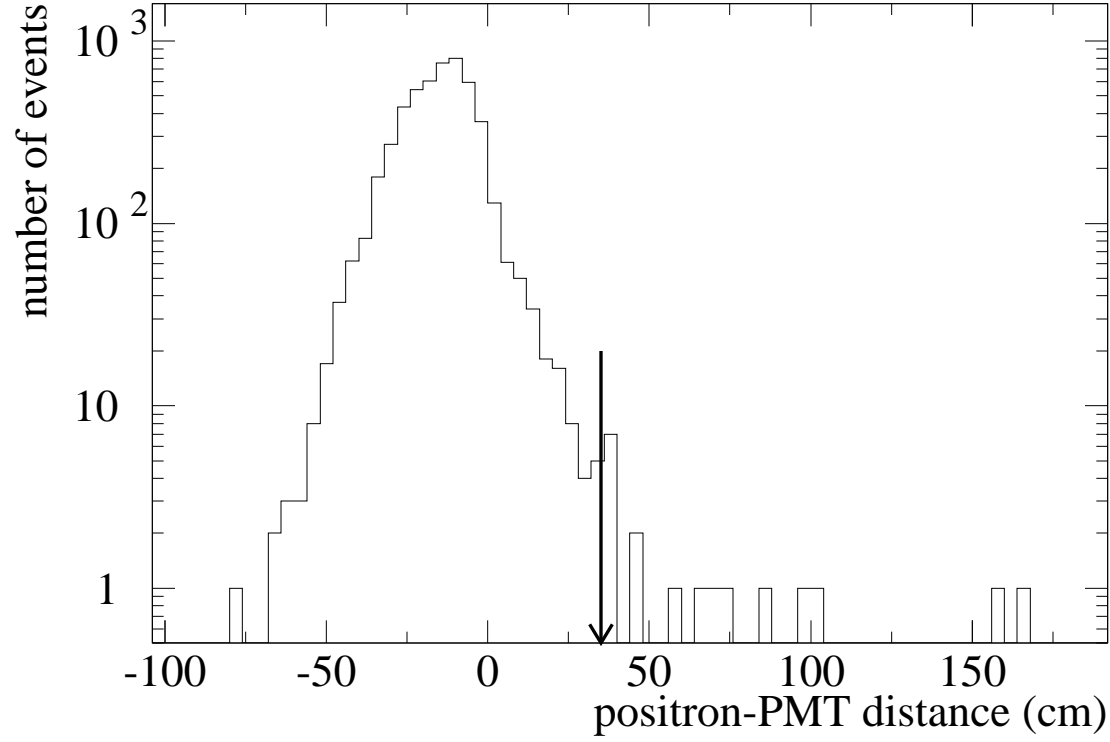


FIG. 11. The D distribution, the reconstructed distance from the PMT surfaces, for a sample of Monte Carlo electron events generated behind the PMT surfaces. The arrow shows the location of the $D > 35$ cm cut.

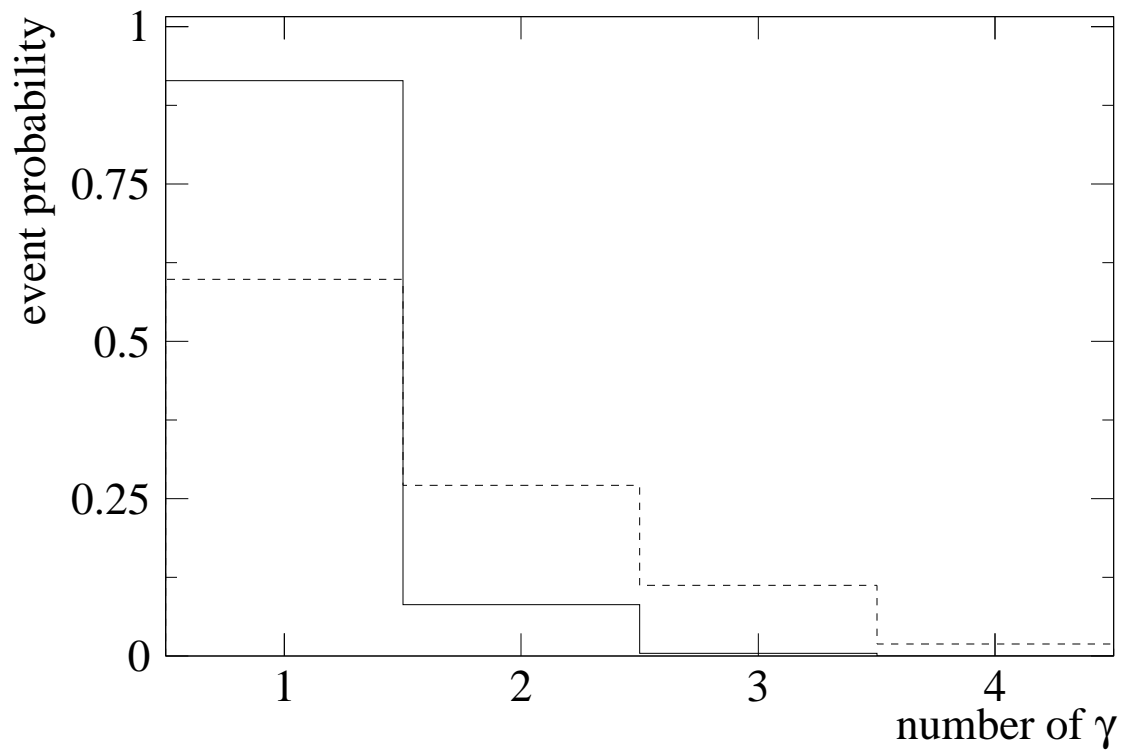


FIG. 12. Number of associated γ s ($R > 1.5$) distribution expected for oscillation events (solid) and for beam-off events (dashed).

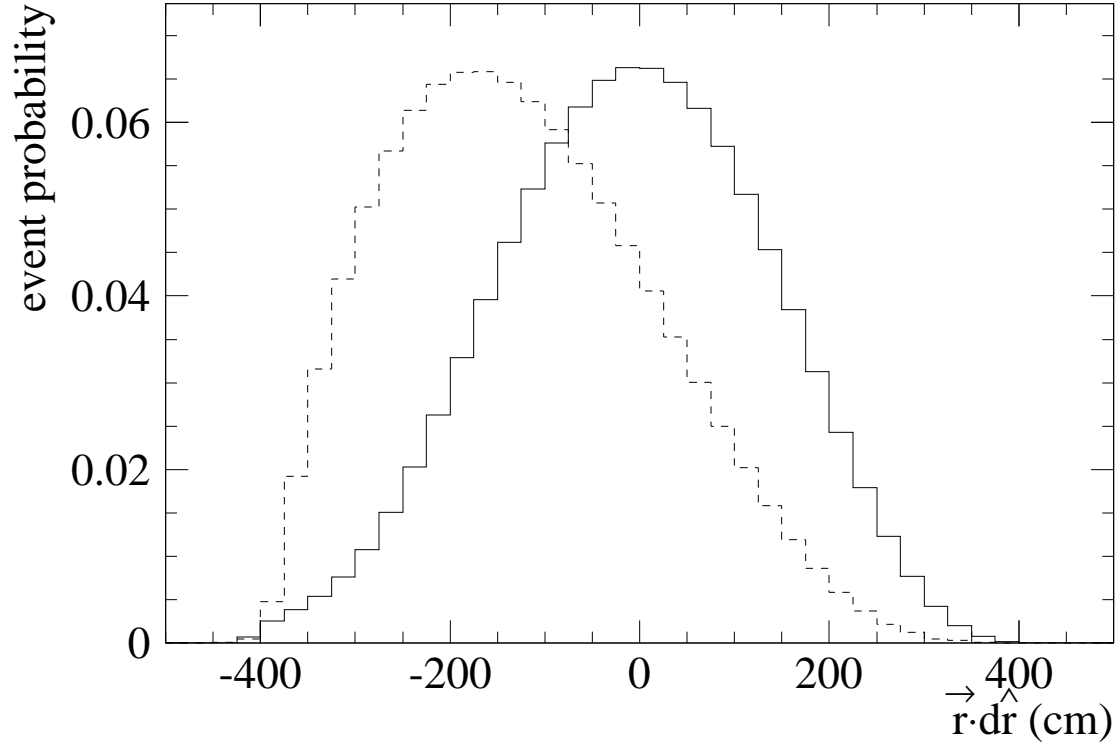


FIG. 13. Distribution of $\vec{r} \cdot \hat{dr}$ for $\nu_e C$ events (solid) and beam-off events (dashed).

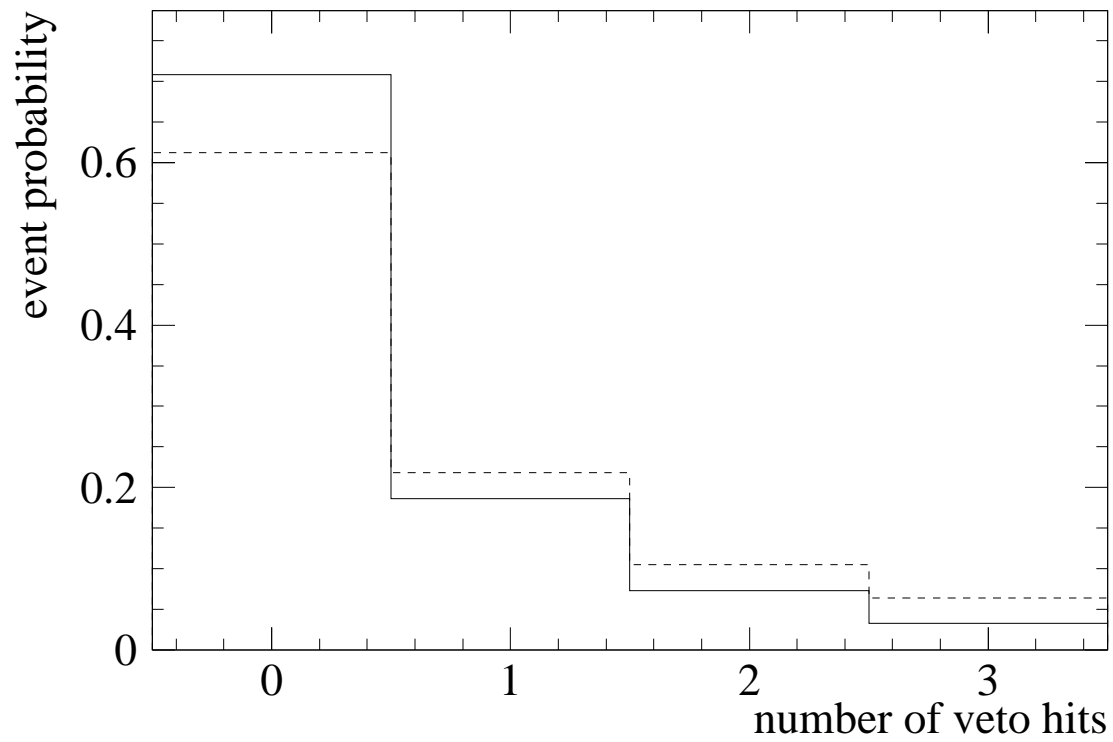


FIG. 14. Distribution of veto hits for laser events (solid) and beam-off events (dashed).

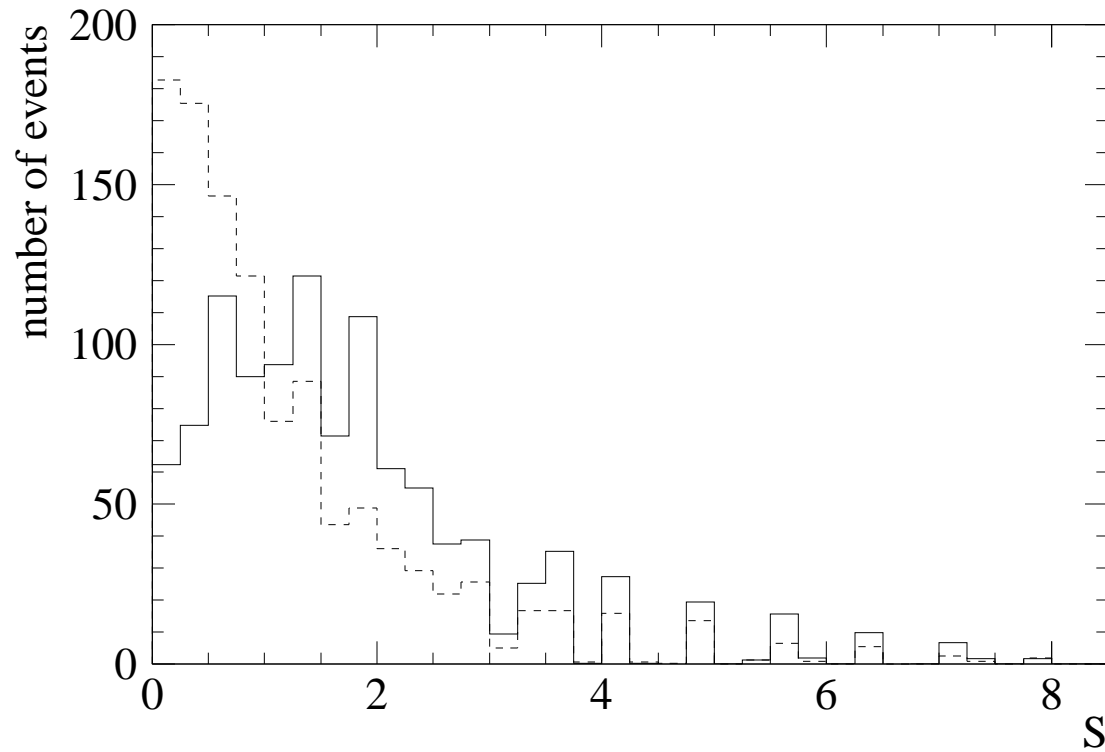


FIG. 15. Distribution of S for $\nu_e C$ events (solid) and beam-off events (dashed).

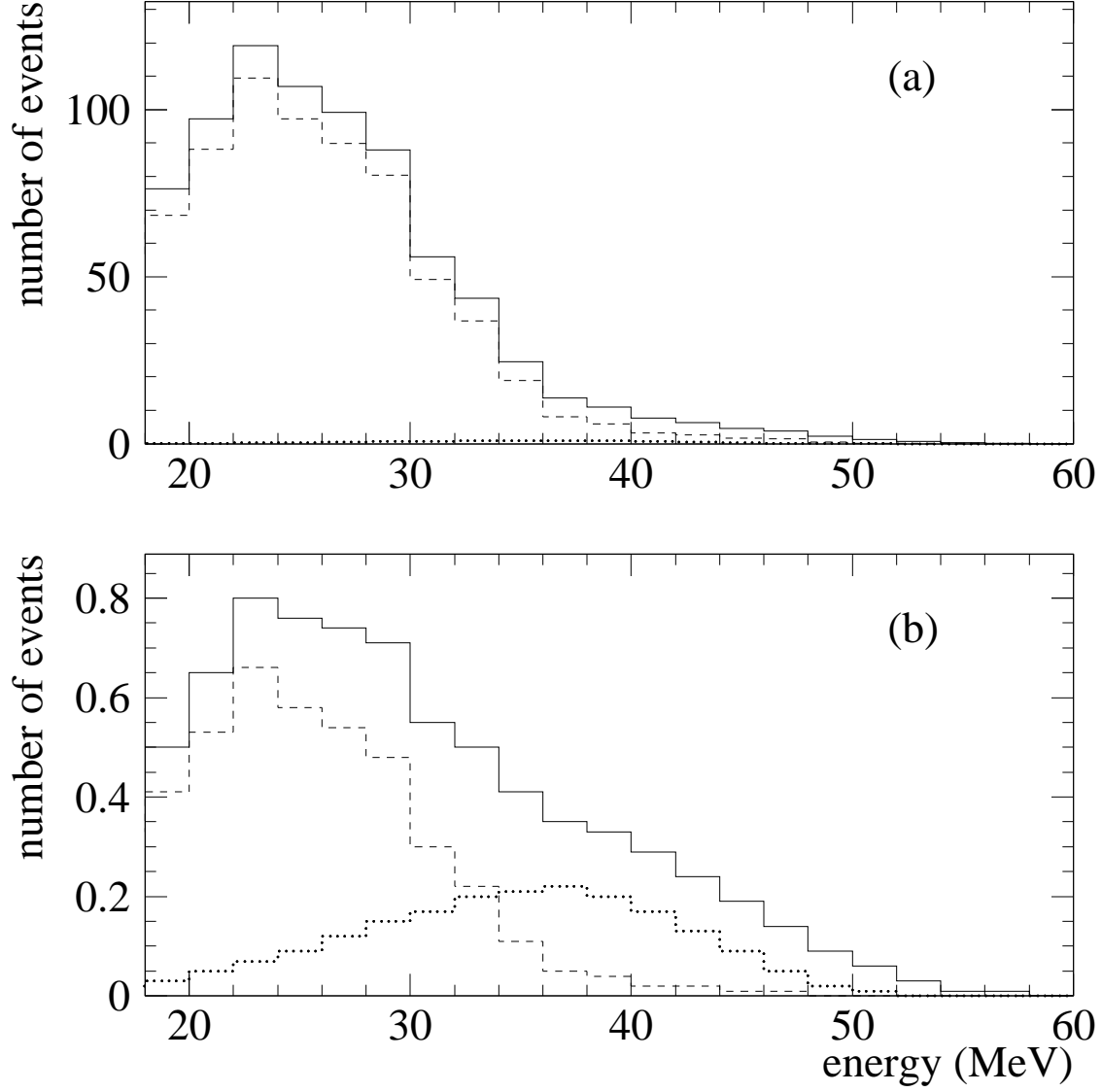


FIG. 16. Total beam-related background (solid curve) calculated as a function of energy for (a) $R \geq 0$ and (b) $R > 30$. Also shown are the contributions from the backgrounds $\nu_e C \rightarrow e^- X$ scattering (dashed curve) and μ^- DAR (dotted curve).

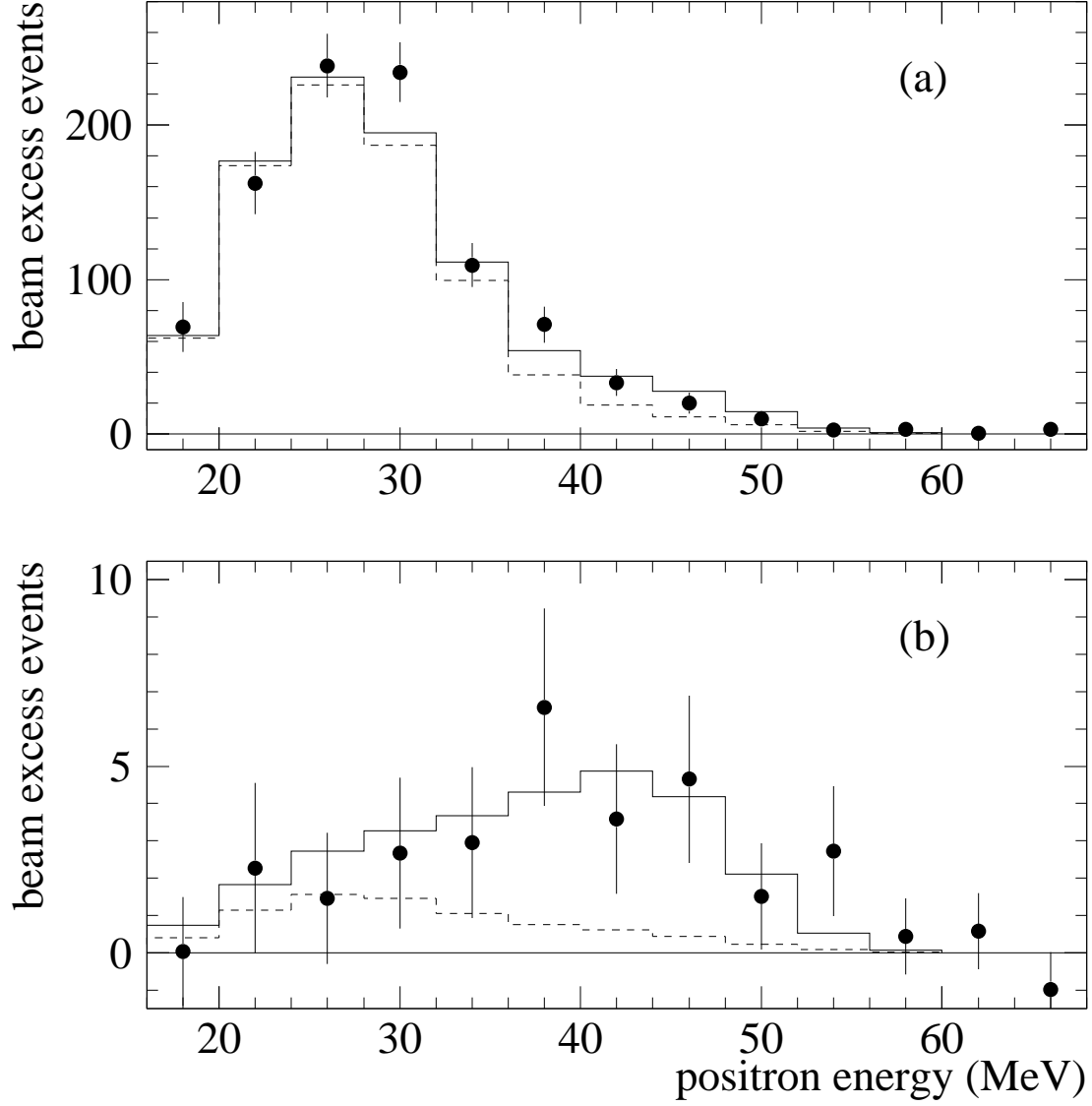


FIG. 17. The energy distribution for events with (a) $R \geq 0$ and (b) $R > 30$. Shown in the figure are the beam-excess data, estimated neutrino background (dashed), and expected distribution for neutrino oscillations at large Δm^2 plus estimated neutrino background (solid).

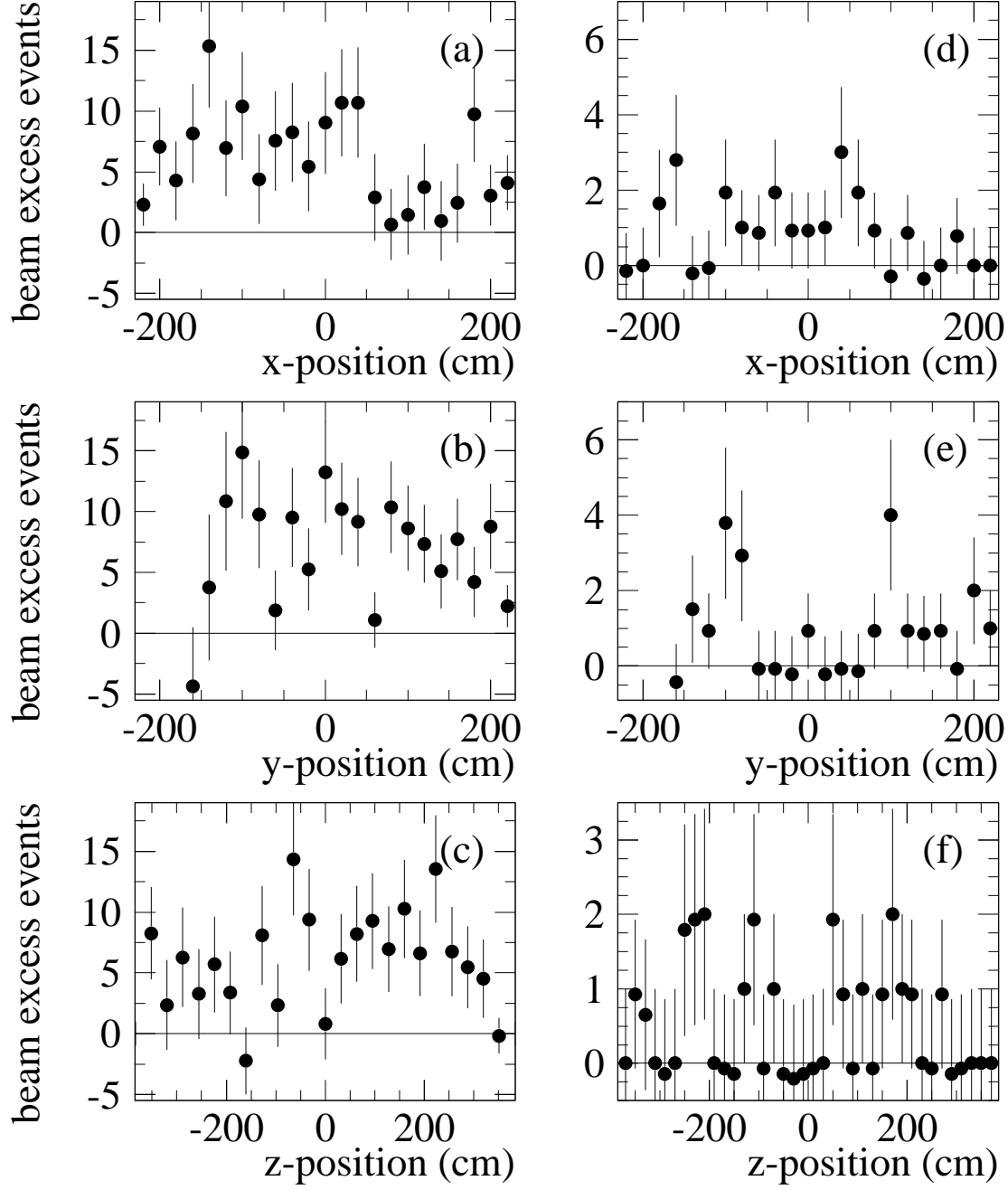


FIG. 18. The spatial distributions for beam-excess data events with $36 < E_e < 60$ MeV. (a) - (c) are for $R \geq 0$ and (d) - (f) are for $R > 30$.

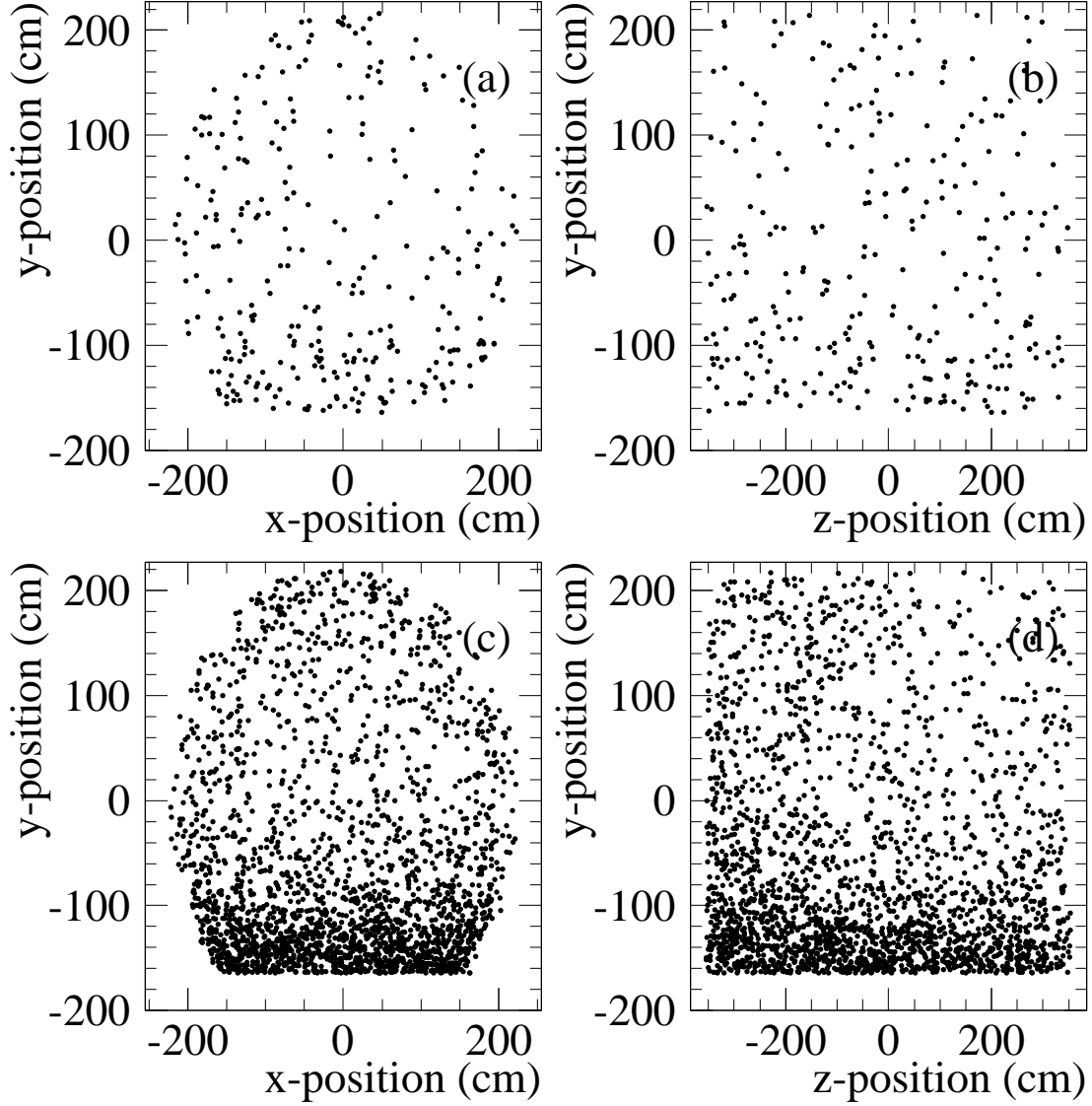


FIG. 19. Spatial distributions of positron events with $36 < E_e < 60$ MeV and $R \geq 0$ in the y - x and Y - Z planes for (a,b) the 300 beam-on events and (c,d) the 2293 beam-off events. Note that the beam on-off excess is 139.5 events, so that less than half of the 300 beam-on events are due to neutrino interactions.

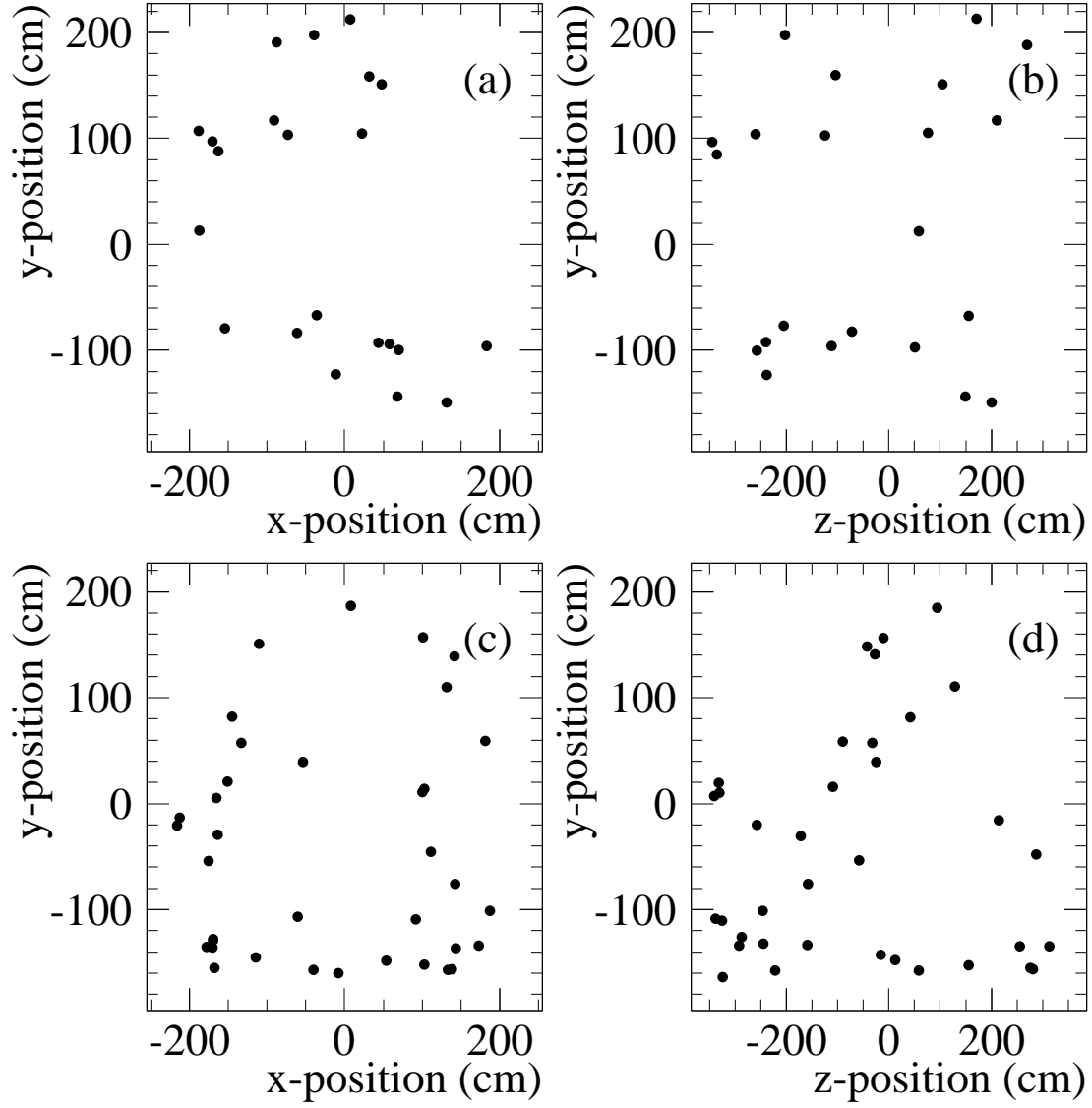


FIG. 20. Spatial distributions of data events with $36 < E_e < 60$ MeV and $R > 30$ in the y - x and Y - Z planes for (a,b) the 22 beam-on events and (c,d) the 36 beam-off events.

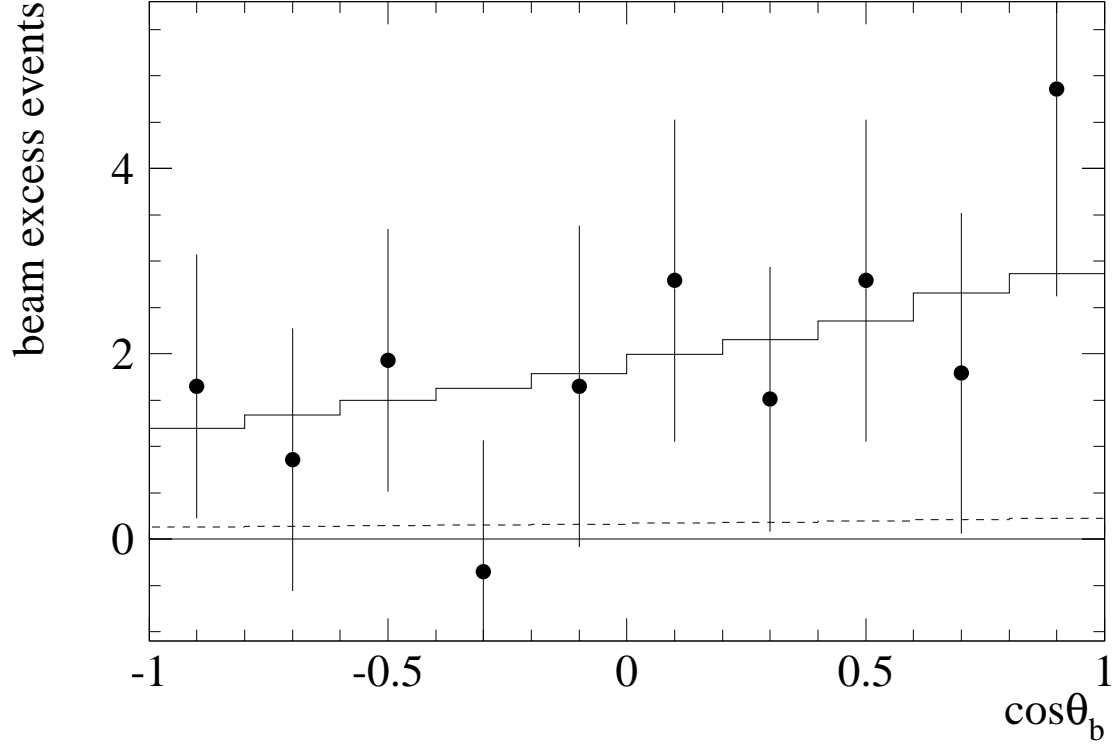


FIG. 21. The $\cos \theta_b$ distribution for beam-excess data events with $36 < E_e < 60$ MeV and $R > 30$ and that expected for neutrino oscillations at large Δm^2 (solid). The dashed curve is the estimated neutrino background. θ_b is the e^+ angle with respect to the neutrino direction.

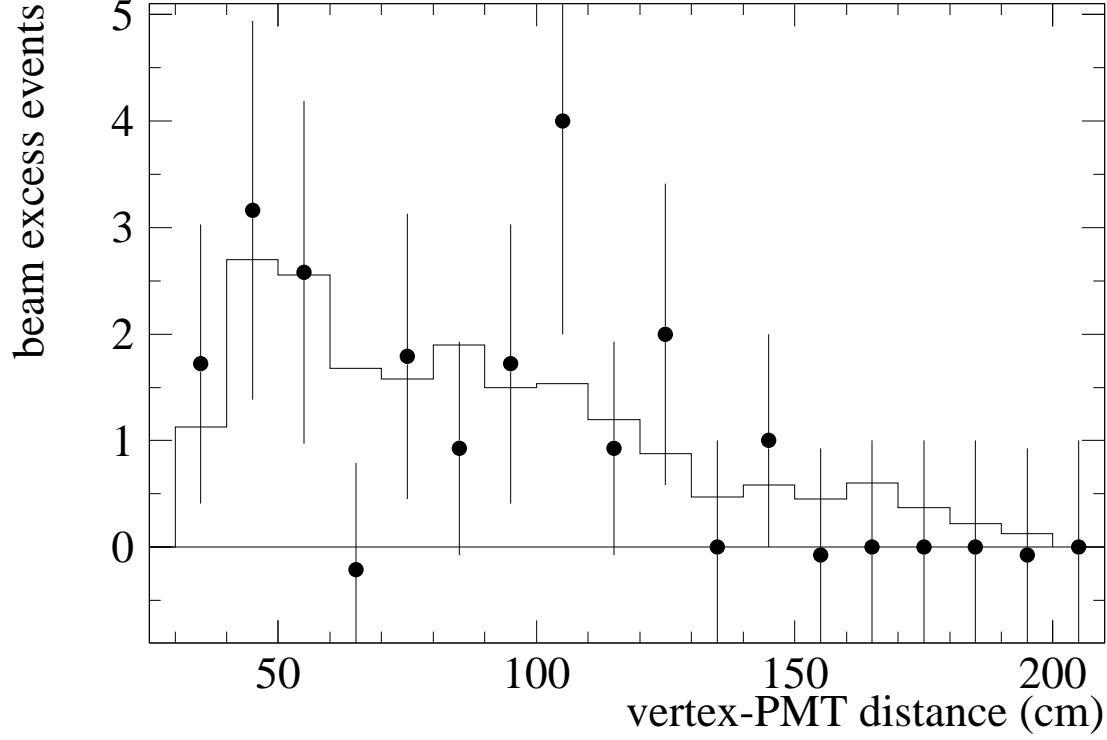


FIG. 22. Distribution of D , the distance of the reconstructed vertex from the PMT surfaces, for beam-excess data events with $36 < E_e < 60$ MeV and $R > 30$. The solid histogram is the expected distribution obtained from a sample of $\nu_e C \rightarrow e^- X$ scattering events.

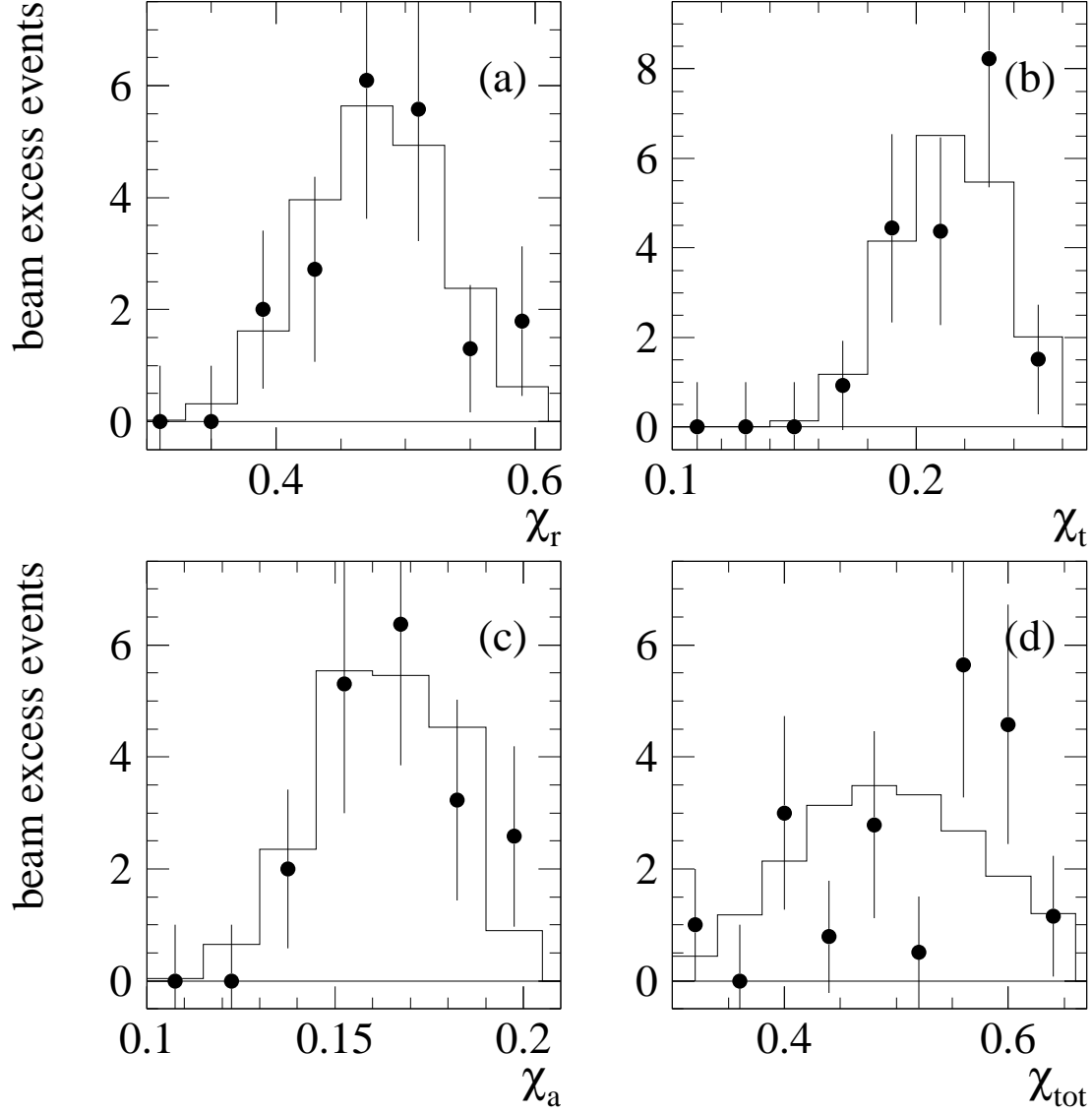


FIG. 23. Distribution of the χ parameters for beam-excess data events with $36 < E_e < 60$ MeV and $R > 30$: (a) χ_r , (b) χ_t , (c) χ_a , (d) χ_{tot} . The solid histograms are the expected distributions obtained from a sample of electrons from muon decay.

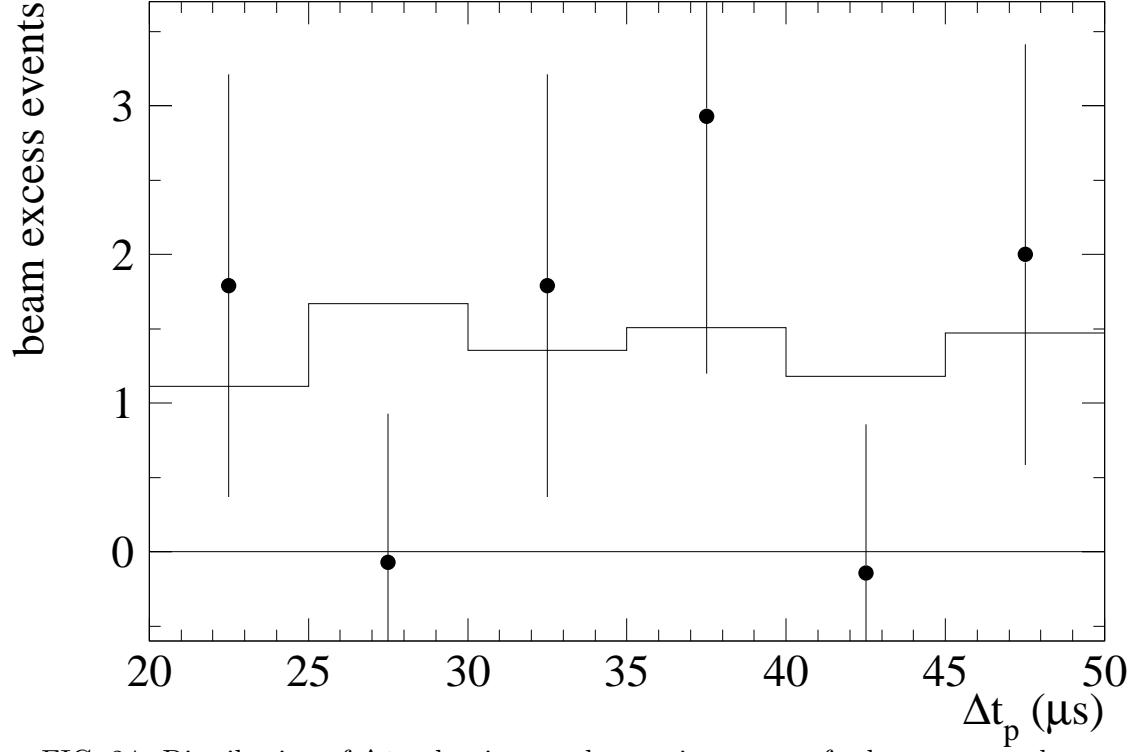


FIG. 24. Distribution of Δt_p , the time to the previous event, for beam-excess data events with $36 < E_e < 60$ MeV and $R > 30$ and with activities within $50 \mu s$. The solid histogram is the expected distribution obtained from a sample of $\nu_e C \rightarrow e^- X$ scattering events.

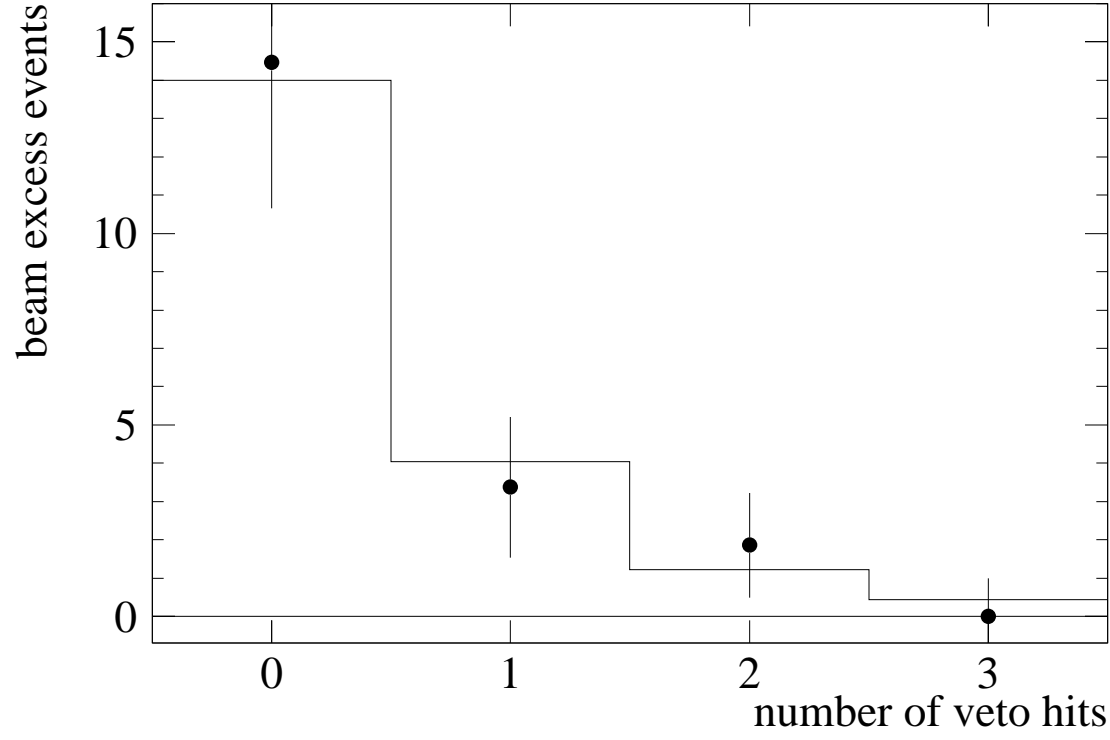


FIG. 25. Distribution of veto hits for beam-excess data events with $36 < E_e < 60$ MeV and $R > 30$. The solid histogram is the expected distribution obtained from a sample of $\nu_e C \rightarrow e^- X$ scattering events.

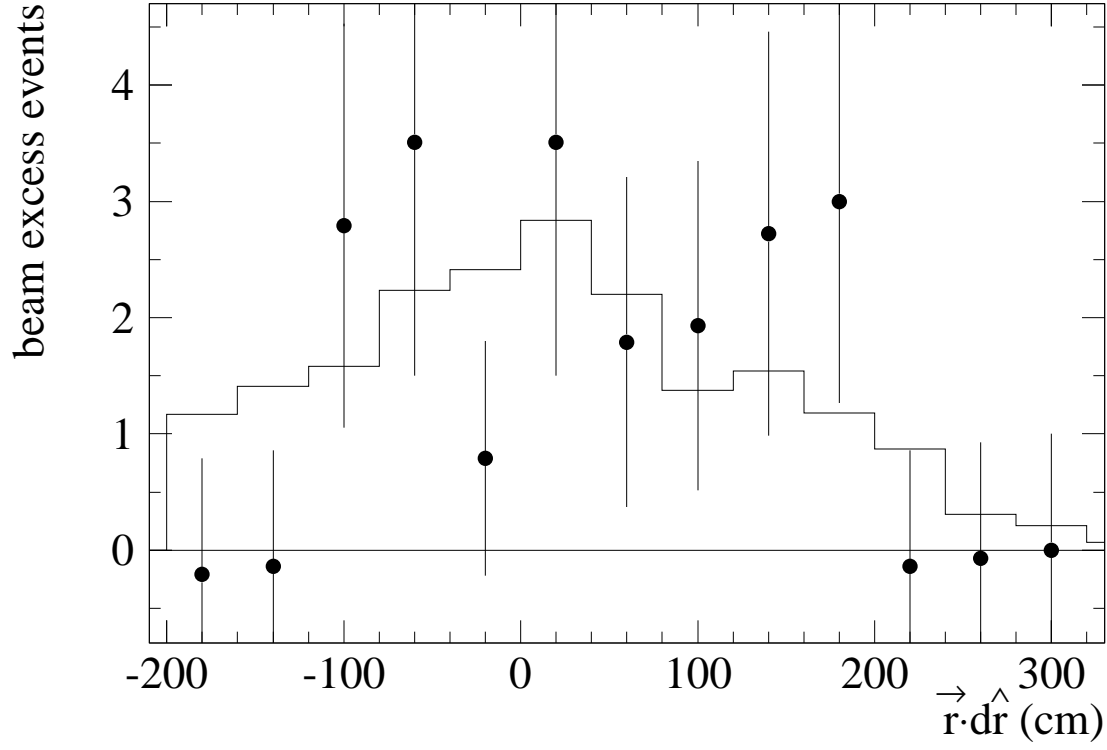


FIG. 26. Distribution of $\vec{r} \cdot \hat{d}r$ for beam-excess data events with $36 < E_e < 60$ MeV and $R > 30$. The solid histogram is the expected distribution obtained from a sample of $\nu_e C \rightarrow e^- X$ scattering events. The $S > 0.5$ cut eliminates all events with $\vec{r} \cdot \hat{d}r < -200$ cm.

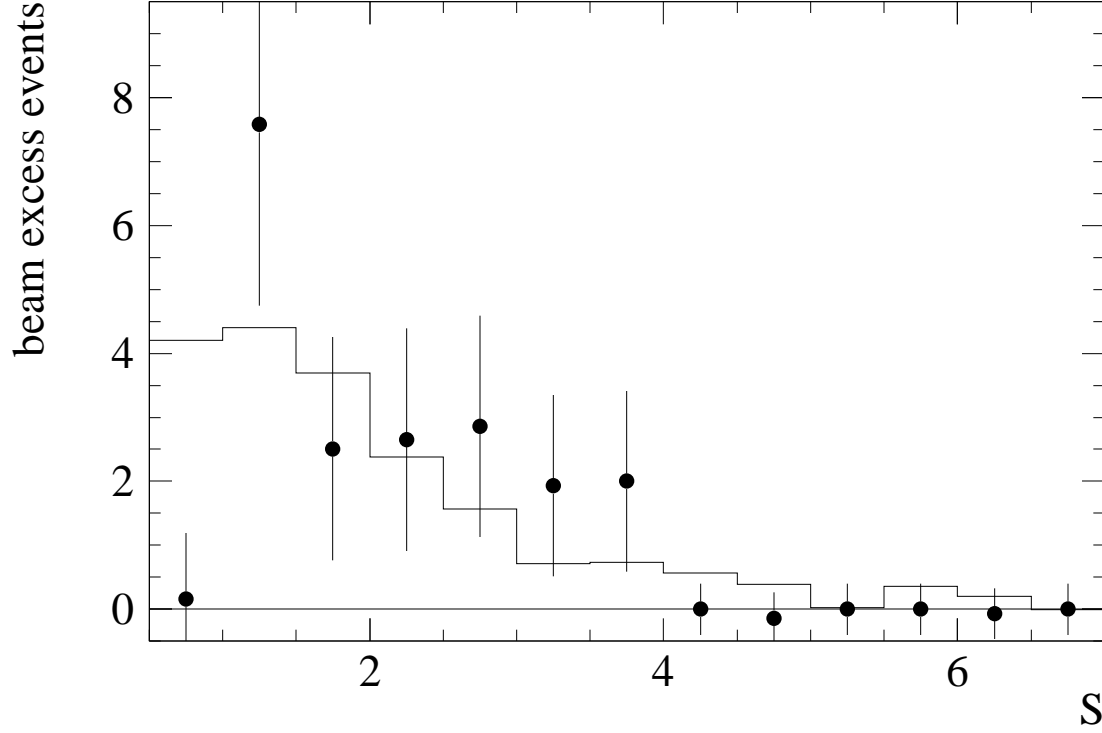


FIG. 27. Distribution of the likelihood ratio, S , for beam-excess data events with $36 < E_e < 60$ MeV and $R > 30$. The solid histogram is the expected distribution obtained from a sample of $\nu_e C \rightarrow e^- X$ scattering events.

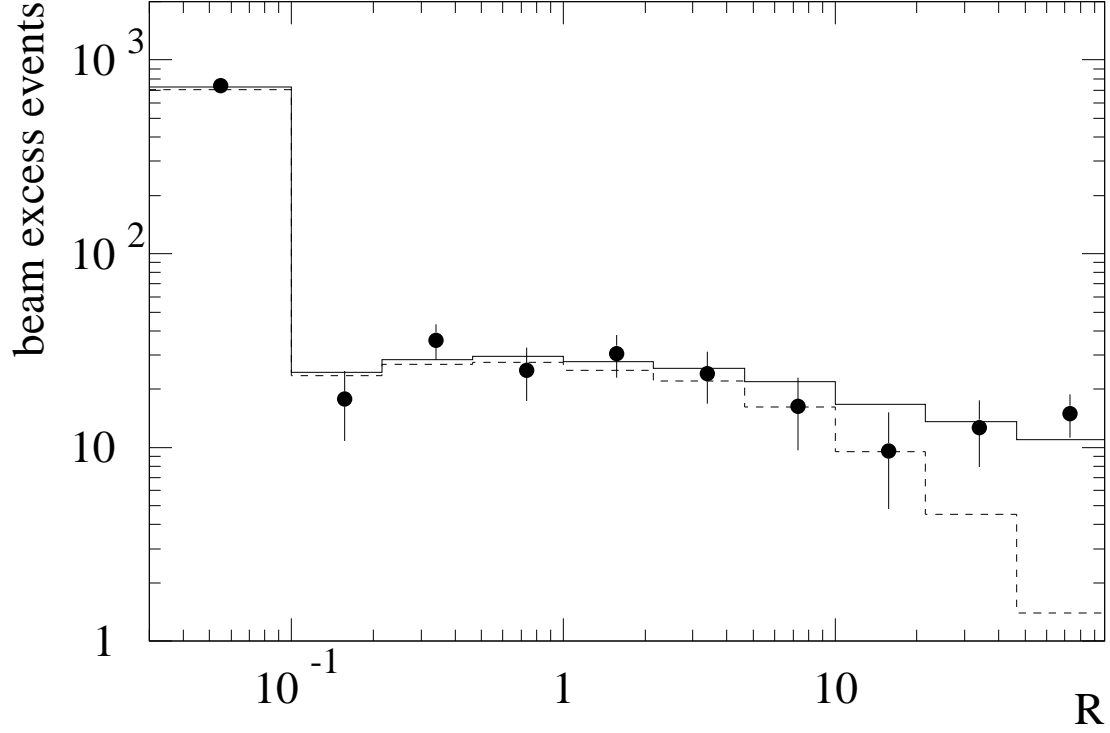


FIG. 28. The R distribution, beam on minus beam off excess, for events that satisfy selection VI and that have energies in the range $20 < E_e < 60$ MeV. The solid curve is the best fit to the data, while the dashed curve is the component of the fit with an uncorrelated γ .

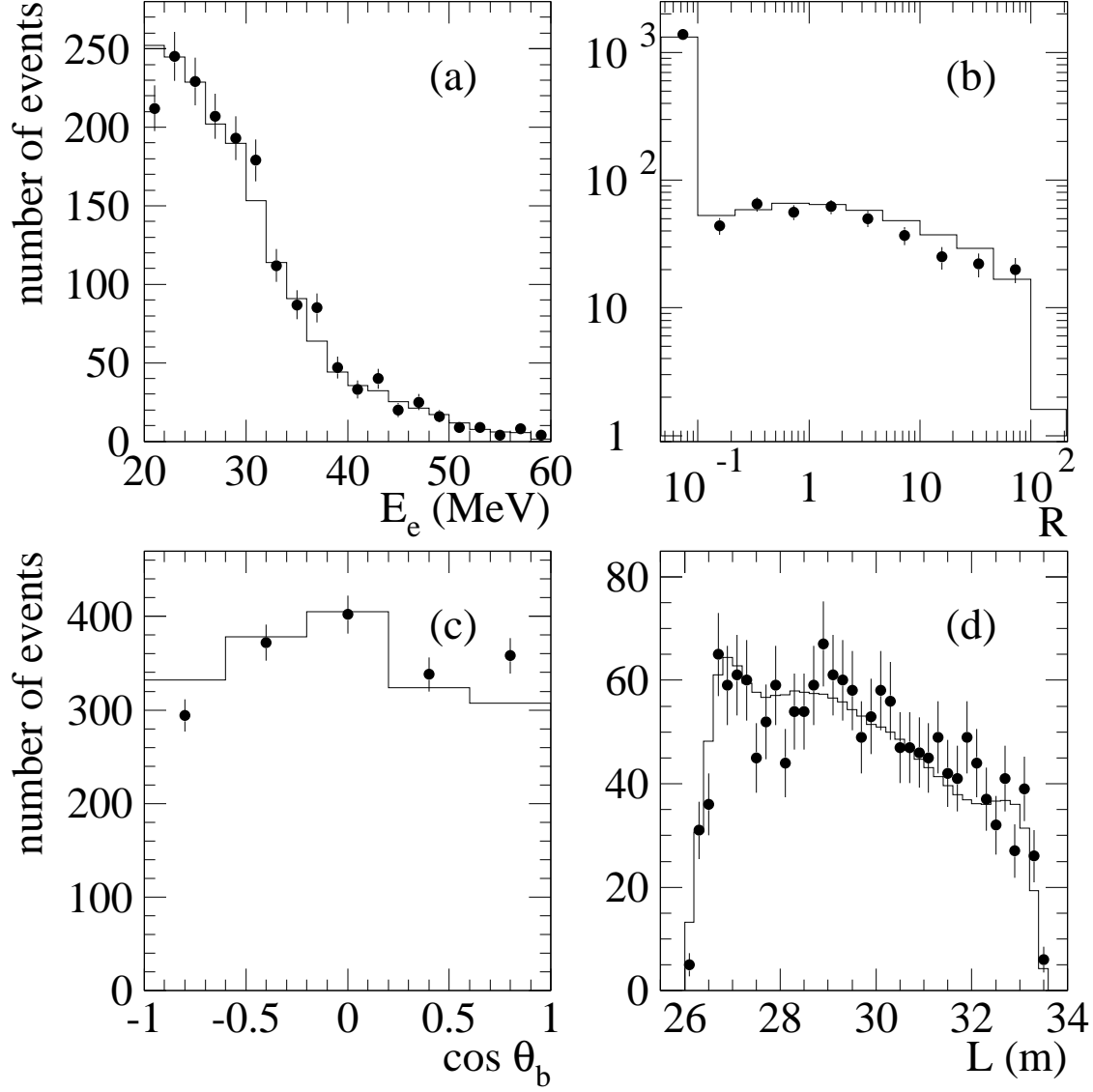


FIG. 29. Distributions of E_e , R , $\cos \theta_b$, and L for the beam-on sample compared with the expected distributions (including oscillations at 19eV^2 , $\sin^2 2\theta = 0.006$).

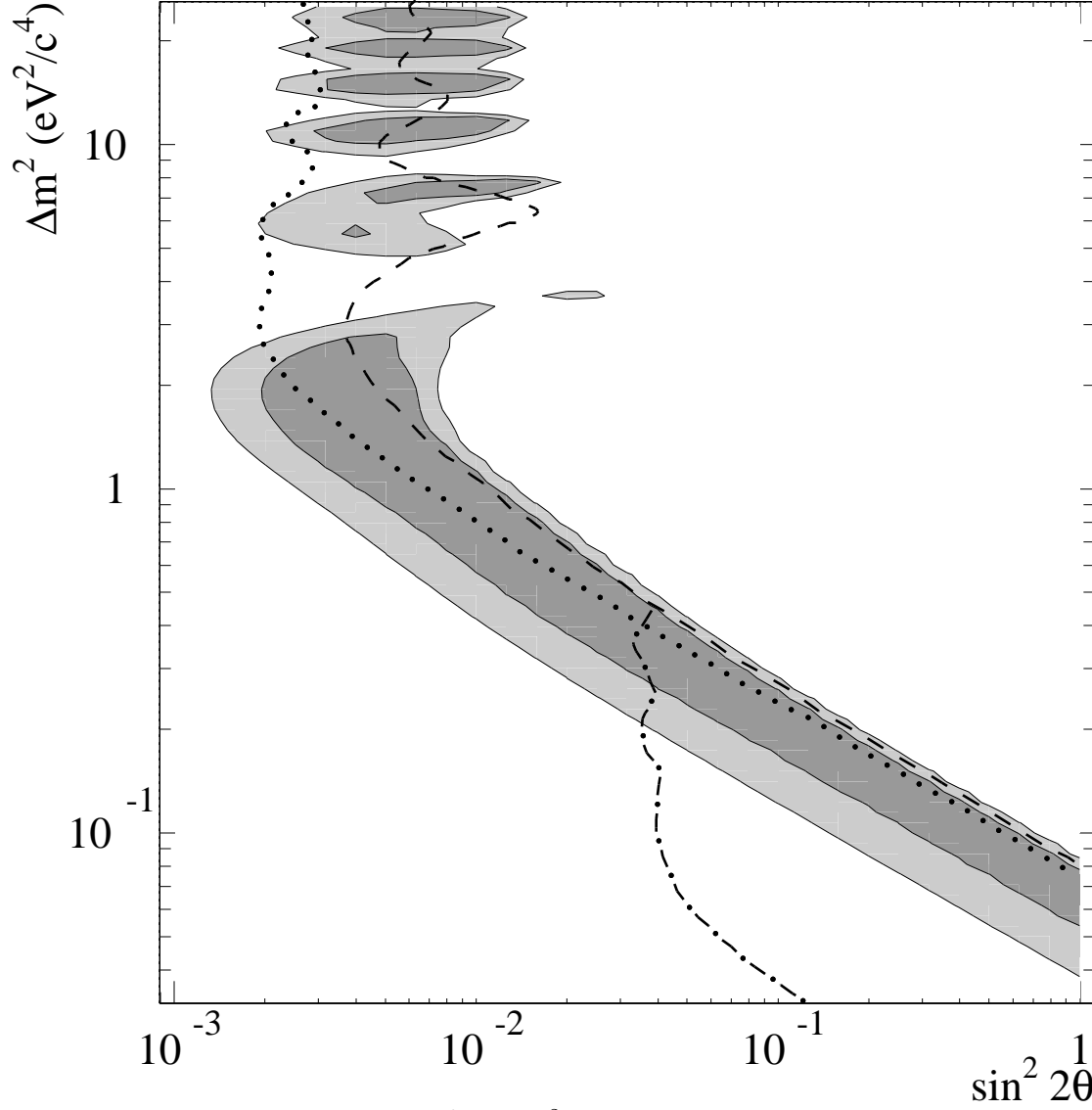


FIG. 30. Plot of the LSND Δm^2 vs $\sin^2 2\theta$ favored regions. The method used to obtain these contours is described in the text. The darkly-shaded and lightly-shaded regions correspond to 90% and 99% likelihood regions after the inclusion of the effects of systematic errors. Also shown are 90% C.L. limits from KARMEN at ISIS (dashed curve), E776 at BNL (dotted curve), and the Bugey reactor experiment (dot-dashed curve).

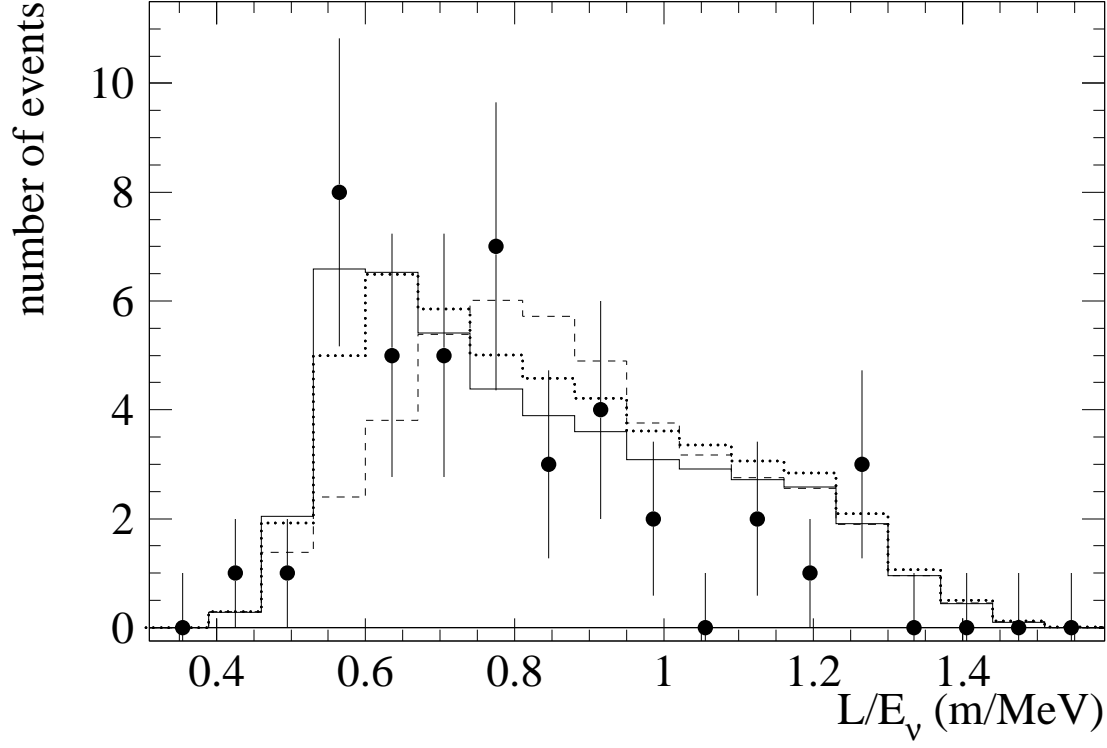


FIG. 31. Distribution of L/E_ν for the beam-on data with high R compared with the expected distributions at ($19eV^2, \sin^2 2\theta = 0.006$: solid line), ($4.3eV^2, \sin^2 2\theta = 0.01$: dashed line), and ($0.06eV^2, \sin^2 2\theta = 1$.: dotted line).

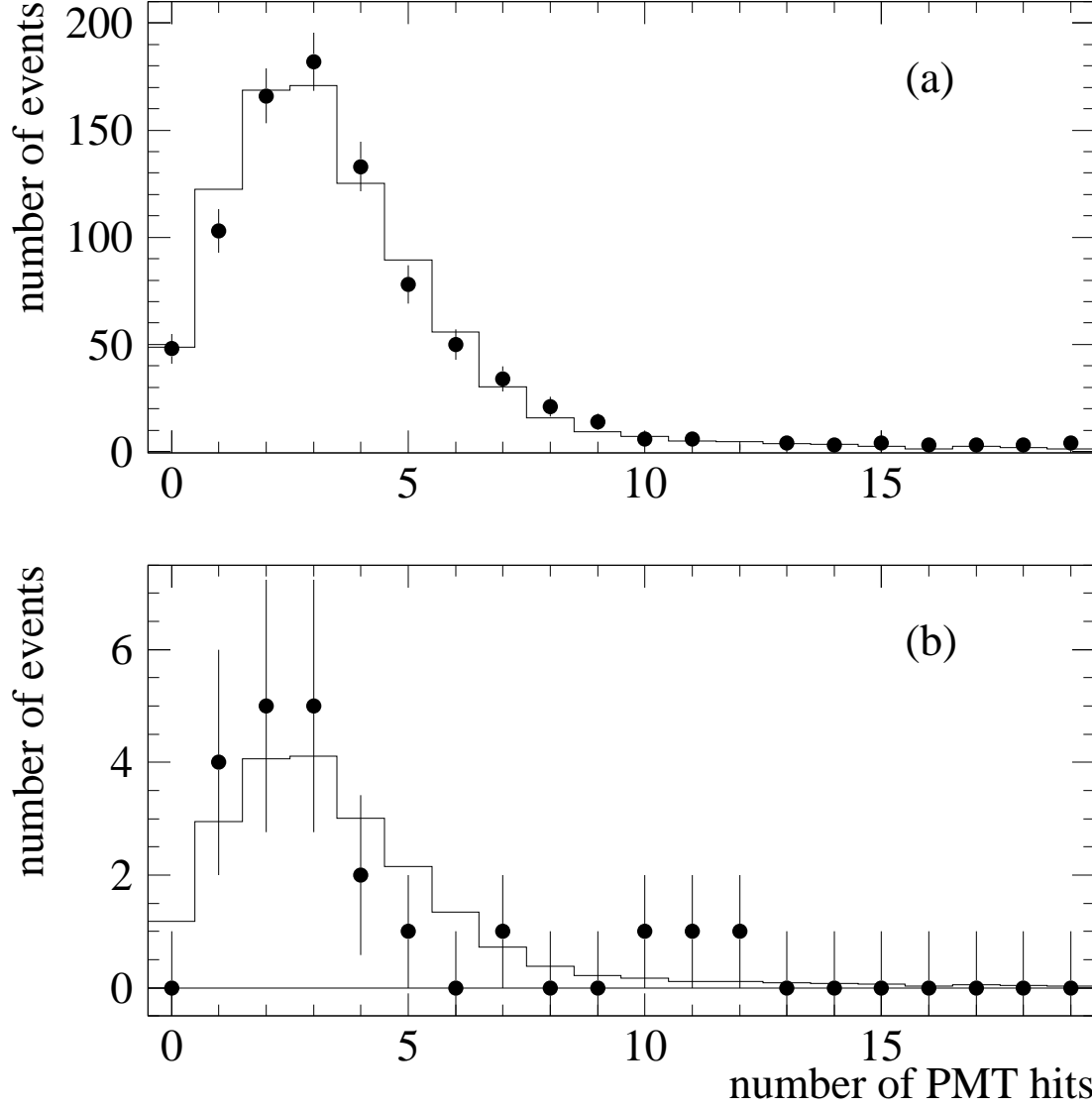


FIG. 32. The total number of hit PMTs in the detector tank for the extra events that occur $0 - 3\mu\text{s}$ and $3 - 6\mu\text{s}$ prior to oscillation candidate events. The candidates are in the $25 < E_e < 60$ MeV energy range with (a) $R \geq 0$ and (b) $R > 30$. The data points are the beam-on events, while the solid curve is what is expected from random PMT hits as determined from the sample of laser calibration events.

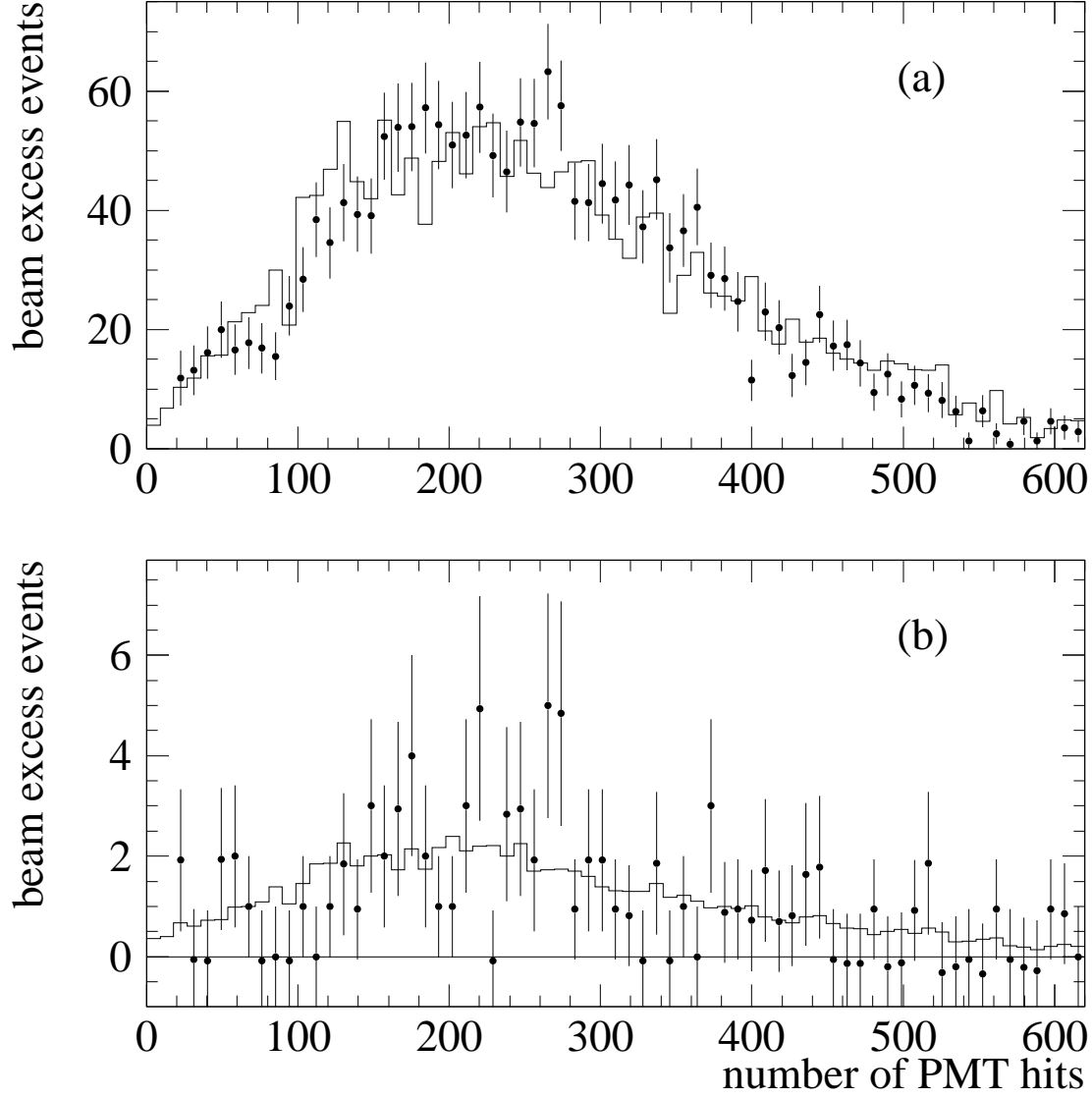


FIG. 33. The observed hit PMT distribution for all $\nu_\mu C$ scattering events (including $\nu_\mu C \rightarrow \mu^- X$, $\bar{\nu}_\mu C \rightarrow \mu^+ X$, and $\bar{\nu}_\mu p \rightarrow \mu^+ n$) for events with (a) $R \geq 0$ and (b) $R > 30$. The solid histogram in each case is the prediction from the Monte Carlo simulation, normalized to the data.

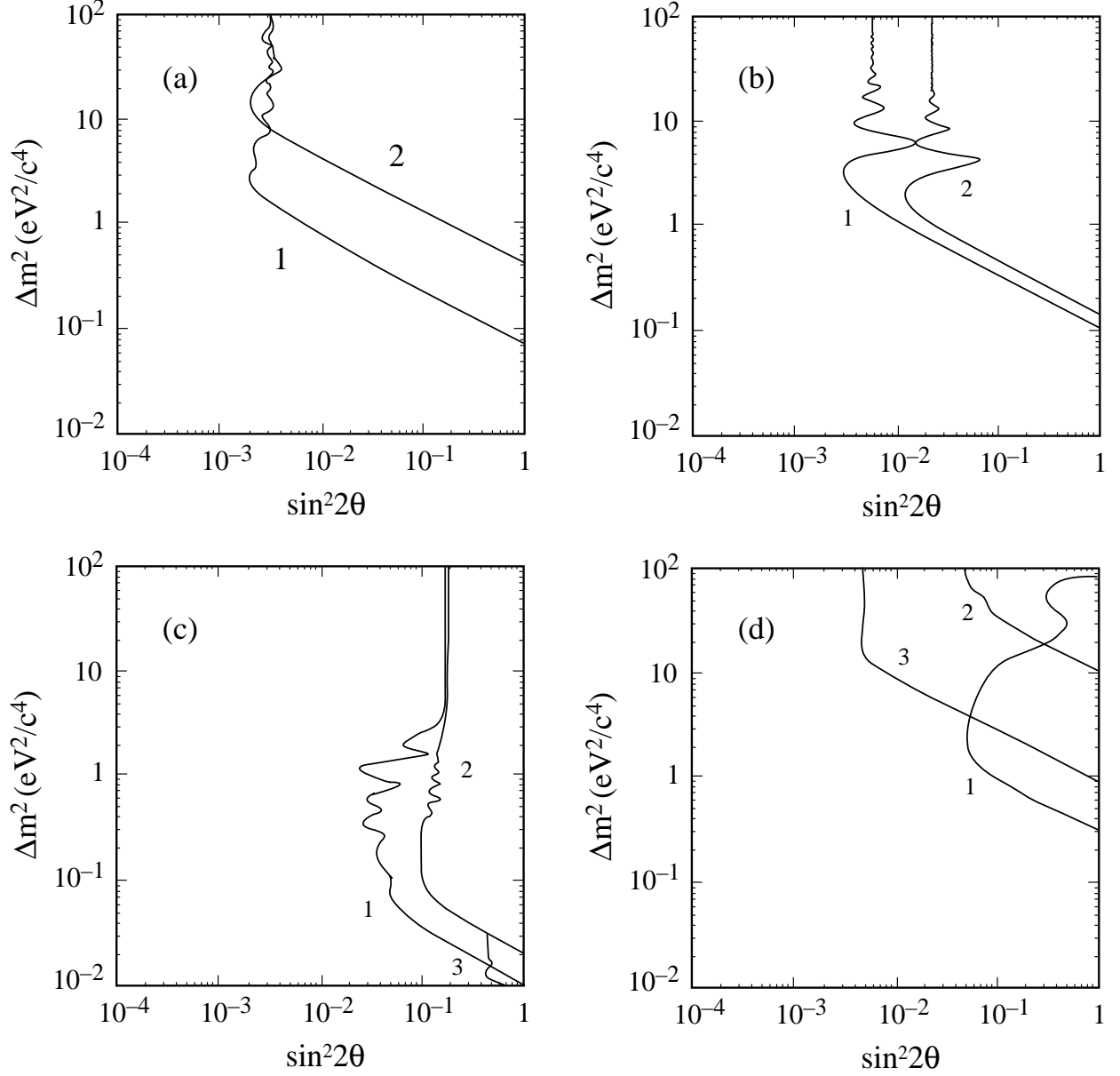


FIG. 34. Most sensitive limits on neutrino oscillations at 90% C.L. (a) $\nu_\mu \rightarrow \nu_e$ appearance from the (1) E776 and (2) E734 experiments at BNL. (b) $\bar{\nu}_\mu \rightarrow \bar{\nu}_e$ appearance from the (1) KARMEN and (2) E645 experiments. (c) $\bar{\nu}_e$ disappearance from the (1) Bugey, (2) Gosgen and (3) Krasnoyarsk reactor experiments. (d) ν_μ disappearance from the (1) CDHS and (2) CCFR experiments. Also shown is the limit from the (3) E531 $\nu_\mu \rightarrow \nu_\tau$ appearance experiment.

REFERENCES

- [1] C. Athanassopoulos *et. al.* , LA-UR-96-1327, submitted to Phys. Rev. C.
- [2] C. Athanassopoulos *et. al.* , Phys. Rev. Lett. **75**, 2650 (1995).
- [3] J. N. Bahcall and M. M. Pinsonneault, Rev. Mod. Phys. **64**, 885 (1992).
- [4] R. Davis, Prog. Part. Nucl. Phys. **32**, 13 (1994).
- [5] Y. Fukuda *et. al.* , Phys. Lett. B **335**, 237 (1994).
- [6] J. N. Abdurashitov *et. al.* , Phys. Lett. B **328**, 234 (1994); P. Anselmanni *et. al.* , Phys. Lett. B **328**, 377 (1994).
- [7] R. Becker-Szendy *et. al.* , Phys. Rev. D**46**, 3720 (1992).
- [8] Y. Hirata *et. al.* , Phys. Lett. B **335**, 237 (1994).
- [9] M. C. Goodman, Nucl. Phys. B (Proc. Suppl.) **38**, 337 (1995).
- [10] T. K. Gaisser, F. Halzen, and T. Stanev, Phys. Rep. **258**, 173 (1995); G. Barr, T.K. Gaisser, and T. Stanev, Phys. Rev. D **39**, 3532(1989); S. Barr, T.K. Gaisser, S. Tilav, and P. Lipari, Phys. Lett. B **214**, 147 (1988).
- [11] C. Cardall and G. M. Fuller, to appear in Phys. Rev. D.
- [12] R. L. Burman, M. E. Potter, and E. S. Smith, Nucl. Instrum. Methods A**291**, 621 (1990); R. L. Burman, A. C. Dodd, and P. Plischke, Nucl. Instrum. Methods in Phys. Research A**368**, 416 (1996).
- [13] C. H. Llewellyn Smith, Physics Reports **3**, 262 (1972); P. Vogel, Phys. Rev. D **29**, 1918 (1984); E. J. Beise and R. D. McKeown, Comm. Nucl. Part. Phys. **20**, 105 (1991).
- [14] R. A. Reeder *et. al.* , Nucl. Instrum. Methods A **334**, 353 (1993).
- [15] J. J. Napolitano *et. al.* , Nucl. Instrum. Methods A **274**, 152 (1989).

- [16] K. McIlhany, *et. al.* , D. Whitehouse, A. M. Eisner, Y-X. Wang and D. Smith, *Computing in High Energy Physics '94* (Proceedings of the Conference on Computing in High Energy Physics April 1994), LBL Report 35822, 357 (1995).
- [17] M. Fukugita, Y. Kohyama, and K. Kubodera, Phys. Lett. B **212**, 139 (1988).
- [18] M. Albert *et. al.* , Phys. Rev. C **51**, 1065 (1995).
- [19] D. Rein and L. M. Sehgal, Nucl. Phys. **B223**, 29 (1983).
- [20] E. Kolbe, K. Langanke, and S. Krewald, Phys. Rev. C **49**, 1122 (1994); (K. Langanke, private communication).
- [21] M. Fukugita, Phys. Rev. C **41**, 1359 (1990).
- [22] B. Bodmann *et. al.* , Phys. Lett. B **267**, 321 (1991); B. Bodmann *et. al.* , Phys. Lett. B **280**, 198 (1992); B. Zeitnitz *et. al.* , Prog. Part. Nucl. Phys., **32** 351 (1994).
- [23] L. Borodovsky *et. al.* , Phys. Rev. Lett. **68**, 274 (1992).
- [24] B. Achkar *et. al.* , Nucl. Phys. **B434**, 503 (1995).
- [25] S. J. Freedman *et. al.* , Phys. Rev. D **47**, 811 (1993).
- [26] K. Eitel, thesis, Universitat und Forschungszentrum Karlsruhe (1995); Forschungszentrum Karlsruhe report FZKA 5684 (1995).
- [27] L. A. Ahrens *et. al.* , Phys. Rev. D **31**, 2732 (1985).
- [28] P. Astier *et. al.* , Nucl. Phys. **B335**, 517 (1990).
- [29] R. C. Allen *et. al.* , Phys. Rev. D **47**, 11 (1993).
- [30] K. S. McFarland *et. al.* , Phys. Rev. Lett. **75**, 3993 (1995); C. Haber *et. al.* , Phys. Rev. Lett. **52**, 1384 (1984).
- [31] G. Zacek *et. al.* , Phys. Rev. D **34**, 2621 (1986).

- [32] G. S. Vidyakin *et. al.* , JETP Letters **59**, 364 (1984).
- [33] F. Dydak *et. al.* , Phys. Lett. B **134**, 281 (1984).
- [34] N. Ushida *et. al.* , Phys. Rev. Lett. **57**, 2897 (1986).